21041

NATIONAL LIBRARY
OTTAWA

BIBLIOTHÈQUE NATIONALE
OTTAWA

NAME OF AUTHOR.... ROBERT DAVID KERR .....

TITLE OF THESIS.... PLASMA DIAGNOSTICS USING CO_2 LASER RADIATION .....

UNIVERSITY..... ALBERTA .....

DEGREE FOR WHICH THESIS WAS PRESENTED.... Ph. D. .....

YEAR THIS DEGREE GRANTED.... SPRING 1974 .....

Permission is hereby granted to THE NATIONAL LIBRARY OF CANADA to microfilm this thesis and to lend or sell copies of the film.

The author reserves other publication rights, and neither the thesis nor extensive extracts from it may be printed or otherwise reproduced without the author's written permission.

(Signed)..... Robert Kerr .....

PERMANENT ADDRESS:

9807-152 ST .....

EDMONTON, ALBERTA .....

.....

DATED.. JANUARY 8 1974

NL-91 (10-68)

THE UNIVERSITY OF ALBERTA

PLASMA DIAGNOSTICS USING CO_2 LASER RADIATION

by

© ROBERT DAVID KERR

A THESIS

SUBMITTED TO THE FACULTY OF GRADUATE STUDIES AND RESEARCH

IN PARTIAL FULFILMENT OF THE REQUIREMENTS FOR THE DEGREE

OF DOCTOR OF PHILOSOPHY

DEPARTMENT OF ELECTRICAL ENGINEERING

EDMONTON, ALBERTA

SPRING, 1974

THE UNIVERSITY OF ALBERTA

FACULTY OF GRADUATE STUDIES AND RESEARCH

The undersigned certify that they have read, and recommend to the Faculty of Graduate Studies and Research, for acceptance, a thesis entitled PLASMA DIAGNOSTICS USING CO_2 LASER RADIATION submitted by ROBERT DAVID KERR in partial fulfilment of the requirements for the degree of Doctor of Philosphy.

A. Offenberger
.....
Supervisor

Peter R. Smith
.....

.....

Douglas M. Sheppard
.....

.....
External Examiner

Date DECEMBER 28, 1973

ABSTRACT

Several experiments utilizing the absorption, interference and Thomson scattering of CO_2 laser radiation as plasma diagnostic techniques are reported.

An electromagnetic shock tube has been used to verify the inverse bremsstrahlung absorption coefficient for 10μ radiation. Subsequent absorption measurements on a plasma jet have yielded electron density profiles. A Mach-Zehnder interferometer and a plasma jet have been used in a quantitative calibration of Langmuir probe ion current from collision-dominated flowing plasmas.

A new technique employing simultaneous absorption and interferometry has yielded both the temporal electron density and temperature in the afterglow of a laser spark in argon. This setup appears particularly suitable for determining electron-ion recombination coefficients.

Integrated Thomson scattering from a low density hollow cathode discharge has been measured. Spectral analysis was unattainable due to poor laser characteristics. A high α, collision-dominated spectrum has been observed for the first time using a plasma jet and a CO_2 laser. Substantial narrowing of the central ion feature due to collisions has been found. In another experiment, the spectrally integrated enhanced scattering from a TEA CO_2 laser-produced hydrogen plasma was measured using a separate TEA CO_2 laser. Enhancements of 1100 times the thermal level have been observed.

Finally, the maximum pulsed CO_2 laser energies usable for low-perturbation diagnostic purposes in atmospheric-pressure, partially ionized plasmas have been obtained using a TEA CO_2 laser and a plasma jet. Measured large-perturbation thresholds are in reasonable agreement with those calculated on the basis of increased ionization limitations.

ACKNOWLEDGEMENTS

Particular thanks go to Dr. A. Offenberger who supervised this work and permitted such a broad range of experiments to be undertaken. His prompt reading and return of this thesis is most appreciated. I would also like to gratefully thank him for encouragement, both professional and personal, during the course of this work.

The author would also like to express his appreciation to the following people: the members of the Plasma Group for their helpful suggestions and assistance; Doug Way-Nee for his technical assistance with the experiments; Barry Arnold for providing the excellent optical components and coatings; Maureen Mounteer for her excellent and prompt typing of this thesis; and the staff of the Machine Shop for their fast and excellent construction of the apparatus with particular thanks going to Konrad Doerbecker and Herb Gans.

The author also gratefully acknowledges financial support received from the National Research Council of Canada and the Department of Electrical Engineering.

TABLE OF CONTENTS

		Page
CHAPTER I :	INTRODUCTION	1
CHAPTER II :	INTERFEROMETRY AND ABSORPTION	6
	2.1 Introduction	6
	2.2 Theory	7
	2.3 Shock Tube Measurements	13
	2.4 Plasma Jet Measurements	20
	2.4.1 Setup	20
	2.4.2 Absorption Results	25
	2.4.3 Interferometer/Langmuir Probe Results	31
	2.5 Transient Interferometric and Absorption Measurements	34
	2.5.1 Setup	34
	2.5.2 Results	37
	2.5.3 Concurrently Time-Varying α and n_R	43
CHAPTER III :	THOMSON SCATTERING	46
	3.1 Introduction	46
	3.2 Theory	48
	3.2.1 Scattering From a Collisionless Maxwellian Plasma	48
	3.2.2 Collision-Dominated Scattering	56
	3.2.3 Enhanced Thomson Scattering	61

Page

3.3 Thomson Scattering From a Low Density Plasma 66
3.3.1 Setup 66
3.3.2 Results and Discussion 70
3.4 High α, Collision-Dominated Thomson Scattering Measurements 71
3.4.1 Setup 71
3.4.2 Results and Discussion 74
3.5 High α, Enhanced Thomson Scattering 78
3.5.1 Setup 78
3.5.2 Results and Discussion 80
CHAPTER IV : PLASMA PERTURBATION BY ABSORPTION OF 10.6μ RADIATION 85
4.1 Introduction 85
4.2 Measurement of Shock Energy Released 86
4.2.1 Setup 86
4.2.2 Results and Discussion 88
4.3 Measurement of Enhanced Emission 94
4.3.1 Setup 94
4.3.2 Results and Discussion 96
CHAPTER V : SUMMARY AND CONCLUSION 102
REFERENCES 106
APPENDIX I 109
APPENDIX II 120

LIST OF FIGURES

		Page
FIGURE 2.1	Experimental setup for absorption measurements using an electromagnetic shock tube	15
2.2	Typical absorption signal in the shock tube experiment	18
2.3	Electron density vs mach number	19
2.4	Experimental setup for absorption measurements using a plasma jet	21
2.5	Experimental setup for interferometric and Langmuir probe measurements in a plasma jet	23
2.6	Electrical circuit of the Langmuir probe	24
2.7	Variables describing light ray passage through the jet	27
2.8	Electron density vs radius from absorption measurements	29
2.9	Electron density vs height from absorption measurements	30
2.10	Electron density vs radius from probe measurements	33
2.11	Experimental setup for simultaneous absorption and interferometry	35

		Page
2.12	Typical absorption and interference signals in the laser spark	38
2.13	Temporal electron density and temperature in the laser spark	41
2.14	Reciprocal electron density in the laser spark	42
2.15	Two-detector Mach-Zehnder interferometer	44
FIGURE 3.1	The function $W(x)$	52
3.2	The function $\Gamma_a(x)$	54
3.3	The function $\Gamma_1^c(x)$	60
3.4	Experimental setup for Thomson scattering from a low-density plasma	67
3.5	Experimental setup for Thomson scattering from a collision-dominated plasma	72
3.6	Fabry-Perot resolution characteristics for a plate spacing of 10 cm	76
3.7	Fabry-Perot interferograms (a) noise and background, (b) Thomson scattering	77
3.8	Experimental setup for enhanced Thomson scattering	79
FIGURE 4.1	Experimental setup for jet perturbation measurements using a piezoprobe	87
4.2	Shock energy released vs incident laser energy	89
4.3	Incident laser energy vs average electron density	93

		Page
4.4	Experimental setup for enhanced plasma emission measurements	95
4.5	Enhanced plasma emission vs input laser energy	98
4.6	Interaction volume of TEA laser and plasma jet	99
FIGURE A2.1	Fabry-Perot resolution characteristics as a function of plate spacing	123

CHAPTER I

INTRODUCTION

Interferometry and Thomson scattering have been well established as plasma diagnostics at wavelengths of 0.5 to 0.7μ. On the other hand, measurements using inverse bremsstrahlung absorption in this range of wavelengths have been restricted to situations of very high electron density such as metal blowoff plasmas; attenuation of this radiation at lower densities is totally negligible. Much interest exists in these methods for several reasons.

Good temporal resolution of < 10ns can be obtained by using available pulsed lasers and detectors, and is often required to determine parameters in a transient plasma. Since high frequency radiation does not couple strongly to other than very dense plasmas, perturbations are usually small. Unlike other diagnostic techniques such as electric and magnetic probes, the actual setup is physically remote from the plasma and thus problems of contamination and component temperature stresses are generally not important.

Interferometrically measured fringe shifts vary as λn_e and directly yield the electron density for a laser frequency ω much larger than the electron plasma frequency ω_{pe}. In addition, absorption via inverse bremsstrahlung varies as $\lambda^2 n_e^2 T_e^{-3/2}$ and therefore T_e can be calculated if n_e is known. Thus combined use of absorption and interferometry for $\omega >> \omega_{pe}$ will explicitly determine n_e and T_e. It can also be seen that sensitive measurement of low density plasmas

utilizing a simple experimental arrangement requires use of long wavelengths. In general, measured fringe shifts and transmission are results integrated through the plasma, thus only spatially averaged electron density and temperature are obtained. However, most plasmas have cylindrical symmetry and therefore these results can be Abel unfolded to determine the spatial variations.

A much more informative diagnostic is Thomson scattering. Spatial resolution is excellent since this is in fact only limited by the collection optical system. In addition, several parameters such as n_e, n_i, T_e, T_i, electron distribution functions and magnetic field can be determined from relatively few measurements.

On the other hand, scattered signals are quite small (cross section $\sim 10^{-25}$ cm^2) and considerable effort is often required to reduce noise and stray light to acceptable levels. Even with available high power lasers, this presently limits measurements to $n_e > 10^{13}$ cm^{-3}.

Thus these two methods of probing plasmas have quite different but useful applications. Often only a macroscopic electron density and temperature is sought and therefore interferometry and absorption would suffice. In this case the experimental setup is quite straightforward and requires a minimum of specialized equipment; results can be obtained fairly quickly.

Alternatively, Thomson scattering is more applicable should detailed microscopic information be desired. However this usually requires spectral dispersion, maximum detection capability and sophisticated signal-to-noise improvement equipment. In addition, stray light problems have to be solved empirically.

Considerable interest in using 10.6μ radiation from CO_2 lasers to do these measurements exists for several reasons. Substantially more absorption and optical path difference are obtained by using this long wavelength and thus lower density plasmas are able to be probed. For Thomson scattering from low density plasmas ($n_e \sim 10^{14}$ cm^{-3}) such as would be used in steady-state fusion reactors, 10μ radiation is desirable since fairly large scattering angles can be used to obtain an optimal scattering parameter $\alpha \sim 1$. This in turn results in a substantially decreased resolving power required for spectral analysis.

For dense plasmas, very high α Thomson scattering is available which enables relatively long wavelength coherent density fluctuations to be measured. In particular, wavelengths longer than particle mean free paths can be used in a quantitative investigation of collisional processes in plasmas.

Although various types of lasers may be used to secure these long wavelength features, the most practical choice is the CO_2 laser from which very high powers can be obtained both continuously and pulsed.

The purpose of this thesis has been to experimentally establish interferometry, absorption and Thomson scattering of CO_2 laser radiation as reliable plasma diagnostic techniques.

Chapter II first summarizes the theoretical absorption and dispersion of high frequency radiation in unmagnetized Maxwellian plasmas. Experimentally, an electromagnetic shock tube with known electron density and temperature has been used to quantitatively verify the inverse bremsstrahlung absorption coefficient at $\lambda = 10\mu$.

For partially ionized plasmas, absorption can be used to spatially resolve the electron density since in this case the electron temperature is essentially constant ($n_e \sim T_e^8$). Such measurements were done using an argon plasma jet.

Langmuir probes are also a valuable diagnostic and have been well established for fully-ionized collisionless plasmas. In order to experimentally verify the theory of convection-limited ion current in high density collisional plasmas, the electron density in a plasma jet has been measured using both a CO_2 laser interferometer and a Langmuir probe.

Finally, a new technique employing simultaneous interferometry and absorption has been used to temporally measure both n_e and T_e in the afterglow of a transient laser-produced plasma.

Chapter III describes experiments undertaken to measure three limiting cases of Thomson scattering. The first was collisionless scattering from a low density ($\sim 5 \times 10^{13}$ cm^{-3}) hollow cathode discharge. Secondly, a high density ($\sim 2 \times 10^{17}$ cm^{-3}) argon plasma jet was used for observation of a collision-dominated scattered spectrum. Finally, measurements were made of Thomson scattering from non-thermal density fluctuations in a turbulent laser-produced plasma. A TEA CO_2 laser was chosen to produce the plasma in order to induce fluctuations with long wavelengths ($\sim 10\mu$).

Chapter IV discusses practical limits of CO_2 laser power for diagnostic purposes above which large plasma perturbations are caused. Experimental thresholds for TEA CO_2 laser radiation focused into a plasma jet have been measured using both shock energy released

and enhanced plasma emission to monitor the level of perturbation.

CHAPTER II

INTERFEROMETRY AND ABSORPTION

2.1 Introduction

Plasma diagnostics using interferometry and inverse bremsstrahlung absorption of CO_2 laser radiation are presented. The absorption coefficient was experimentally verified for 1 eV plasmas using an electromagnetic shock tube. Subsequent use of the absorption technique to obtain electron density profiles in an argon plasma jet is reported.

Since Langmuir probes can also be very useful for measuring plasma density, quantitative verification of the convection-dependent, flowing plasma probe theory has been done using the jet and a Mach-Zehnder interferometer at 10.6μ. Radial electron density profiles have also been obtained using the probe and are in agreement with those obtained from the absorption measurements.

The use of CO_2 laser radiation in simultaneous interferometry and absorption measurements for temporal resolution of electron density and temperature in transient plasmas has been investigated in the decay of a laser spark in argon. These results have been used to calculate the recombination coefficient for argon.

2.2 Theory

The nature of propagation of transverse electromagnetic waves in plasmas is obtained by solving Maxwell's equations, allowing for the non-zero conductivity due to charged particles. Plane wave solutions of the form $\underline{E}_o e^{i(\underline{k}\cdot\underline{r}-\omega t)}$ in an isotropic unmagnetized plasma satisfy the dispersion relation

$$k^2 = \frac{\omega^2}{c^2}\left\{\epsilon + \frac{4\pi\sigma}{\omega} i\right\} = n^2 \frac{\omega^2}{c^2} \qquad 2.1$$

where σ = conductivity due to the charged free particles, n = refractive index, and ϵ = dielectric constant which includes both bound electron polarizability and absorption.

In general ϵ and σ are complex quantities. The refractive index is thus

$$n^2 = \left\{\left(\epsilon_R - \frac{4\pi}{\omega}\sigma_I\right) + i\left(\epsilon_I + \frac{4\pi}{\omega}\sigma_R\right)\right\} \qquad 2.2$$

where R and I denote the real and imaginary parts.

For interferometric and absorption measurements, appreciable transmission of the wave through the plasma is required. Hence only radiation of sufficiently high frequency can be utilized. In this case $n_I \ll 1$ and $\omega > \omega_{pe}$ such that the refractive index can be approximated by

$$n \approx \sqrt{\epsilon_R - \frac{4\pi}{\omega}\sigma_I} + \frac{1}{2} i \frac{\left(\epsilon_I + \frac{4\pi}{\omega}\sigma_R\right)}{\sqrt{\epsilon_R - \frac{4\pi}{\omega}\sigma_I}} \; . \qquad 2.3$$

The condition $\omega > \omega_{pe}$ results in a positive quantity under the root sign.

In the experiments performed, bound electron effects were negligible. To this end the dielectric constant can be taken as $\epsilon = 1$, such that

$$n = n_R + in_I = \sqrt{1 - \frac{4\pi}{\omega}\sigma_I} + i\frac{2\pi\frac{\sigma_R}{\omega}}{\sqrt{1 - \frac{4\pi}{\omega}\sigma_I}} . \qquad 2.4$$

An approximation to σ can be obtained from a two fluid model. The current density is given by

$$\underline{j} = -e\, n_e\, \underline{v}_e \qquad 2.5$$

where n_e = electron density and $\underline{v}_e$ = wave induced electron velocity. A negligible ion contribution has been taken because of the large ion-electron mass ratio. The induced velocity is obtained from

$$\frac{d\underline{v}_e}{dt} = -\frac{e\underline{E}}{m_e} - \nu_e \underline{v}_e \qquad 2.6$$

which has the steady state solution

$$\underline{v}_e = -\frac{e\underline{E}}{m_e(\nu_e - i\omega)} \qquad 2.7$$

where $\underline{E}$ = wave electric field, ω = wave frequency and ν_e is the effective collision frequency of the electrons representing the dissipation. Thus

$$\underline{j} = \sigma \underline{E} = \frac{1}{4\pi}\left(\frac{\omega_{pe}^2(\nu_e + i\omega)}{\nu_e^2 + \omega^2}\right)\underline{E} \quad . \qquad 2.8$$

For $\omega > \omega_{pe}$, low absorption cases correspond to $\frac{4\pi\sigma_R}{\omega} << 1$ (see eqn. 2.4) and thus to $\omega >> \nu_e$. In this limit, the conductivity is given to first order by

$$\sigma = \frac{1}{4\pi}\,\frac{\omega_{pe}^2}{\omega^2}(\nu_e + i\omega) \qquad 2.9$$

whereby from eqn. 2.4

$$n \approx \sqrt{1 - \frac{\omega_{pe}^2}{\omega^2}} + i\,\frac{\nu_e \omega_{pe}^2}{2\omega^3\sqrt{1 - \frac{\omega_{pe}^2}{\omega^2}}} \quad . \qquad 2.10$$

Thus for high frequencies, n_R depends only on the electron density.

The detailed absorption requires further calculation of the effective electron collision frequency for high frequency waves. A linearized Vlasov treatment is presented by Dawson and Oberman[1]. Their result includes collective plasma oscillations and for $\omega >> \omega_{pe}$ gives

$$n \approx \sqrt{1 - \frac{\omega_{pe}^2}{\omega^2}} + i\,\frac{4\sqrt{2\pi}^{3/2} e^6}{3m_e^{3/2}\sqrt{1 - \frac{\omega_{pe}^2}{\omega^2}}} \cdot \frac{Zn_e^2}{\omega^3 (KT_e)^{3/2}}\left[\ell n\left(\frac{2k_{max}^2 v_{th}^2}{\omega^2}\right) - \gamma\right] \qquad 2.11$$

where m_e = electron mass, T_e = electron temperature, $Z = \frac{n_e}{n_{ion}}$,

$v_{th} = \sqrt{\frac{KT_e}{m_e}}$ = electron thermal speed, $\gamma = 0.577$ = Euler's constant, and

$$\frac{1}{k_{max}} \sim \frac{Ze^2}{m_e v_{th}^2} \qquad 2.12$$

is the classical minimum impact parameter.

An explicit absorption constant can then be obtained by noting that the wave propagates according to $e^{-i\underline{k}\cdot\underline{r}} = e^{-n_I(\hat{\underline{e}}\cdot\underline{r})\omega/c}\, e^{in_R(\hat{\underline{e}}\cdot\underline{r})\omega/c}$ whereby the power absorption coefficient is given by

$$\alpha = \frac{2n_I\omega}{c} \quad . \qquad 2.13$$

Thus the Dawson and Oberman result implies

$$\alpha = \frac{8\sqrt{2}e^6}{3c}\left(\frac{\pi}{m_e}\right)^{3/2} \frac{Zn_e^2}{\omega^2\sqrt{1 - \frac{\omega_{pe}^2}{\omega^2}(KT_e)^{3/2}}} \left[\ln\left(\frac{2k_{max}^2 v_{th}^2}{\omega^2}\right) - \gamma\right] \qquad 2.14$$

or numerically

$$\alpha = \frac{4.34\times10^{-38}}{\sqrt{1 - \frac{\omega_{pe}^2}{\omega^2}}} \frac{Zn_e^2\lambda_\mu^2}{T_e^{3/2}} \ln\left(\frac{.0269\, T_e^3\lambda_\mu^2}{Z^2}\right) \text{ cm}^{-1}$$

for $n_e = \text{cm}^{-3}$, λ_μ = microns, and T_e = eV. $\qquad 2.15$

Quantum mechanical calculations of the absorption coefficient in Maxwellian plasmas are outlined by Shkarofsky et al[2], who give

$$\alpha = \frac{4}{3}\sqrt{\frac{2\pi}{3}} \frac{e^6}{c^3 m_e^{3/2}} \frac{Zn_e^2\lambda^2}{(KT_e)^{3/2}} \left[\frac{1 - e^{-\hbar\omega/KT_e}}{\hbar\omega/KT_e}\right] \bar{G}(\omega,T) \qquad 2.16$$

where $\bar{G}$ is the averaged Gaunt factor. For 10.6μ radiation and $T_e \geq 1$ eV, $\hbar\omega/KT \ll 1$, hence

$$\alpha = 1.57\times10^{-37} \frac{Zn_e^2\lambda_\mu^2}{T_e^{3/2}} \bar{G}(\omega,T) \quad cm^{-1} \qquad 2.17$$

where $n_e = cm^{-3}$, $T_e = eV$, λ_μ = microns and where $1.4 \leq \bar{G} \leq 2.5$ for $1 \leq T_e \leq 10$ eV. This result is larger than that of Dawson and Oberman by 10% at $T_e = 10$ eV and by a factor of ~ 4.6 at 1 eV. The disparity is attributable to assumptions by Dawson and Oberman which become invalid at low temperature.

Since no theoretical models have been exactly solved, the absorption constant of a singly ionized argon plasma with accurately known n_e and T_e was experimentally measured as described later in this chapter. The results indicate that

$$\alpha \sim 1.6\times10^{-37} \frac{\lambda_\mu^2 n_e^2}{T_e^{3/2}} \quad cm^{-1} \qquad 2.18$$

(microns, cm^{-3}, eV) for $T_e \sim 1$ eV, $n_e \sim 5\times10^{16} cm^{-3}$ and $Z = 1$. Note that this is the result of eqn. 2.17 if $\bar{G}$ is set equal to 1.

It is of interest to calculate ν_e in eqn. 2.10 from this value of α. Using $\alpha = 2n_I\omega/c$ gives

$$\nu_e = 5.36\times10^{-6} \frac{n_e}{T_e^{3/2}} \sqrt{1 - \frac{\omega_{pe}^2}{\omega^2}} \quad sec^{-1} \qquad 2.19$$

(cm^{-3}, eV). In the experiments $n_{emax} \sim 10^{18} cm^{-3}$, $\left(\frac{n_e}{T_e^{3/2}}\right)_{max} \sim$

1.1×10^{18} $cm^{-3}eV^{-3/2}$ and $\omega = 1.78\times10^{14}$ sec^{-1} for which $\nu_{emax} \sim 6\times10^{12}$ sec^{-1}. Thus expansion of the conductivity (eqn. 2.9) for $\nu_e << \omega$ was indeed valid.

In an interferometer, the number of fringe shifts due to an optical path difference caused by the plasma is

$$n = \frac{\int_L (n_R - 1)d\ell}{\lambda} \qquad 2.20$$

where L = path of the beam through the plasma and λ = wavelength in the absence of the plasma. Similarly for absorption, the relative transmission is

$$T = e^{-\int_L \alpha(\ell)d\ell} \quad . \qquad 2.21$$

For $\omega >> \omega_{pe}$, $n_R - 1 \sim \lambda^2 n_e$ (eqn. 2.10) and $\alpha \sim \frac{\lambda^2 n_e^2}{T_e^{3/2}}$ (eqn. 2.17). Thus use of long wavelengths offers the most accurate measurements as well as the capability to probe lower density, higher temperature plasmas. In addition, combined use of interferometry and absorption yields both n_e and T_e - n_e explicitly from the fringe shifts which subsequently allows calculation of T_e from the absorption. However, it can be seen that only an average density and temperature are obtained from such measurements. Additional information about the plasma geometry is needed in order to calculate the spatial variations.

The results of eqns. 2.10 and 2.17 apply only to cases of dominant free electron contributions. Ionic and atomic polarizability has been neglected ($\epsilon_R = 1$). This assumption is valid for the ions

since there are at least as many free electrons. On the other hand, a large neutral concentration can lead to complete masking of the electronic component, whereby sensitive interferometric measurements in very weakly ionized plasmas may not be possible. This problem may be lessened by choosing ω closer to ω_{pe} but then excessive beam refraction due to density gradients may occur.

The absorption constant given here is only that due to free-free electron transitions in the fields of ions. However, at 10.6μ, the bound-bound and bound-free (ionization) transitions are from highly excited ionic or atomic states. The density of such states in substantially ionized gases is much less than the electron density and hence the contribution to the absorption by these transitions is negligible compared to that of the free electrons.

In addition, if the plasma is only partly ionized, inverse bremsstrahlung due to electron-neutral collisions must also be considered. However, for plasmas of eV temperatures, electron-ion collisions dominate the absorption for degrees of ionization >1%[3]. This can also be checked experimentally by noting whether α varies as n_e^2 (characteristic of electron-ion interaction) or as n_e (characteristic of electron-neutral interaction).

Thus in substantially ionized (>1%) plasmas with eV temperatures, the propagation of CO_2 laser radiation is essentially described by eqns. 2.10 and 2.17 which depend only on n_e and T_e. Plasmas in this regime were used in the following experiments.

2.3 Shock Tube Measurements

The use of an electromagnetic shock tube for determining the

absorption coefficient was doubly advantageous. Firstly, it is known that the plasma obtained is quite reproducible and has n_e and T_e that are accurately predicted from the Rankine-Hugoniot and Saha relations. Secondly, these parameters are essentially constant across the shock tube diameter. This absence of gradients eliminates spatial unfolding of the results.

Fig. 2.1 shows the experimental setup used. The shock tube[4] had a diameter of 2" and utilized helium as the driver gas. The downstream section was evacuated and backfilled with 1 Torr of argon for each shot. Measurements were done ~20 diameters (96 cm) from the mylar diaphragm thus assuring proper shock structure at this point. The two sodium chloride windows were mounted 3 1/2" back from the centre of the tube in order to prevent excessive condensation of vaporized material on them.

A low-pressure sealed-off CO_2 laser[5] was used. A continuous output power of ~ 2W in a beam of ~ 2mm diameter at a wavelength of 9.4μ (00°1 - 02°0 transition band) was obtained. The radiation was focused into the plasma with this point being re-imaged onto a gold-doped germanium detector so that any negative lens effect of the plasma could be compensated for. Detection response time was reduced to that of the detector itself (<100ns) by terminating in a 100Ω load. This was quite adequate for these measurements.

The ionizing shock front passing through the test section emitted substantial broadband bremsstrahlung into the optical system. Since these dectectors are sensitive over a bandwidth ~5μ of infra-red as well as in the visible, a 9.4μ bandpass filter (B.P. = .52μ) was used

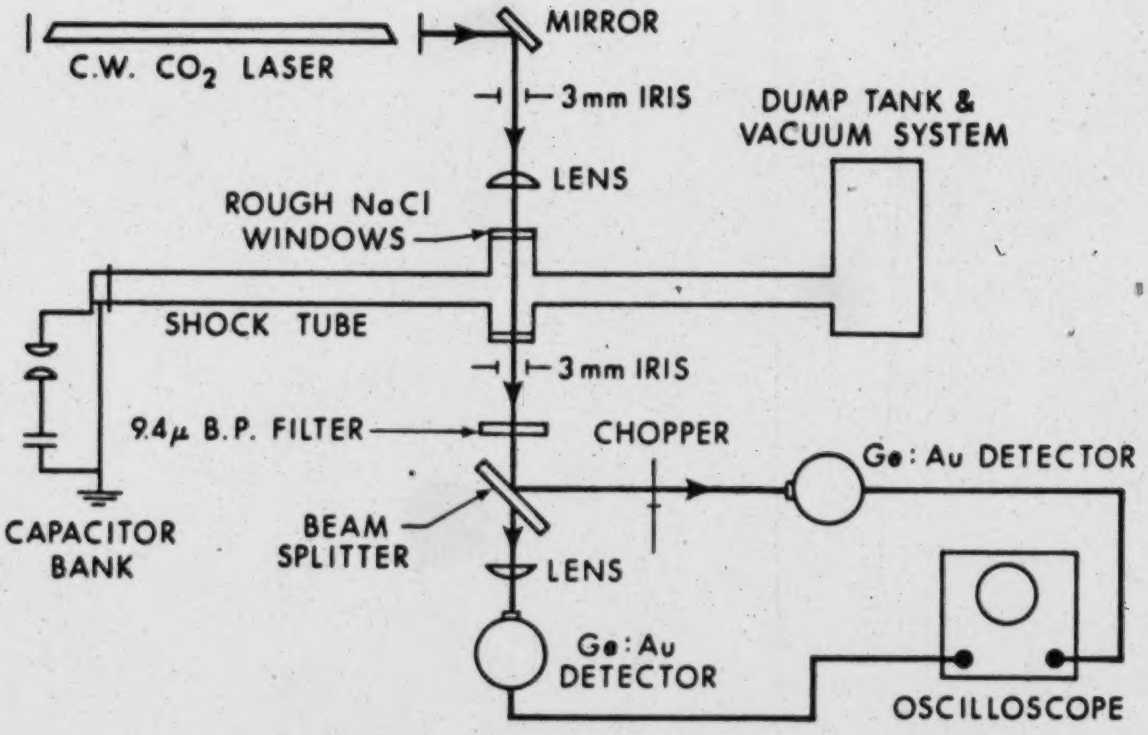

Fig. 2.1 Experimental setup for absorption measurements using an electromagnetic shock tube.

to limit the spectrally integrated radiation seen. Further reduction of the visible radiation was achieved by finely roughening the NaCl windows. Separate measurements indicated that 10μ light was relatively unaffected by this while that from a He-Ne laser was effectively scattered over 4π sr.

A piezoelectric pressure transducer located 7.5 cm upstream from the laser beam was used to trigger the oscilloscope. This allowed calculation of the shock mach number from the delay time of the observed absorption.

An absolute reference power level was obtained by chopping the radiation just prior to each firing of the shock tube. That this remained constant throughout the shot was monitored on a second detector viewing a continuouslychopped fraction of the beam. The laser output was found to slowly vary over a period of several minutes.

Initial alignment of the optical system was done using a He-Ne laser. Irises were placed as shown so that the CO_2 laser beam could be adjusted to follow the same path. These were subsequently opened to a 3mm aperture for the measurements. Results of integrated absorption were obtained for mach numbers in the range 15-18 into 1 Torr of argon by varying the capacitor back voltage.

The electron density and temperature were calculated from

$$n_e = \alpha_i \left(\frac{\rho_2}{\rho_1}\right) n_{01} \qquad 2.22$$

$$T_e = T_2$$

where n_{01} = neutral density of the unshocked gas, T_2 = equilibrium temperature behind the shock, ρ_2/ρ_1 = density ratio across the shock and

α_i = fractional ionization in the shocked gas. Numerically calculated curves, using the Rankine-Hugoniot and Saha relations, of α_i, ρ_2/ρ_1, T_2/T_1 versus mach number M in argon as presented by Mikoshiba[6] were used. As mentioned, M was experimentally determined from the piezo-electric probe:

$$M = \frac{7.5\text{cm}}{tc_1} \qquad 2.23$$

where t = time delay of the absorption signal on the scope and c_1 = 319 m/sec = sound speed in argon at 25°C. For M = 15-18, $n_e \sim 3\times10^{16}$-8×10^{16} cm^{-3} and $T_e \sim 1$ eV.

Since the diameter of the focused laser light was much less than that of the shock tube (D ~ 5cm), the transmission is given by (see eqns. 2.17 and 2.21)

$$T = \exp -(1.57\times10^{-37} \frac{\lambda^2 n_e^2}{T_e^{3/2}} \bar{G}D) \qquad 2.24$$

where $\hbar\omega \ll KT_e$ has been taken. For M < 50, the plasma obtained is only singly ionized, hence Z = 1. The purpose of these measurements was to obtain an accurate numerical value for $\bar{G}$. Observed transmissions were in the range 7-40%.

A typical absorption signal is shown in Fig. 2.2 for M = 20. Note that an increase in radiation corresponds to a negative trace deflection. Comparison of measured absorptions with those predicted by the known n_e and T_e gave $\bar{G}$ = 1 as the appropriate Gaunt factor.

For M = 15-18, the plasma was not fully ionized ($\alpha_i \sim 0.1$-0.3) and hence the temperature variations were small (~10%). Thus it is of

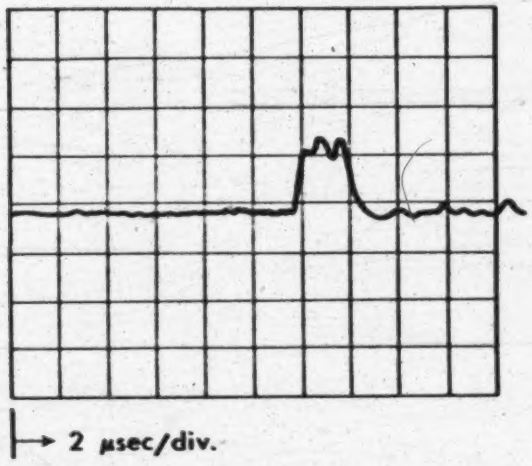

Fig. 2.2 Typical absorption signal in the shock tube experiment.

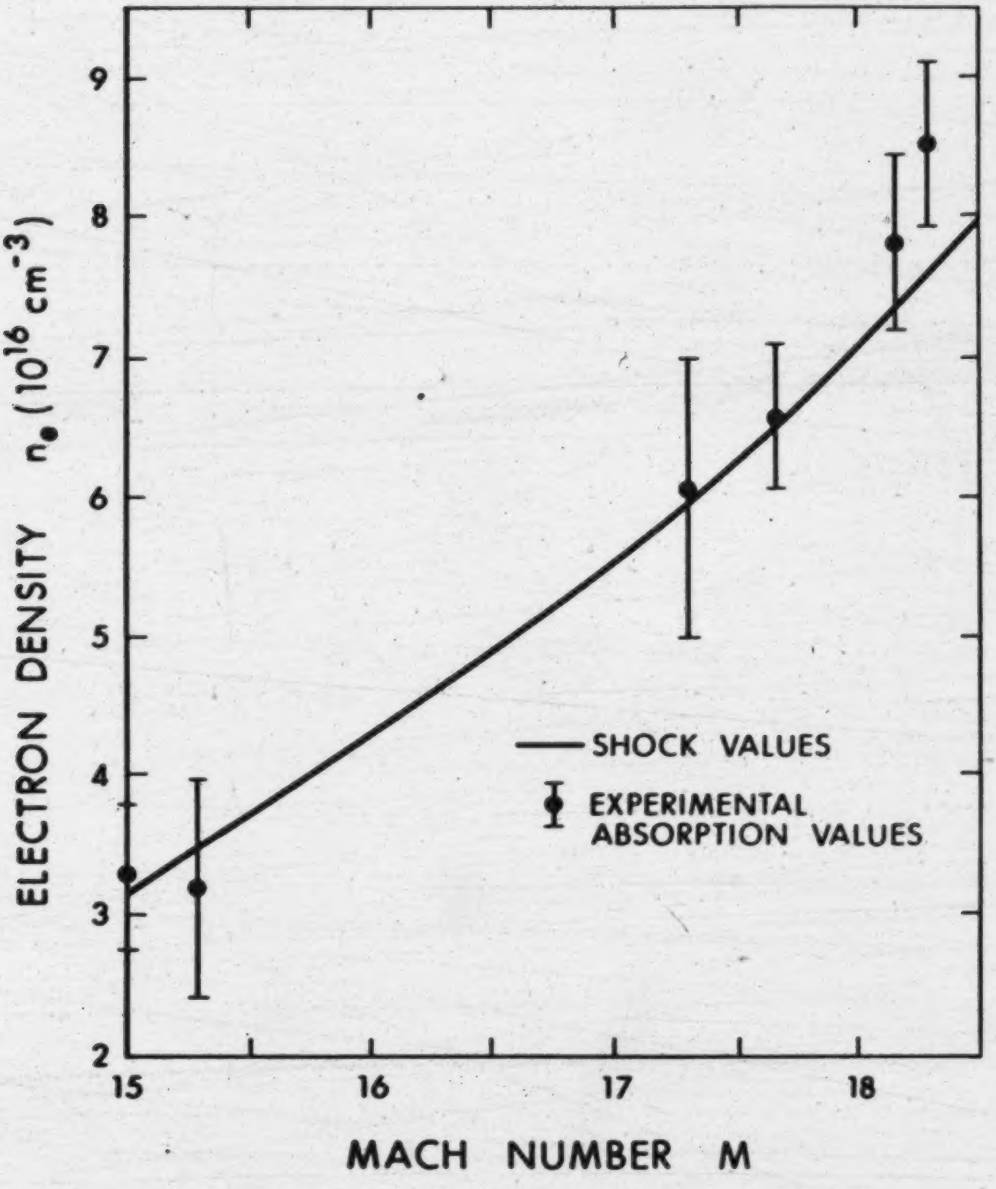

Fig. 2.3 Electron density vs mach number determined from absorption measurements.

sufficient accuracy to use the temperature predicted by the shock relations to calculate n_e from the measured transmission (taking $\bar{G} = 1$).

This n_e versus M is plotted in Fig. 2.3 along with the shock predicted values. The error bars correspond to individual shot variations. It can be seen that agreement is good in view of the strong dependence of n_e on M, whereby small uncertainties in M (mostly oscilloscope time errors) would account for the discrepancies.

Evidently the electron-neutral inverse bremsstrahlung contribution was negligible since a complete n_e^2 dependence was found even at M = 15 where the plasma was only 10% ionized.

These results demonstrate the absorption technique to be simple and reliable, and to have good temporal resolution. It is quite apparent that $\bar{G} = 1$ is the appropriate Gaunt factor for CO_2 laser radiation in plasmas with $n_e \sim 5 \times 10^{16}$ cm^{-3} and $T_e \sim 1$ eV.

2.4 Plasma Jet Measurements

2.4.1 Setup

The setup used in the absorption measurements is shown in Fig. 2.4. A standard argon plasma jet[7] was utilized.

The CO_2 laser was that used in the shock tube measurements with the exception that here the wavelength was 10.6μ. The 2W continuous beam was focused into the plasma (focal spot size = 0.4 mm) and then re-imaged onto the Ge:Au detector to eliminate the negative refraction by the plasma. Constant relative absorption as a function of input iris aperture size was obtained implying adequate compensation.

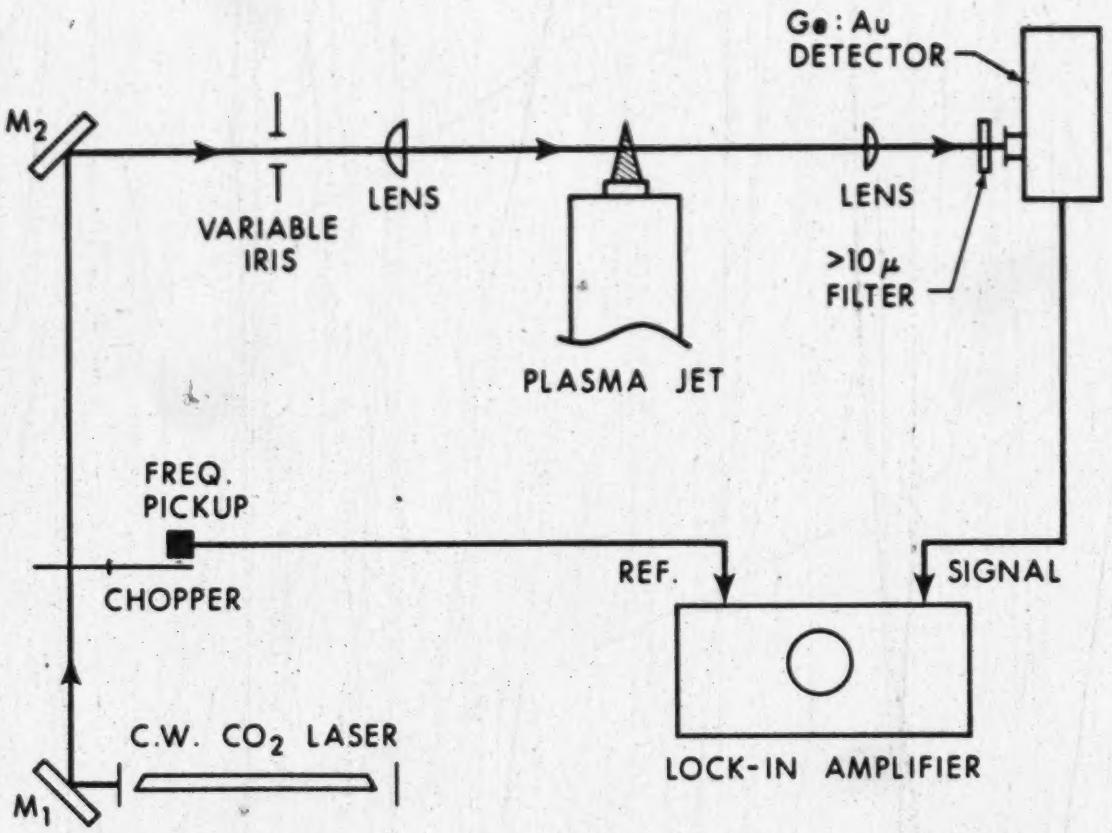

Fig. 2.4 Experimental setup for absorption measurements using a plasma jet.

Typically 0.5° shift of the beam was observed. A long-wavelength cut-on filter was used to reduce the plasma emission seen by the detector.

Synchronous detection using a P.A.R. HR-8 lock-in amplifier provided a good signal-to-noise ratio as well as temporal averaging. Modulation of the laser beam was done using a chopper wheel with a photoelectric pickup to provide a frequency reference for the lock-in amplifier.

Measurements of transmission were done both as a function of radial position 7.5mm above the anode and as a function of axial position from 3-12mm above the anode. This was done simply by translating the jet horizontally and vertically across the focused probe beam.

The jet was operated at a current of 300 Amp. and an argon flow rate of 80cc/sec (N.T.P.).

Further density measurements were done using a swept Langmuir probe, quantitatively calibrated using a Mach-Zehnder interferometer as shown in Fig. 2.5.

The output beam of the CO_2 laser was three-fold expanded to $\sim$ 6mm diameter using two NaCl lenses in order to obtain a large area of background fringes to which shifts due to the plasma ($\sim$ 3mm diameter) could be referenced. This provided for viewing of the complete extent of the jet.

The beam splitters were NaCl substrates with a 10% reflecting coating on one surface and an anti-reflection coating on the other.

An additional lens at the output of the interferometer further expanded the beam so a large display of fringes could be obtained.

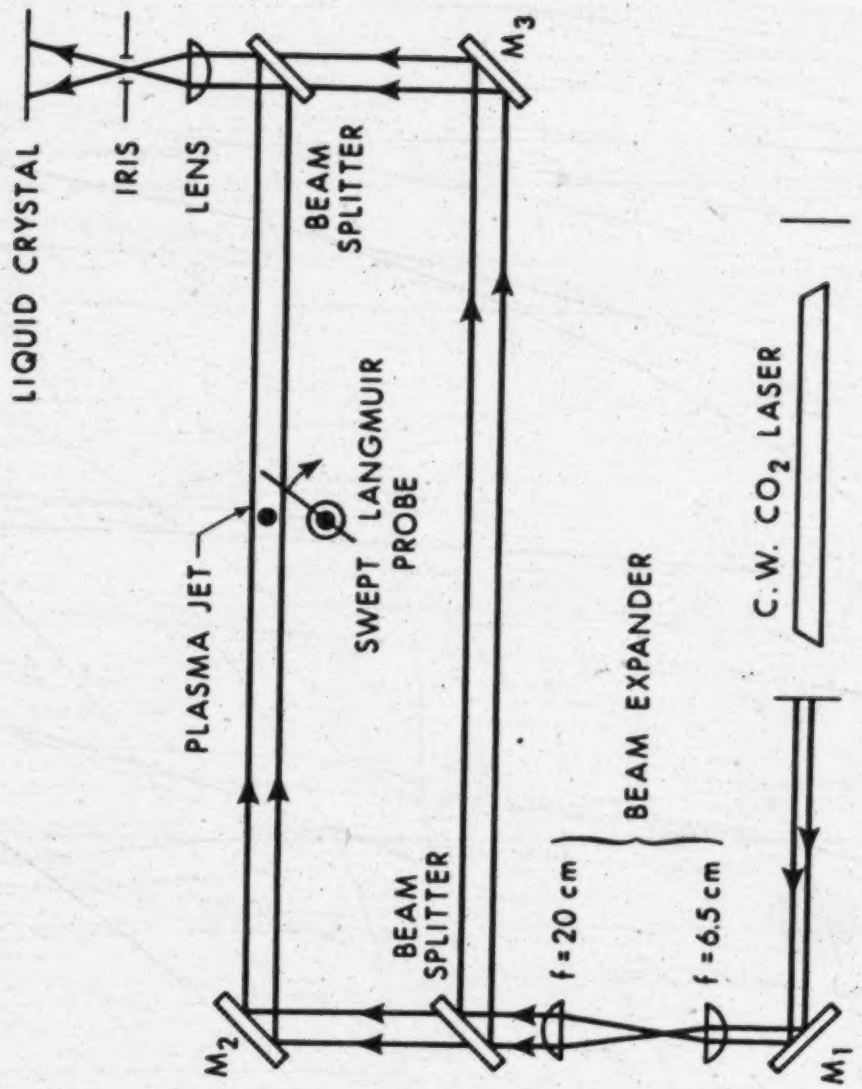

Fig. 2.5 Experimental setup for interferometric and Langmuir probe measurements in a plasma jet.

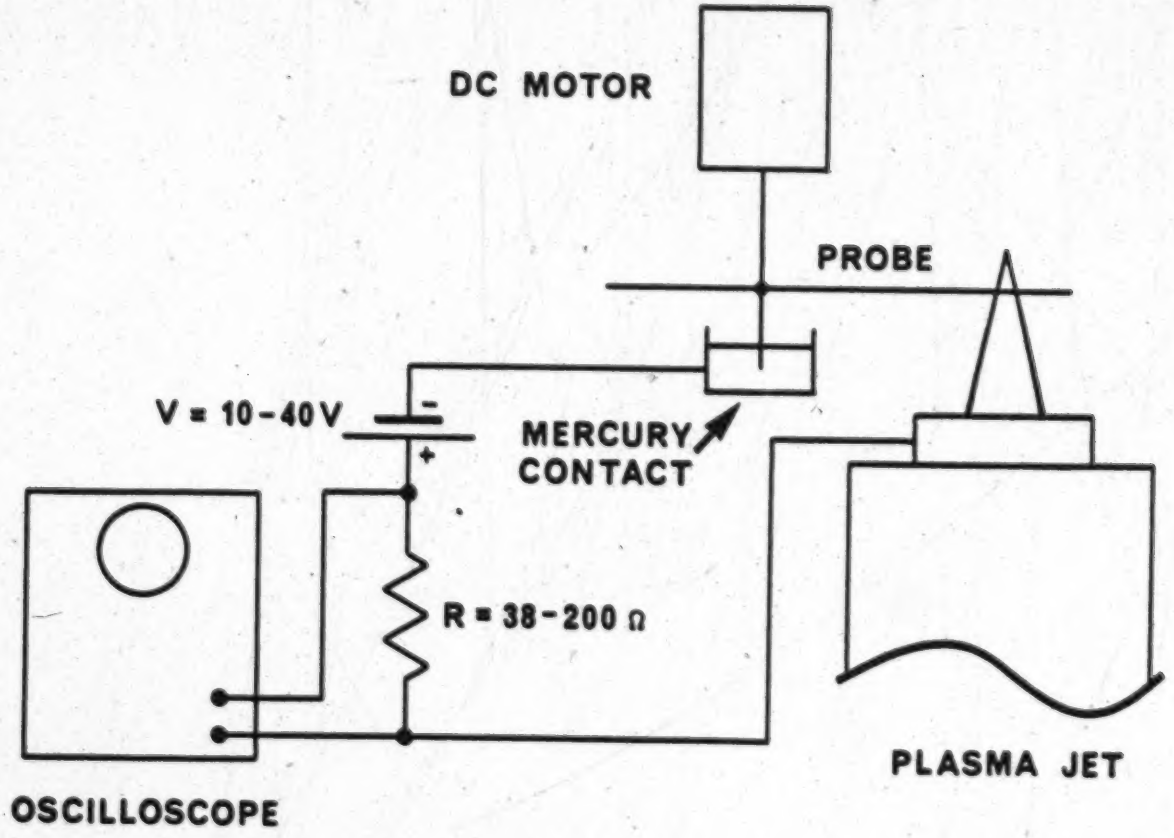

Fig. 2.6 Electrical circuit of the Langmuir probe.

Irising eliminated copious amounts of visible light.

A film of encapsulated liquid crystal on a mylar sheet (Edmund Scientific Co.) was used for detection of the radiation. Blue fringes due to local heating were obtained on a room-temperature green background.

In addition, the Langmuir probe 1cm long was scanned radially through the jet at a speed of 10 m/sec by a small motor. Radial dependence of the collected ion current was thus obtained from the temporal oscilloscope measurements. The probe circuit is shown in Fig. 2.6.

With the jet off and probe stationary over the anode, a probe image was obtained on the fringe pattern at the viewing screen. Thus interferometrically and probe determined densities could be compared at the exact same axial position.

These calibration measurements were done 1cm above the anode with jet operating conditions of 100 Amp. and flow rate of 80 cc/sec in order to obtain a distinct shifted pattern of fringes. Further results using only the probe were obtained at the same height and operating conditions used in the absorption measurements.

A glass-clad probe 0.625mm long was later used for comparison with the unfolded results of the long probe. These long and short probes were constructed of 0.250 and 0.375mm diameter wire respectively.

2.4.2 Absorption Results

From eqn. 2.18, the absorption constant for $\lambda = 10.6\mu$ is

$$\alpha = 1.8\times10^{-35} \frac{n_e^2}{T_e^{3/2}} \ cm^{-1} \qquad 2.25$$

where $n_e = cm^{-3}$ and T_e = eV are both functions of position. In the argon plasma jet $T_e \sim 1.2$ eV such that $\hbar\omega << KT_e$.

Since the jet is symmetrical about its axis, n_e and T_e are functions only of height h above the anode and radial distance r. Thus for a ray of light passing radially through the jet (h = constant) as shown in Fig. 2.7, the transmission is

$$T(y) = \exp\{-2 \int_y^{r_o} \frac{\alpha(r) r \, dr}{\sqrt{r^2-y^2}}\} \qquad 2.26$$

where y = chord distance and r_o = effective plasma radius. The ray trajectory has been assumed a straight line in view of the maximum observed total deflection of 0.5°. Thus the integrated absorption constant $<\alpha\ell>$ is

$$<\alpha\ell> = 2 \int_y^{r_o} \frac{\alpha(r) r \, dr}{\sqrt{r^2-y^2}} = -\ell n \, T(y) \qquad 2.27$$

which can be Abel inverted[8]

$$\alpha(r) = -\frac{1}{\pi} \int_r^{r_o} \frac{d<\alpha\ell>}{dy} \cdot \frac{dy}{\sqrt{y^2-r^2}} \, . \qquad 2.28$$

In terms of the measured quantity T;

$$\alpha(r) = \frac{1}{\pi} \int_r^{r_o} \frac{d\ell n T(y)}{dy} \cdot \frac{dy}{\sqrt{y^2-r^2}} \, . \qquad 2.29$$

Transmission data were taken for increments of 0.1mm in y. Identical values for positive and negative y reassured the assumption of plasma symmetry. These were unfolded according to eqn. 2.29 to obtain

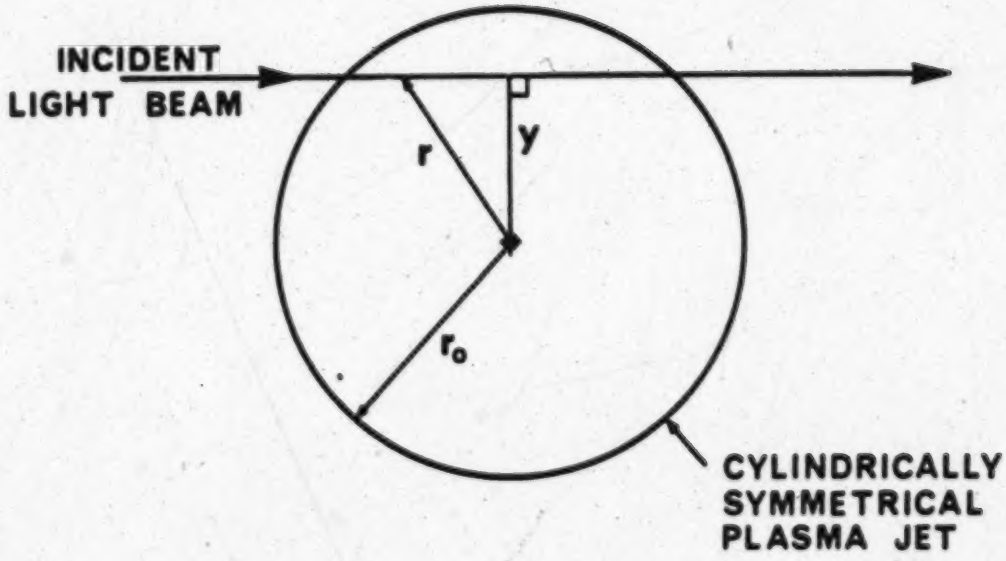

Fig. 2.7 Variables describing light ray passage through the jet.

$\alpha(r)$.

It is reasonable to assume that electron temperature scales with ion temperature since the latter is quite flat from the axis to the boundary region. Profiles of spectroscopically measured ion temperature[9] were used to describe $T_e(r)$. The axial $T_e(0)$ was taken as 1.2 eV. The radial profile of n_e was then calculated from eqn. 2.25 and unfolded $\alpha(r)$.

Fig. 2.8 shows this result along with that obtained by detailed interferometric measurements of Keilmann[10]. Both n_e and r have been normalized to the axial density and plasma radius respectively for purposes of direct comparison. The absolute density of 2.4×10^{17} cm^{-3} obtained here is in reasonable agreement with 1.4×10^{17} cm^{-3} obtained by Keilmann.

This variance as well as that in the effective radius r_o can be accounted for by the different construction and operation of each jet. In particular the jet used here had both a lower flow rate and a smaller anode orifice.

On the other hand, closer agreement in the shapes of the density profiles is expected since these are not critically dependent on the above mentioned jet parameters. The normalized profiles of Fig. 2.8 thus show that the absorption measurements do in fact give the plasma density fairly well. The substantial difference at large radii may be partly attributed to the finite size of the focused radiation whereby only part of the probe beam intercepts the plasma.

Axial transmission measurements ($y = 0$) were done from 3-12mm above the anode at a jet current of 300 Amp. and flow rate of 80 cc/sec. The unfolded axial density, normalized to its extrapolated value at 2.5mm is shown in Fig. 2.9. These results indicate a fairly linear

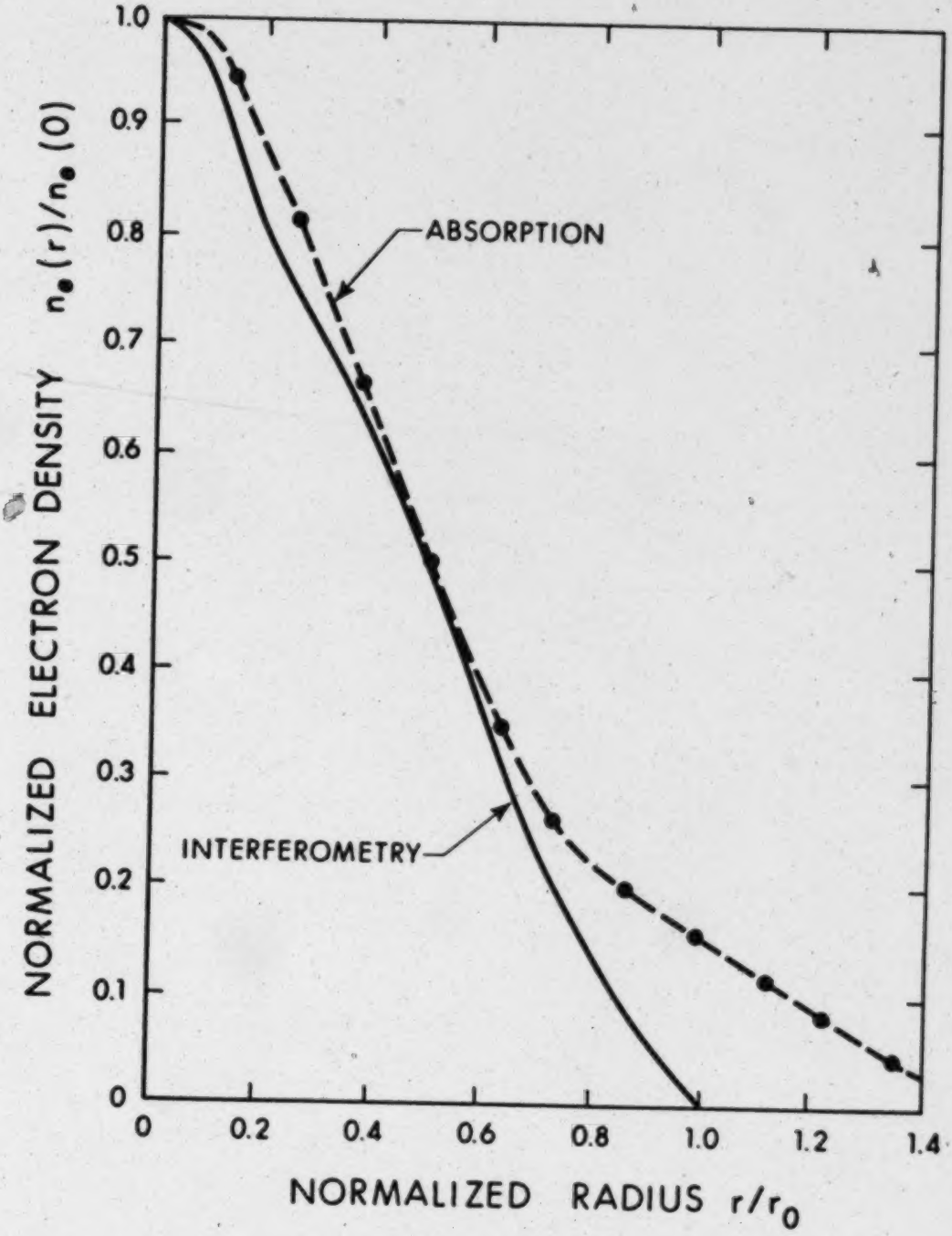

Fig. 2.8 Electron density vs radius in the jet determined from absorption measurements compared with the results of Keilmann.

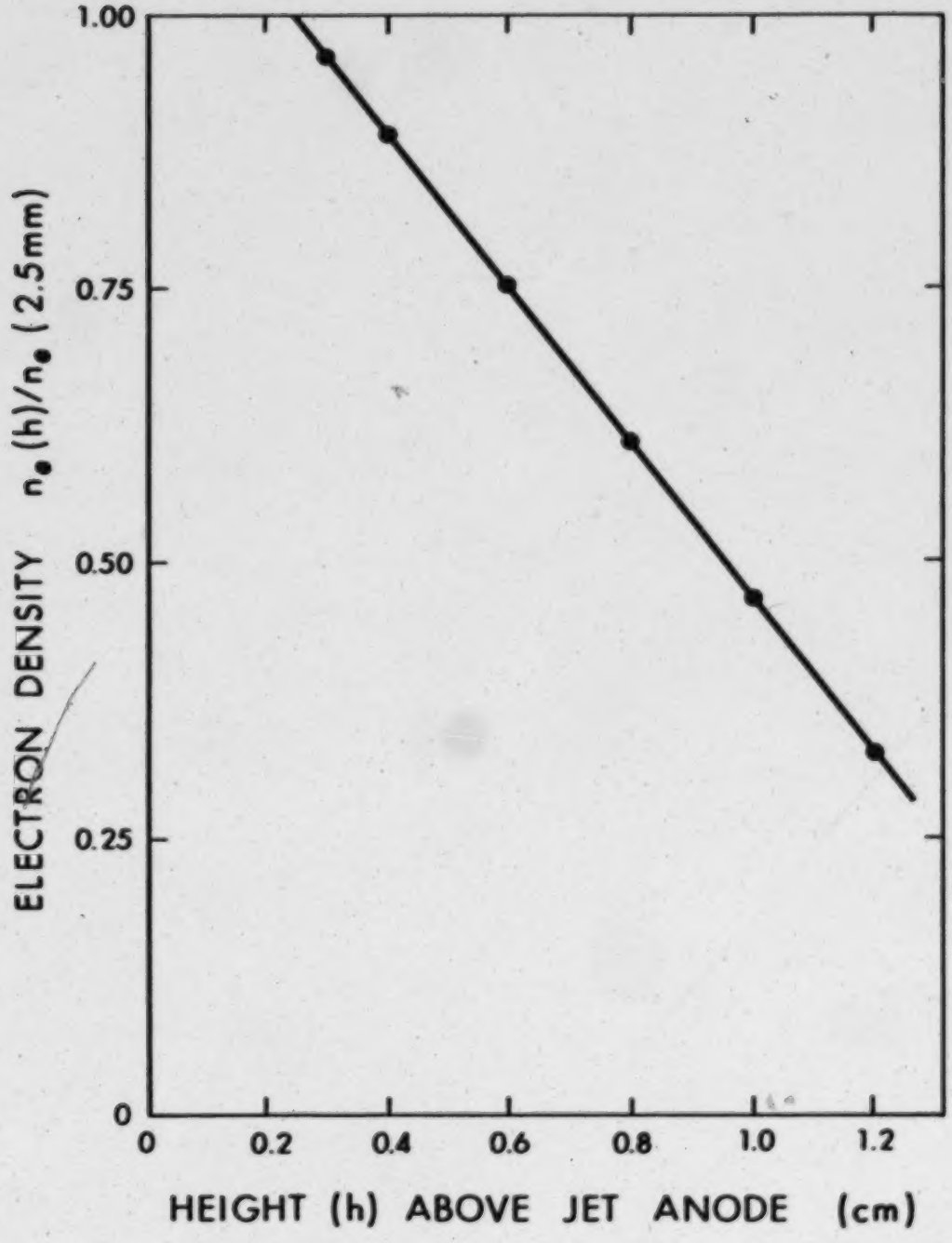

Fig. 2.9 Electron density vs height above the jet determined from absorption measurements.

density falloff with height from 3-12mm. Keilmann has also obtained a similar profile. An absolute value of $n_e(3mm) = 3.2x10^{17}$ cm^{-3} was obtained from these measurements. The value of $n_e(2.5mm) = 3.3x10^{17}$ cm^{-3} was used in the normalization.

2.4.3 Interferometer/Langmuir Probe Results

For the collision dominated plasma jet, the ion current I_i to the probe is predicted by convection dependent theory in flowing plasmas[11] which gives

$$I_i = 5.3(\epsilon_o e^3 \mu_i r_p v_f^3 n_e^3)^{1/4} V^{1/2} \ell \text{ (m.k.s. units)} \qquad 2.30$$

where ϵ_o = permitivity of free space, e = electronic charge, μ_i = ionic mobility, v_f = flow velocity of the plasma relative to the probe, r_p = probe radius, V = probe bias, and ℓ = probe length. This result applies to a long cylindrical probe with the plasma flow perpendicular to its axis.

The plasma velocity (in the lab frame) can be calculated from the volume flow of heated gas through the anode orifice. An effective temperature was taken as 9500°K corresponding to the typical ion and neutral temperature 7.5mm above the anode. From the orifice diameter of 4.5mm and cold flow rate of 80 cc/sec, $v_p \sim 150$ m/sec. The appropriate v_f is the vector sum of the probe velocity and the plasma velocity, but since the latter is much greater it is sufficient to take $v_f \sim v_p$. Including $\mu_i \sim 50$ cm^2/volt-sec and $r_p = 0.125$mm gives

$$I_i = 2.8\times10^{-14} n_e^{3/4} V^{1/2} \ell \qquad 2.31$$

for I = amps, $n_e = cm^{-3}$, V = volts, ℓ = cm.

This result applies to homogeneous plasmas. For the long probe in the jet, the total current is approximated by

$$I_i = 2.8\times10^{-14} V^{1/2} \cdot \int n_e^{3/4}(\ell)\, d\ell \qquad 2.32$$

where integration is through the full extent of the jet. This is reasonable since the scale length of substantial parameter variations is larger than the probe radius. A constant flow velocity has been assumed since this varies only linearly with temperature whereas $n_e \sim T_e^N$ (N >> 1) for partially ionized plasmas.

As with the absorption result of eqn. 2.27

$$I_i(y) = 2(2.8\times10^{-14} V^{1/2}) \int_y^{r_o} \frac{n_e^{3/4}(r)\, r\, dr}{\sqrt{r^2-y^2}} \qquad 2.33$$

which upon Abel inversion becomes

$$n_e^{3/4}(r) = \frac{-1}{\pi(2.8\times10^{-14} V^{1/2})} \int_r^{r_o} \frac{dI_i(y)}{dy} \cdot \frac{dy}{\sqrt{y^2-r^2}} \qquad 2.34$$

This was used to calculate $n_e(r)$ from the oscillograms obtained at h = 7.5mm with a jet current of 300 Amp. The additional short probe (ℓ = .625mm) was used to eliminate the unfolding process. Eqn. 2.31 was applied directly in this case.

Normalized results of both the long and short probes have been plotted in Fig. 2.10. Good agreement at small radii can be seen. It is interesting to note that the long probe results closely correspond

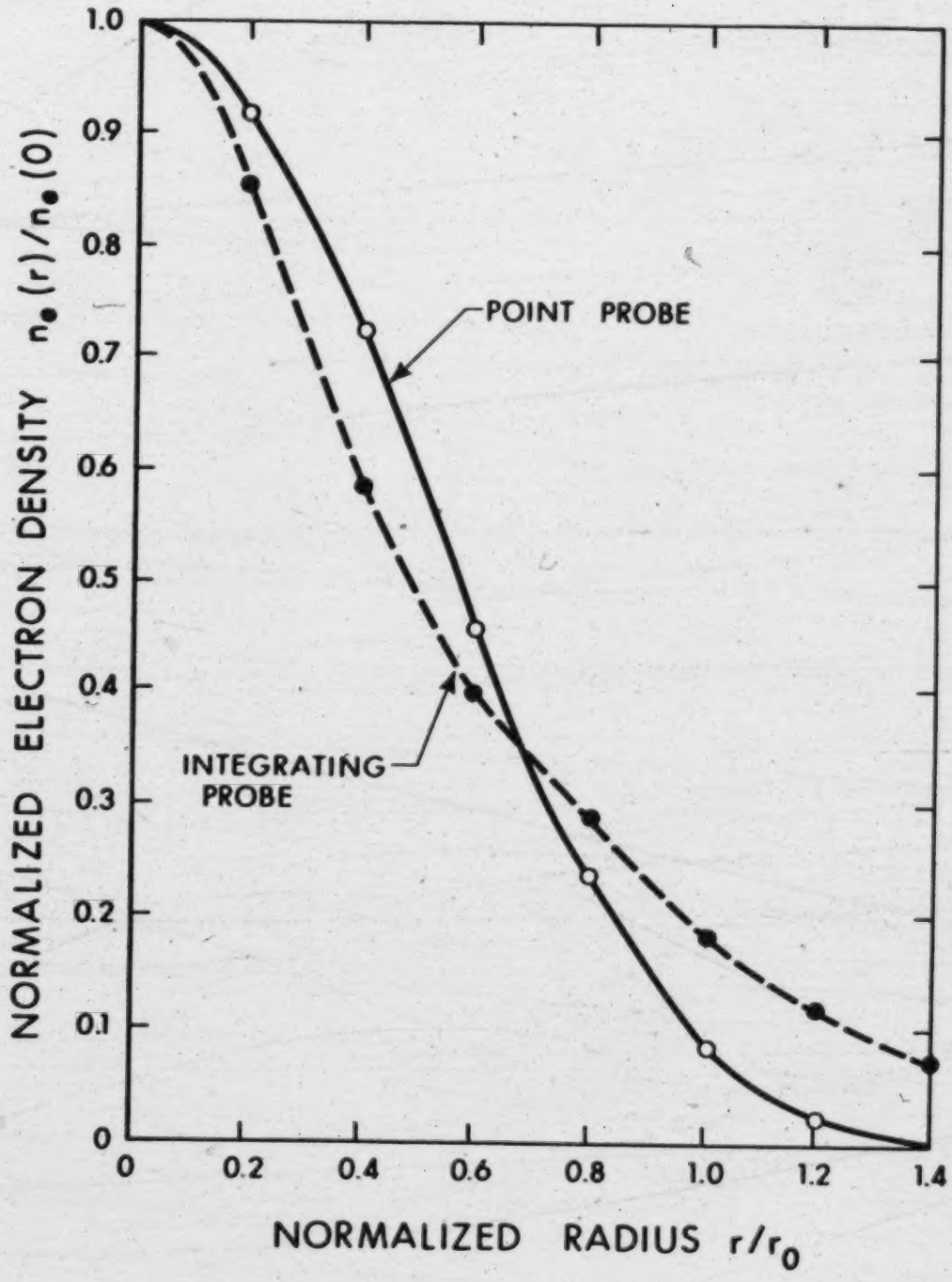

Fig. 2.10 Electron density vs radius in the jet determined from probe measurements.

to the previous absorption measurements (Fig. 2.8) for all r/r_o. Thus the density in this particular jet appears to have a profile resembling that obtained with the long probe. Calculation shows that inclusion of a finite size for both the probe and the focused laser light would give values only 10-15% lower than those plotted.

The short probe result is expected to underestimate the density at large radii since a fixed length had been taken. Near the plasma boundary however, the effective intersection of probe and plasma is somewhat shorter. In addition, collection of current at the end of the probe has been neglected.

The peak axial density obtained from the long probe was 2.1×10^{17} cm^{-3} while the short probe gave 3.2×10^{17} cm^{-3}.

Verification of the numerical validity of eqn. 2.30 was done at h = 1cm and a jet current of 100 Amp. as previously mentioned. A corrected value of v_p = 130 m/sec corresponding to the lower temperature of 8000°K was used in this case. The Mach-Zehnder interferometer gave an axial density of 5.9×10^{16} cm^{-3} while the long probe gave 5.1×10^{16} cm^{-3} under these conditions.

Reasonable agreement of these results thus allows confidence to be placed in the probe-measured values. Evidently eqn. 2.30 can be used to good approximation even for short probes with lengths only marginally greater than their radii under conditions similar to those in the jet.

2.5 Transient Interferometric and Absorption Measurements

2.5.1 Setup

This is shown in Fig. 2.11. Most of the details are the same

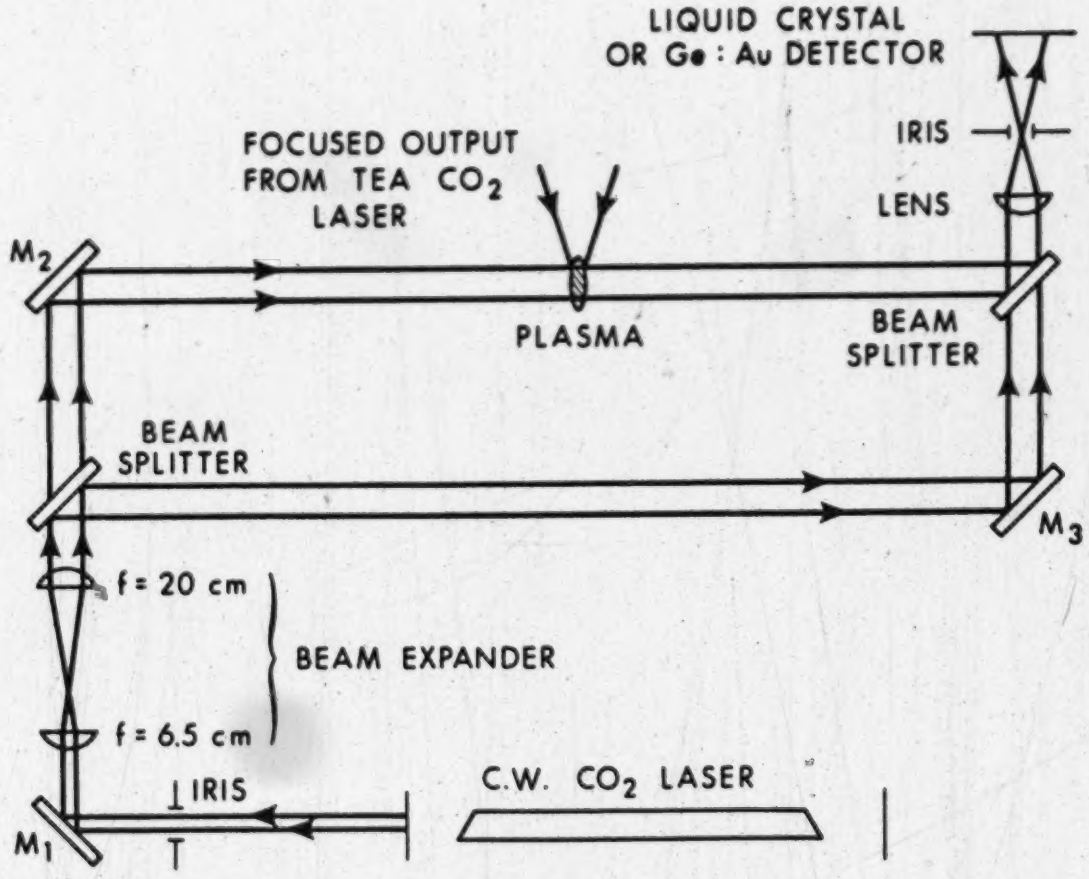

Fig. 2.11 Experimental setup for simultaneous absorption and interferometry.

as in the jet measurements and are not repeated here. The plasma was the spark produced at the focus of a 0.25J pin-type TEA CO_2 laser[12]. This was created in a flow of argon gas just above an inoperative plasma jet. The axis of the spark was perpendicular to the probe radiation.

The Mach-Zehnder interferometer was initially aligned using a liquid crystal viewing screen to permit visual observation of the fringes. This was subsequently replaced with a gold-doped germanium detector for the transient measurements. Loading of the detector to 100Ω gave adequate temporal resolution of < 100 ns.

It is important that the interferometer be aligned to give a fringe separation larger than the detector size (1.5mm diameter here). A maximum of beat amplitude is therefore obtained. The liquid crystal was found most useful for this purpose.

The 10.6μ probe laser was expanded using two lenses as shown. A lens at the output of the interferometer imaged the plasma onto a 1mm iris for substantial reduction of plasma emission and reflected TEA laser radiation seen by the detector. The viewing plane was placed beyond the iris in order to get a large fringe separation.

Relative transmission through the plasma measured at this point was the same as that measured at the location of the iris, thus plasma refraction was not important in the results obtained. Attenuation was also found to be independent of input beam diameter by varying the input iris aperture.

Additional rejection of plasma emission was obtained by using a > 10μ longpass filter. A removable chopper wheel was used for reference measurements of the unabsorbed radiation. The TEA laser was focused at the centre of the probe beam using a 10cm focal length NaCl

lens.

2.5.2 Results

Typical oscillograms obtained are shown in Fig. 2.12. A positive deflection represents absorption. With the reference arm of the interferometer blocked, only transient absorption (60%) is seen (a) while with both arms open, interference as well as absorption is detected (b).

That the power at $t \sim 60$ μs is larger than the quiesent value is the result of the detector not being at a position of maximum constructive interference with no plasma present. The large negative-going signal in the initial stage is due to reflection of TEA laser light into the viewing system. At these times large electron densities ($\omega_{pe} = \omega_{CO_2}$) with large gradients are present. Consequently, only the results for $t > 8$ μsec will be discussed.

Earlier times could be investigated by using a 9.4μ probe laser and a 9.4μ bandpass filter. Increased sensitivity of Ge:Au detectors at this wavelength might also be an asset. Alternatively, for a 10.6μ probe, a 9.4μ TEA laser could be used. These options however, were not available with the lasers used here. It should be mentioned that at very early times, the large densities with sharp gradients give correspondingly large refractive index gradients whereby refraction of the probe beam itself by the plasma may become too severe.

Only spatially averaged n_e and T_e were obtained since the resolution of the detection system was comparable to typical observed plasma diameters of $\lesssim$ 2mm. For the calculations, an effective

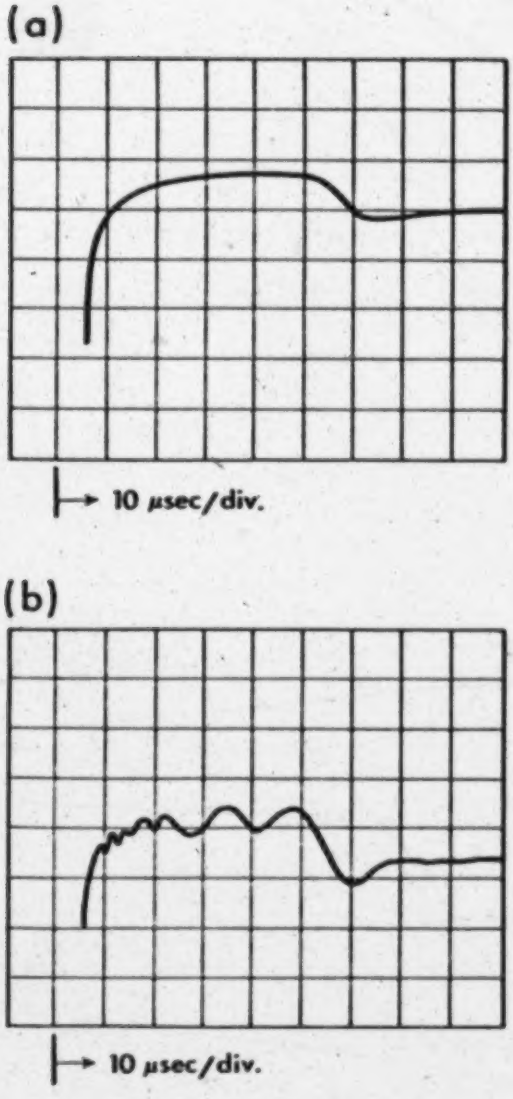

Fig. 2.12 Typical absorption and interference signals in the laser spark; (a) absorption only, (b) absorption plus interferometry.

thickness of 2mm was used.

A relatively constant absorption over the plasma duration (Fig. 2.12a) was found for this plasma. This enabled simple calculation of n_e and T_e since time variations with the reference arm open (Fig. 2.12b) were determined solely by the fringe shifts. Cases where temporally varying absorption is also present is discussed in the next section.

From eqn. 2.20, the fringe shifts

$$n = \frac{\langle \Delta n_R \rangle L}{\lambda_o} \qquad 2.35$$

where $\langle \Delta n_R \rangle$ = average change in refractive index. For L = 2mm and $n \leq 7$ here, $\langle \Delta n_R \rangle << 1$ whereby $n_R \approx 1$. Thus the refractive index can be approximated by

$$n_R = \sqrt{1 - \frac{\omega_{pe}^2}{\omega^2}} = 1 - \frac{r_o \lambda_o^2}{2\pi} n_e \qquad 2.36$$

where r_o = classical electron radius. Determination of n_e from the fringe shifts then follows from

$$n_e = \left(\frac{2\pi}{r_o \lambda_o L}\right)|n| = 1.06 \times 10^{17} |n| \text{ cm}^{-3} \qquad 2.37$$

for λ_o = 10.6μ and L = 2mm.

The absorption constant was taken as

$$\alpha = 1.6 \times 10^{-35} \frac{\lambda_\mu^2 n_e^2}{T_e^{3/2}} \left[\frac{1 - e^{-\hbar\omega/T_e}}{\hbar\omega/T_e}\right] \qquad 2.38$$

for λ_μ = microns, n_e = cm^{-3} and T_e = eV.

The last factor (see eqn. 2.16) corrects for low temperatures in the late stages where $T_e \to \hbar\omega$. $\bar{G}$ has been set equal to 1; a reasonable assumption since theoretical models[2] give $\bar{G}(T_e = \hbar\omega) \approx 1$. For 10.6μ radiation $\hbar\omega = 0.117$ eV.

Calculated average density and temperature using eqns. 2.37 and 2.38 are shown in Fig. 2.13 as a function of time. Points were calculated at integral numbers of fringe shifts.

These time-dependent results allow determination of the recombination coefficient. For prevailing three-body collisional-radiative decay, the density evolves according to

$$\frac{dn_e}{dt} = -\beta n_e^2 \qquad 2.39$$

where β = recombination coefficient and which has the solution

$$\frac{1}{n_e(t)} = \frac{1}{n_e(0)} + \beta t \ . \qquad 2.40$$

A plot of measured reciprocal density versus time is given in Fig. 2.14. Two linear regions are obtained. For t = 8-13 μsec, $\beta = 1.1\times10^{-13}$ cm^3 sec^{-1} and for t = 13-30 μsec, $\beta = 1.4\times10^{-13}$ cm^3 sec^{-1}. The larger value for late times may be related to the lower temperature where increased collision frequencies are expected.

Recombination thus is slower in argon than in helium for which $\beta = 6\times10^{-12}$ cm^3 sec^{-1} has been obtained spectroscopically by George et al[13]. To verify this, helium was substituted for argon in the setup of Fig. 2.11. The absorption-interference was found to be shorter lived by a factor of about 5, showing that the helium

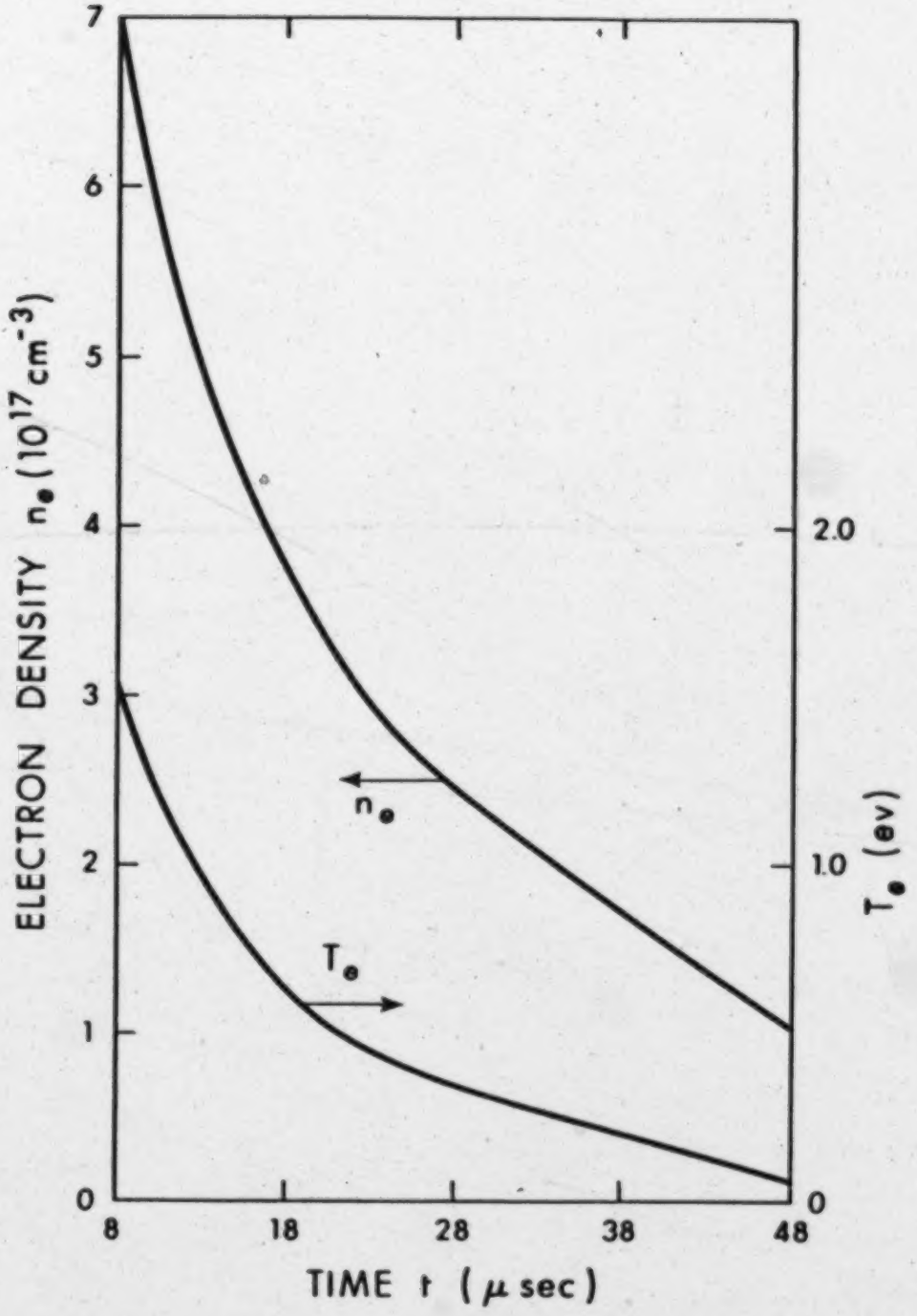

Fig. 2.13 Temporal electron density and temperature in the laser spark. Uncertainties are due to oscilloscope errors.

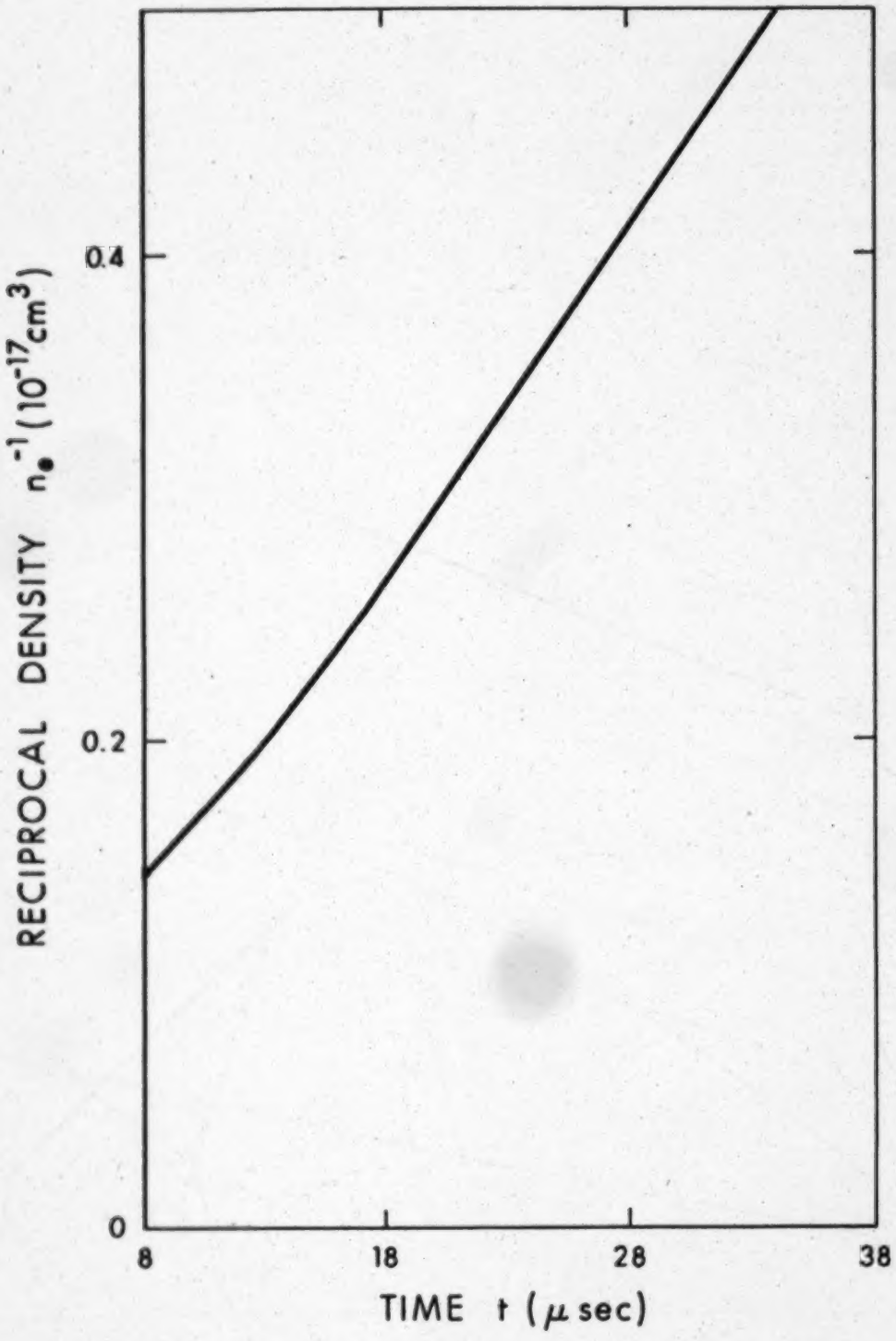

Fig. 2.14 Reciprocal electron denisty in the laser spark.

recombination is indeed faster. Detailed measurements for helium were not possible here because of the large reflection of TEA laser radiation at early times.

The foregoing results show that simultaneous CO_2 laser interferometry and absorption provide a convenient technique for temporal determination of density and temperature in transient, moderately dense plasmas. Use of the 9.4μ/10.6μ system previously mentioned to eliminate the TEA laser reflection problem would be a simple method for measuring recombination coefficients in different gases.

2.5.3 Concurrently Time-Varying α and n_R

For a Mach-Zehnder interferometer, it is relatively simple to show that the power seen by a square-law detector at the output is given by

$$P = TP_1 + P_2 + 2\sqrt{P_1 P_2}\sqrt{T}\cos(\phi+\Delta K_R \ell) \qquad 2.41$$

where P_2 = reference beam power, P_1 = initial power in the beam passing through the plasma of length ℓ and transmission T, $\Delta K_R = (n_R-1)\omega/c$, and ϕ = phase angle depending only on alignment of the optical system. For temporally varying n_e and T_e (slow compared to the reciprocal detector bandwidth), ΔK_R and T are functions of time. Ambiguity is obvious when both of these are changing at the same rate or if the transmission is oscillatory.

However, this problem can be eliminated by using a two-detector arrangement as shown in Fig. 2.15. A third beam splitter allows the

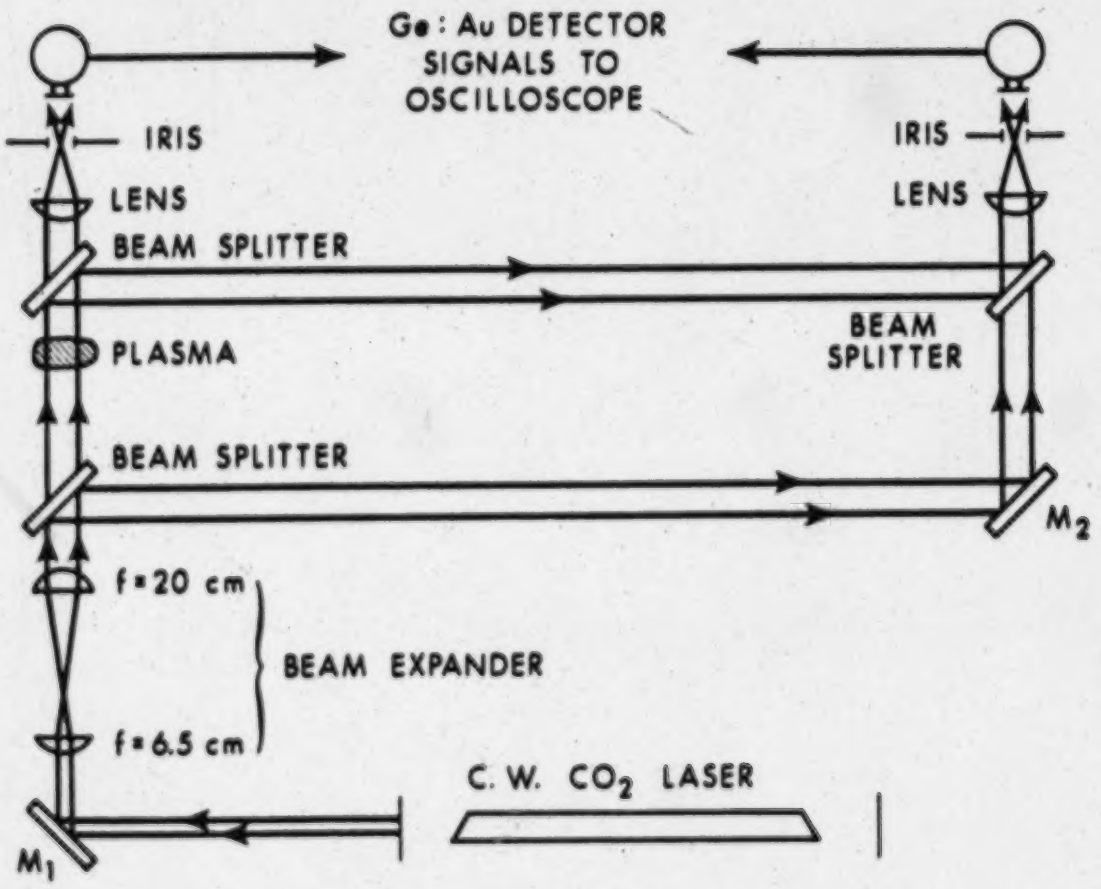

Fig. 2.15 Two-detector Mach-Zehnder interferometer for simultaneous absorption and interferometry.

second detector to see only the attenuation. This direct measure of T(t) can subsequently be used to calculate $\Delta K_R(t)$ from the original detector output by eqn. 2.41 above.

Thus with the use of two detectors, simultaneous interferometry and absorption is a general technique for temporal determination of both electron density and temperature.

CHAPTER III

THOMSON SCATTERING

3.1 Introduction

Thomson scattering of laser radiation in the wavelength range 0.5 - 0.7μ has been used extensively as a reliable plasma diagnostic. Experiments since the first theoretical descriptions of the process[1,2,3] have measured both cooperative and incoherent scattered spectra from a variety of plasmas by utilizing chiefly ruby lasers for the high incident power required (cross-section $\sim 10^{-25}$ cm^2).

In addition to thermal fluctuations, Thomson scattering has been observed from non-thermal fluctuations occurring in turbulent plasmas[4,5] and those induced by non-linear mixing of laser light in Maxwellian plasmas[6].

Many of these experiments are summarized in a recent review paper by Evans and Katzenstein[7].

Cooperative spectra have been observed but only from plasmas of at least moderate density (>10^{15} cm^{-3}). For lower density plasmas, use of short wavelengths (0.5 - 0.7μ) requires exceedingly small scattering angles and collection solid angles resulting in excessive stray light and detector noise problems.

On the other hand, very few experiments utilizing CO_2 laser light (λ = 10.6μ) for Thomson scattering have been reported[8,9,10]. This long wavelength radiation is of much interest for cooperative scattering from low density plasmas since it enables large scattering angles to be used and requires less resolving power for spectral analysis.

For high density plasmas, 10.6μ radiation establishes a highly cooperative Thomson scattering regime. In this case, the spectra of fluctuations with wavelengths much larger than collisional mean free paths can be obtained. Such measurements of collision-dominated scattering have not been previously reported using shorter wavelength radiation.

In addition to the above mentioned thermal fluctuations, 10.6μ radiation can be used to probe long-wavelength non-thermal fluctuations such as those expected in CO_2 laser-produced plasmas. These measurements could prove very useful for a more complete understanding of the non-linear coupling of high power CO_2 laser radiation to plasmas which are of current interest in laser fusion.

Three experiments utilizing CO_2 laser radiation for Thomson scattering are described here. The first experiment undertaken was to measure the mildly cooperative (α = 2) scattered spectrum from a low density ($n_e \sim 5 \times 10^{13}$ cm^{-3}) hollow cathode discharge. In the second, a collision-dominated spectrum has been obtained by using a high density argon plasma jet. Finally, enhanced scattering of 10.6μ radiation has been observed from a hydrogen plasma produced by a TEA CO_2 laser operating at λ = 9.6μ.

Description of these experiments is first preceded by a summary of the pertinent Thomson scattering theory.

3.2 Theory

3.2.1 Scattering from a Collisionless Maxwellian Plasma

The detailed calculations of Thomson scattering from a collisionless Maxwellian plasma appear throughout the literature[1,2,3]. In the following, these results will be summarized in terms of standard tabulated functions.

Thomson scattering is the re-radiation from charged particles accelerated by an incident high frequency electromagnetic wave. Thus scattering from ions is negligible compared to that of the much lighter electrons.

For a plasma, contributions from the large number of electrons can be summed, accounting for time-varying spatial phase differences, into a general form

$$dP_s = N_e \sigma_T S(\underline{k},\omega) I_o d\omega d\Omega \qquad 3.1$$

where N_e = total number of electrons contributing to the scattering

$\sigma_T = r_o^2 \sin^2\beta$ = Thomson cross-section for one electron

r_o = classical electron radius

β = angle between incident electric field and $\underline{k}_s$

$\underline{k}_s$ = wavevector of scattered radiation

$\underline{k}_i$ = wavevector of incident radiation

$\underline{k} = \underline{k}_s - \underline{k}_i$ = scattering wavevector

ω_o = incident wave frequency

ω_s = scattered wave frequency

$\omega = \omega_s - \omega_i$

$S(\underline{k},\omega)$ = effective form factor

I_o = incident wave intensity

dP_s = power scattered in a frequency band $d\omega$ about ω_s into a solid angle $d\Omega$ about $\underline{k}_s$.

Experimentally, scattered light is usually collected from the full cross-section of incident radiation such that $N_e = n_e A\ell$ and $I_o = P_o/A$ where n_e = electron density and P_o = incident power. Thus in this case

$$dP_s = n_e \sigma_T \, S(\underline{k},\omega) P_o \ell \, d\omega d\Omega \quad . \tag{3.2}$$

The form factor $S(\underline{k},\omega)$, which accounts for the position and motion of all the electrons in the plasma, is the spatially and temporally Fourier transformed electron density autocorrelation function

$$S(\underline{k},\omega) = \frac{1}{2\pi} \int e^{i(\omega\tau - \underline{k}\cdot\underline{\rho})} d\underline{\rho} d\tau \lim_{V,T\to\infty} \left\{ \frac{1}{n_{eo} VT} \cdot \int n_e(\underline{r},t) n_e(\underline{r}+\underline{\rho},t+\tau) d\underline{r} dt \right\} \tag{3.3}$$

where n_{eo} = average electron density.

The above results are quite general and describe the Thomson scattered spectrum from any given plasma providing the autocorrelation of n_e is known.

For a collisionless Maxwellian plasma this can be calculated using linearized Vlasov equations for electrons and ions. Although ions do not appreciably scatter the incident radiation, they are electrostatically coupled to electrons and therefore also affect the scattered spectrum.

In this case the form factor is given by

$$S(\underline{k},\omega) = \left|\frac{1-G_i}{1-G_e-G_i}\right|^2 \frac{F_{em}(\frac{\omega}{k})}{k} + Z\left|\frac{G_e}{1-G_e-G_i}\right|^2 \frac{F_{im}(\frac{\omega}{k})}{k} \qquad 3.4$$

where $$G_{e,i}(\underline{k},\omega) = \frac{\omega_{pe,i}^2}{k^2}\int \frac{\underline{k}\cdot\frac{\partial f_{e,im}(\underline{v})}{\partial \underline{v}}}{\underline{k}\cdot\underline{v}-\omega}\, d\underline{v} \qquad 3.5$$

$$f_{e,im}(\underline{v}) = \frac{1}{(\pi v_{e,i}^2)^{3/2}} e^{-(v/v_{e,i})^2} \qquad 3.6$$

$$v_{e,i} = \left(\frac{2k_B T_{e,i}}{m_{e,i}}\right)^{1/2} \qquad 3.7$$

$$F_{e,im}(v) = \frac{1}{\sqrt{\pi}v_{e,i}} e^{-(v/v_{e,i})^2} \quad . \qquad 3.8$$

It should be noted that the factor $\varepsilon(\underline{k},\omega) = 1-G_e-G_i$ appearing in the denominator is simply the dielectric constant for electrostatic plasma waves with wavevector $\underline{k}$ and frequency ω. Thus the scattering cross-section is large for $\varepsilon \to 0$.

A further simplification of S is obtained by using a normalized frequency shift x and a scattering parameter α:

$$x_{e,i} \equiv \frac{\omega}{kv_{e,i}} \qquad 3.9$$

$$\alpha \equiv \frac{1}{k\lambda_{De}} \qquad 3.10$$

$$\lambda_{De} = \left(\frac{k_B T_e}{4\pi n_e e^2}\right)^{1/2}$$

whereby both G_e and G_i can be rewritten in terms of a new function $W(x)$:

$$G_e = -\alpha^2 W(x_e) \qquad 3.11$$

$$G_i = -Z\left(\frac{T_e}{T_i}\right)\alpha^2 W(x_i) \qquad 3.12$$

with

$$W(x) = 1-2xe^{-x^2}\int_0^x e^{p^2}dp - i\sqrt{\pi}\,xe^{-x^2} \qquad 3.13$$

being the evaluation of the singular Landau-type integrals. A plot of the real and imaginary parts of W is shown in Fig. 3.1. Thus

$$S(\underline{k},\omega)d\omega = \left|\frac{1+Z\left(\frac{T_e}{T_i}\right)\alpha^2 W(x_i)}{1+Z\left(\frac{T_e}{T_i}\right)\alpha^2 W(x_i)+\alpha^2 W(x_e)}\right|^2 \frac{e^{-x_e^2}}{\sqrt{\pi}}\,dx_e$$

$$+ Z\left|\frac{\alpha^2 W(x_e)}{1+Z\left(\frac{T_e}{T_i}\right)\alpha^2 W(x_i)+\alpha^2 W(x_e)}\right|^2 \frac{e^{-x_i^2}}{\sqrt{\pi}}\,dx_i \,. \qquad 3.14$$

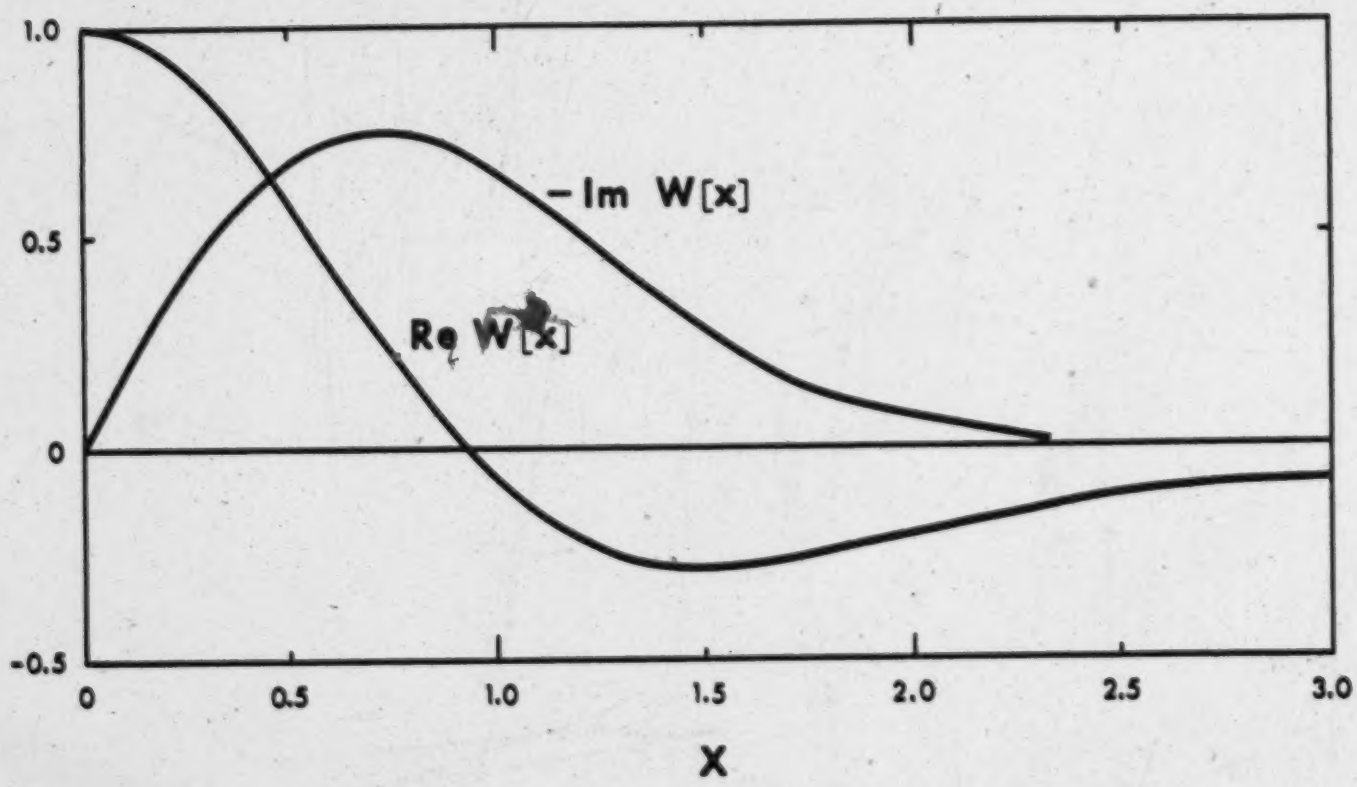

Fig. 3.1 The function W(x).

A useful approximation of $x_e << x_i$ due to Salpeter[3] can be made if the ion temperature does not exceed the electron temperature. Since $dx_e << dx_i$ the first term is greater than the second only for $x_i >> 1$ in which case $W(x_i) \sim W(\infty) = 0$ may be taken. For values of $x_i \lesssim 1$ the second term dominates and it is sufficiently accurate to set $W(x_e) \sim W(0) = 1$ in this case. Thus $W(x_i)$ can be neglected in the first term and $W(x_e)$ set equal to 1 in the second. With these approximations

$$S(\underline{k},\omega)d\omega \approx \left|\frac{1}{1+\alpha^2 W(x_e)}\right|^2 \frac{e^{-x_e^2}}{\sqrt{\pi}}\, dx_e + Z\left(\frac{\alpha^2}{1+\alpha^2}\right)^2 \left|\frac{1}{1+\frac{\alpha^2}{1+\alpha^2} Z\left(\frac{T_e}{T_i}\right) W(x_i)}\right|^2 \frac{e^{-x_i^2}}{\sqrt{\pi}}\, dx_i \qquad 3.15$$

where each term is now independently a function of either x_e or x_i.

The similarity of these terms suggests definition of another function Γ:

$$\Gamma_\alpha(x) \equiv \frac{e^{-x^2}}{\sqrt{\pi}\left|1+\alpha^2 W(x)\right|^2} \qquad 3.16$$

such that

$$S(\underline{k},\omega)d\omega = \Gamma_\alpha(x_e)dx_e + Z\left(\frac{\alpha^2}{1+\alpha^2}\right)^2 \Gamma_\beta(x_i)dx_i \qquad 3.17$$

where

$$\beta^2 = Z\left(\frac{T_e}{T_i}\right)\left(\frac{\alpha^2}{1+\alpha^2}\right) .$$

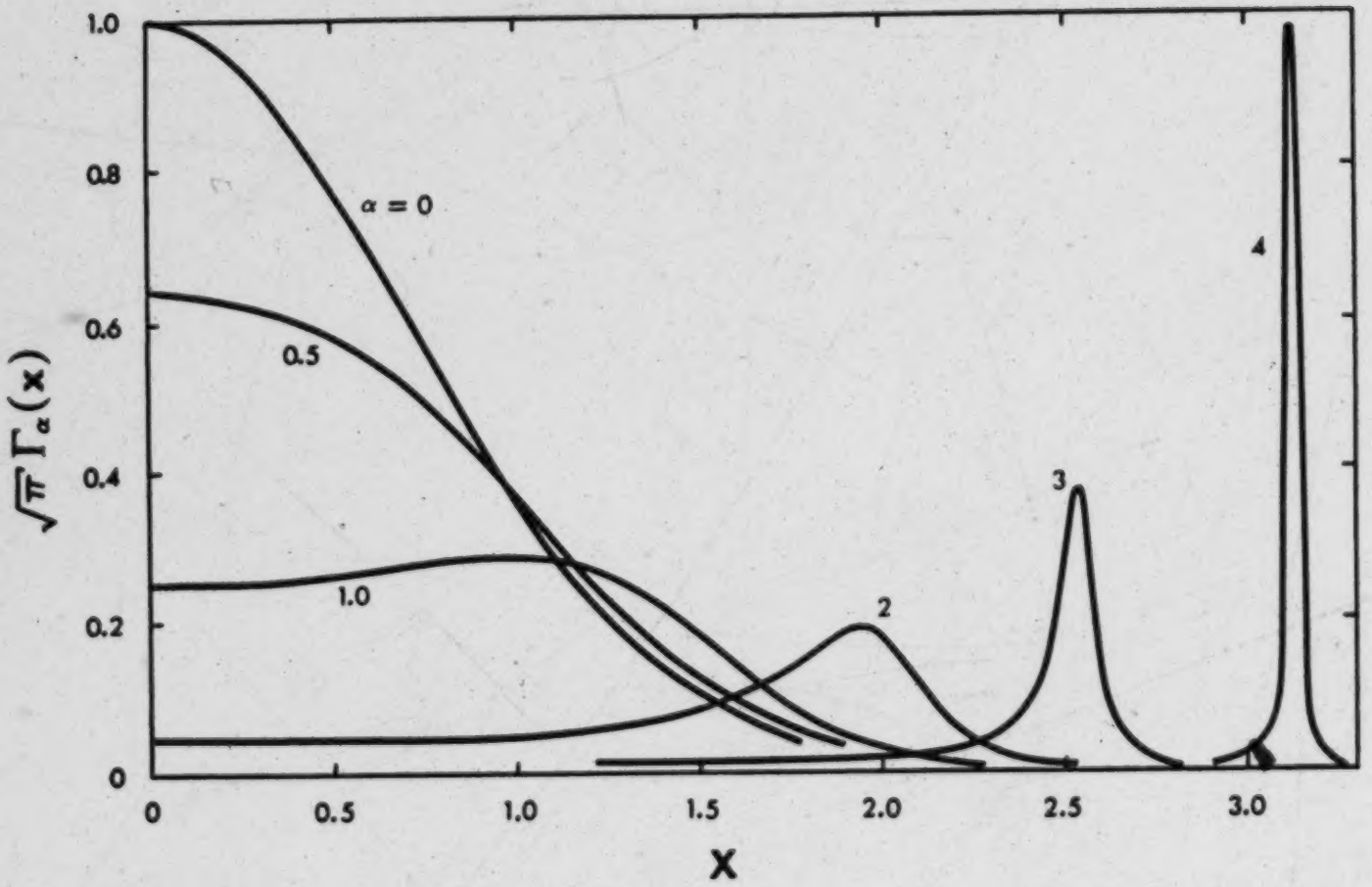

Fig. 3.2 The function $\Gamma_\alpha(x)$ (after Salpeter).

Several plots of Γ for various values of α are shown in Fig. 3.2.

Finally, integration of Γ over all x is given by

$$\int_{-\infty}^{\infty} \Gamma_\alpha(x)dx = \frac{1}{1+\alpha^2} \qquad 3.18$$

and thus the spectrally integrated form factor is

$$S(\underline{k}) = \frac{1+\alpha^2\left(1+Z\frac{T_e}{T_i}\right)+Z\alpha^4}{\left\{1+\alpha^2\left(1+Z\frac{T_e}{T_i}\right)\right\}\left\{1+\alpha^2\right\}} \qquad 3.19$$

In the limit of $\alpha \ll 1$,

$$S(\underline{k},\omega) = \frac{e^{-x_e^2}}{\sqrt{\pi}}\,dx_e \qquad 3.20$$

which is simply a Doppler-broadened spectrum. Thus T_e can be obtained directly from the linewidth ($\Delta\omega \sim kv_e$). Here scattering occurs from density fluctuations with wavelengths short compared to λ_{De} (individual electrons); collective effects are negligible because of strong Landau damping ($k\lambda_{De} \gg 1$).

On the other hand, for $\alpha \gg 1$ coherent plasma oscillations dominate the scattered spectrum. Electron satellites are obtained at a frequency shift

$$\omega = \pm \omega_{pe}\left[1 + \frac{3}{\alpha^2}\right]^{1/2} \qquad 3.21$$

and have a width governed by Landau damping:

$$\Delta\omega = \omega_{pe}\sqrt{\frac{\pi}{2}}\,(\alpha^2+3)^{3/2}\,\exp\left\{-\left(\frac{\alpha^2+3}{2}\right)\right\} \quad . \qquad 3.22$$

These satellites are therefore very narrow for large α. The electron density can be accurately found from the measurement of this shift since absolute intensity calibration of the collection optics is not required as would be if the spectrally integrated scattering were used to determine n_e (see eqn. 3.2). However,as can be seen from eqn. 3.18 only $1/2\alpha^2$ of the total scattered power is contained in each satellite.

The bulk of the scattered spectrum for $\alpha \gg 1$ is described by

$$S(\underline{k},\omega)d\omega \simeq Z\,\Gamma_\beta(x_i)dx_i \quad . \qquad 3.23$$

The ion temperature can therefore be determined directly from a measurement of the width of this distinct ion feature ($\Delta\omega \sim kv_i$). This width as does that of the electron satellites decreases with increasing α ($\Delta\omega \sim kv_i \sim v_i(\alpha\lambda_{De})^{-1}$). It should be noted that since the shape of the scattered spectrum depends on β, T_e can also be determined from spectral measurements for $\alpha \gg 1$.

Experimentally, values of $\alpha \gtrsim 1$ are usually chosen for cooperative Thomson scattering since less spectral resolution is required than for very large α (see Fig. 3.2).

3.2.2 Collision-Dominated Scattering

The effects of collisions on the Thomson scattered spectrum from Maxwellian plasmas for the limiting cases of $\alpha \ll 1$ and $\alpha \gg 1$ are

discussed by Fejer[1]. Subsequent calculations[11,12,13] have extended the theory for general α. The results of Grewal[11] will be summarized here.

In order to incorporate collisions, Fokker-Planck equations of the form

$$\left[\frac{\partial}{\partial t} + \underline{v}\cdot\frac{\partial}{\partial \underline{r}} + \frac{q_{e,i}}{m_{e,i}}\underline{E}_{int}\cdot\frac{\partial}{\partial \underline{v}} - \nu_{e,i}\frac{\partial}{\partial \underline{v}}\left\{\underline{v} + \frac{k_B T_{e,i}}{m_{e,i}}\frac{\partial}{\partial \underline{v}}\right\}\right] f_{e,i}(\underline{r},\underline{v},t) = 0 \qquad 3.24$$

are used for both electrons and ions. Here $\underline{E}_{int}$ = local electrostatic field and ν = effective collision frequency. Defining collisional parameters

$$p_{e,i} \equiv \frac{\nu_{e,i}}{k v_{e,i}} = \frac{1}{k(\lambda_{mfp})_{e,i}} \qquad 3.25$$

the function W(x) (see eqn. 3.13) modified to include collisions becomes

$$W^C(x_j) = 1 - i x_j F^*(x_j) \qquad 3.26$$

where

$$F(x_j) = \int_0^\infty e^{i x_j y} \exp\left\{-\frac{1}{p_j^2}\left[\exp(-p_j y) + p_j y - 1\right]\right\} dy \qquad 3.27$$

and * denotes the complex conjugate.

The form factor can then be written as

$$S(\underline{k},\omega)d\omega = \left| \frac{1 + \alpha^2 Z\left(\frac{T_e}{T_i}\right) W^c(x_i)}{1 + \alpha^2 W^c(x_e) + \alpha^2 Z\left(\frac{T_e}{T_i}\right) W^c(x_i)} \right|^2 \left\{ \text{Re } F(x_e) \right\} \frac{dx_e}{\pi}$$

$$+ Z \left| \frac{\alpha^2 W^c(x_e)}{1 + \alpha^2 W^c(x_e) + \alpha^2 Z\left(\frac{T_e}{T_i}\right) W^c(x_i)} \right|^2 \left\{ \text{Re } F(x_i) \right\} \frac{dx_i}{\pi}. \qquad 3.28$$

Taking the Salpeter approximation ($x_e \ll x_i$) to be valid and $p_e = p_i$,

$$S(\underline{k},\omega)d\omega = \Gamma_\alpha^c(x_e)dx_e + Z\left(\frac{\alpha^2}{1+\alpha^2}\right)^2 \Gamma_\beta^c(x_i)dx_i \qquad 3.29$$

where $\beta^2 = Z\left(\frac{T_e}{T_i}\right)\left(\frac{\alpha^2}{1+\alpha^2}\right)$

and $$\Gamma_\alpha^c(x) = \frac{\text{Re } F(x)}{\pi \left| 1+\alpha^2 W^c(x) \right|^2} \qquad 3.30$$

Thus in general, the Thomson scattered spectrum is characterized by a collisional parameter $p = (k\lambda_{mfp})^{-1}$ in addition to the normal scattering parameter $\alpha = (k\lambda_{De})^{-1}$.

In the limit of $p \to 0$ $(\nu \to 0)$,

$$F(x) \to \sqrt{\pi} e^{-x^2} + 2ie^{-x^2} \int_0^x e^{y^2} dy \qquad 3.31$$

and $$W^c(x) \to 1 - 2xe^{-x^2} \int_0^x e^{y^2} dy - i\sqrt{\pi} xe^{-x^2} = W(x) \qquad 3.32$$

whereby eqns. 3.29 and 3.30 reduce to the previously discussed collisionless results.

In the limit of $p \to \infty$,

$$F(x) \to \frac{2p(1+2ipx)}{1+4p^2x^2} \tag{3.33}$$

$$W^c(x) \to \frac{1}{1+4p^2x^2} - i\,\frac{2px}{1+4p^2x^2} \tag{3.34}$$

whereby $$\Gamma_\alpha^c(x) \to \frac{2p}{\pi\left[4p^2x^2 + (1+\alpha^2)^2\right]} \tag{3.35}$$

and $$S(\underline{k},\omega)d\omega \to \frac{2p_e}{1+4p_e^2x_e^2}\,\frac{dx_e}{\pi} \quad \text{for} \quad \alpha \ll 1 \tag{3.36}$$

$$\to \frac{2p_i}{(1+\beta^2)^2+4p_i^2x_i^2}\,\frac{dx_i}{\pi} \quad \text{for} \quad \alpha \gg 1\,. \tag{3.37}$$

Thus collision-dominated Thomson scattering has a Lorentzian lineshape and spectral width that decreases with increasing values of p.

Although the spectral shape is a function of p, the integrated scattering is independent of p:

$$\int_{-\infty}^{\infty} \Gamma_\alpha^c(x)dx = \frac{1}{1+\alpha^2} \tag{3.38}$$

which is the same result as for collisionless plasmas.

For highly cooperative scattering ($\alpha \gg 1$), the scattered spectrum essentially consists of a dominant central ion feature

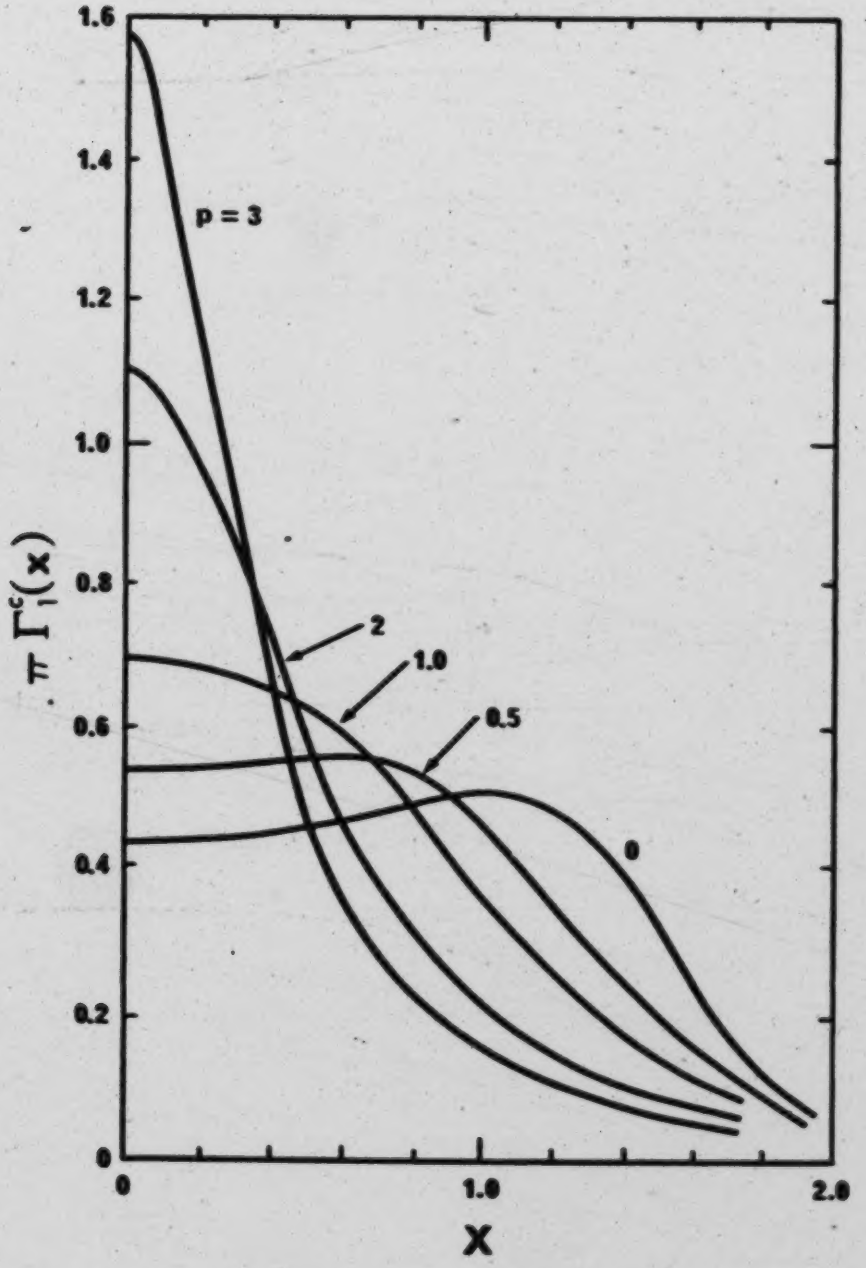

Fig. 3.3 The function $\Gamma_1^c(x)$ (after Grewal).

$$S(\underline{k},\omega)d\omega = Z\left(\frac{\alpha^2}{1+\alpha^2}\right)^2 \Gamma_\beta^c(x_i)dx_i \ . \qquad 3.39$$

The transition of Γ_β^c from the collisionless to collision-dominated regime is shown in Fig. 3.3 for $\beta = 1$. As expected, collisional effects become quite important for $p \gtrsim 1$.

Large α scattering from a highly collisional plasma is therefore expected to show substantial narrowing of the central ion feature (by a factor of $\sim 1.6\ p_i$) along with disappearance of the ion acoustic resonances found for a collisionless plasma. In this case the scattered spectrum is described by eqn. 3.37.

3.2.3 Enhanced Thomson Scattering

The previous two sections have dealt with Thomson scattering from thermal fluctuations. The specific case of scattering from fluctuations induced by non-linear mixing of two intense high frequency ($\omega > \omega_{pe}$) electromagnetic waves in a plasma will be discussed here.

It will be assumed that the plasma is collisionless and that no constant external magnetic field is present. Two monochromatic plane electromagnetic waves are considered:

$$\underline{E}_{1,2}(\underline{r},t) = \underline{E}_{1,2}\cos(\underline{k}_{1,2}\cdot\underline{r} - \omega_{1,2}t)$$

$$\underline{B}_{1,2}(\underline{r},t) = \underline{B}_{1,2}\cos(\underline{k}_{1,2}\cdot\underline{r} - \omega_{1,2}t) \ . \qquad 3.40$$

The electron and ion distribution functions $f_e(\underline{r},\underline{v},t)$ and $f_i(\underline{r},\underline{v},t)$ therefore satisfy Vlasov equations of the form

$$\frac{\partial f_e}{\partial t} + \underline{v} \cdot \frac{\partial f_e}{\partial \underline{r}} - \frac{e}{m_e}\left(\underline{E}_{ext} + \underline{E}_{int} + \frac{\underline{v}}{c} \times \underline{B}_{ext}\right) \cdot \frac{\partial f_e}{\partial \underline{v}} = 0 \qquad 3.41$$

$$\frac{\partial f_i}{\partial t} + \underline{v} \cdot \frac{\partial f_i}{\partial \underline{r}} + \frac{Ze}{m_i}\left(\underline{E}_{ext} + \underline{E}_{int} + \frac{\underline{v}}{c} \times \underline{B}_{ext}\right) \cdot \frac{\partial f_i}{\partial \underline{v}} = 0 \qquad 3.42$$

where $\underline{E}_{int}$ = internal electrostatic field and $\underline{E}_{ext}$, $\underline{B}_{ext}$ are the sums of the externally applied wave fields.

For sufficiently intense electromagnetic waves $\underline{E}_{ext} >> \underline{E}_{int}$ whereby first order perturbations of the distribution functions from Maxwellian are obtained by taking $\underline{E}_{int} = 0$. This result can be subsequently used to calculate a second order perturbation for $\underline{E}_{int} \neq 0$.

Details of this calculation are given in Appendix I where the spatially and temporally Fourier-transformed second order electron perturbation averaged over velocity space is shown to be approximated by

$$f_{e2}(\underline{k},\omega) \simeq -\frac{\pi^3 \alpha_1^2}{n_e m_e \omega_1 \omega_2}\left\{\delta(\underline{k}-\Delta\underline{k})\delta(\omega-\Delta\omega)+\delta(\underline{k}+\Delta\underline{k})\delta(\omega+\Delta\omega)\right\}$$
$$\cdot\left[\frac{1 + \alpha_1^2 Z\left(\frac{T_e}{T_i}\right) W(x_i)}{1 + \alpha_1^2 W(x_e) + \alpha_1^2 Z\left(\frac{T_e}{T_i}\right) W(x_i)}\right]$$
$$\cdot\left[W(x_e)\left\{|\underline{k}|^2(\underline{E}_1\cdot\underline{E}_2) + 2(\underline{k}_1\cdot\underline{E}_2)(\underline{k}_2\cdot\underline{E}_1)\right\}\right.$$
$$\left. + x_e \frac{\partial W(x_e)}{\partial x_e}(\underline{k}_1\cdot\underline{E}_2)(\underline{k}_2\cdot\underline{E}_1)\right] \qquad 3.43$$

where $\underline{E}$ = wave electric field amplitudes

n_e = mean electron density

$\Delta\underline{k} = \underline{k}_2 - \underline{k}_1$

$\Delta\omega = \omega_2 - \omega_1$

$\alpha_1^{-1} = |\underline{k}|\lambda_{De}$

and the function W has been previously defined (eqn. 3.13). This result applies for $T_e \geq T_i$.

The second order density perturbation is $n_{e2}(\underline{k},\omega) = n_e \cdot f_{e2}(\underline{k},\omega)$. Using

$$n_{e2}(\underline{r},t) = \frac{1}{(2\pi)^4}\int n_{e2}(\underline{k},\omega)e^{i(\underline{k}\cdot\underline{r}-\omega t)}d\underline{k}d\omega \qquad 3.44$$

and eqn. 3.3, the form factor for Thomson scattering from these fluctuations is

$$S(\underline{k},\omega) = \frac{\pi\alpha_1^4}{32n_e m_e^2(\omega_1\omega_2)^2}\left|\frac{1+\alpha_1^2 Z\left(\frac{T_e}{T_i}\right)W(x_i)}{1+\alpha_1^2 W(x_e)+\alpha_1^2 Z\left(\frac{T_e}{T_i}\right)W(x_i)}\right|^2$$

$$\cdot\left|W(x_e)\left\{|\underline{k}|^2(\underline{E}_1\cdot\underline{E}_2) + 2(\underline{k}_1\cdot\underline{E}_2)(\underline{k}_2\cdot\underline{E}_1)\right\}\right.$$

$$\left. + x_e\frac{\partial W(x_e)}{\partial x_e}(\underline{k}_1\cdot\underline{E}_2)(\underline{k}_2\cdot\underline{E}_1)\right|^2\left\{\delta_{\underline{k},\omega}\right\} \qquad 3.45$$

where $\left\{\delta_{\underline{k},\omega}\right\} = \delta(\underline{k}-\Delta\underline{k})\delta(\omega-\Delta\omega) + \delta(\underline{k}+\Delta\underline{k})\delta(\omega+\Delta\omega)$.

Thus enhanced scattering occurs only at frequency shifts $\Delta\omega = \pm(\omega_2-\omega_1)$ and when the scattering wavevector $\underline{k} = \pm(\underline{k}_2-\underline{k}_1)$. The

above result is essentially that of Meyer and Stansfield[14] in the limit of no external magnetic field. The additional terms involving $(\underline{k}_1\cdot\underline{E}_2)(\underline{k}_2\cdot\underline{E}_1)$ account for cases of non-parallel electric fields.

It can be seen that the enhanced scattering cross-section is large for resonances in the plasma dielectric constant $\epsilon = 1 + \alpha_1^2 W(x_e) + Z\alpha_1^2(\frac{T_e}{T_i})W(x_i)$ as is found for thermal plasmas. The case where electron waves are excited ($\alpha_1^2 W(x_e)\to 1$) has been discussed by Kroll, Ron, and Rostoker[15] with experimental Thomson scattering results reported by Stansfield et al[6].

On the other hand, ion waves can also be excited. In this case $x_e \ll x_i \lesssim 1$ thus $W(x_e) \sim 1$ and

$$x_e \frac{\partial W(x_e)}{\partial x_e} \to 0$$

whereby

$$S(\underline{k},\omega) = \frac{\pi}{32 n_e m_e^2 (\omega_1\omega_2)^2}\left|\frac{1+\alpha_1^2 Z\left(\frac{T_e}{T_i}\right)W(x_i)}{1+Z\frac{\alpha_1^2}{1+\alpha_1^2}\left(\frac{T_e}{T_i}\right)W(x_i)}\right|^2\left(\frac{\alpha_1^2}{1+\alpha_1^2}\right)^2$$

$$\cdot\left|\,|\underline{k}|^2(\underline{E}_1\cdot\underline{E}_2) + 2(\underline{k}_1\cdot\underline{E}_2)(\underline{k}_2\cdot\underline{E}_1)\right|^2\left\{\delta_{\underline{k},\omega}\right\} . \qquad 3.46$$

It is of interest to calculate an approximate maximum value of this form factor. For simplicity, $T_e = T_i$ and $Z = 1$ will be taken. In addition the sum of terms involving $\underline{E}_1$, $\underline{E}_2$ can be approximated by $|\underline{k}|^2|\underline{E}_1||\underline{E}_2|$ so that

$$S(\underline{k},\omega) = \frac{\pi E_1^2 E_2^2 k^4}{32 n_e (m_e \omega_1 \omega_2)^2} \left(\frac{\alpha_1^2}{1+\alpha_1^2} \right)^2 \left| \frac{1+\alpha_1^2 W(x_i)}{1+\frac{\alpha_1^2}{1+\alpha_1^2} W(x_i)} \right|^2 \cdot \left\{ \delta_{\underline{k},\omega} \right\} \cdot \qquad 3.47$$

For $\alpha_1 \ll 1$

$$S(\underline{k},\omega) = \frac{\pi E_1^2 E_2^2 k^4 \alpha_1^4}{32 n_e (m_e \omega_1 \omega_2)^2} \left\{ \delta_{\underline{k},\omega} \right\} \qquad 3.48$$

since $|W(x_i)|_{max} < 2$ (see Fig. 3.1).

In the limit of $\alpha_1 \gg 1$, the maximum value of

$$\left| \frac{1+\alpha_1^2 W(x_i)}{1+\frac{\alpha_1^2}{1+\alpha_1^2} W(x_i)} \right|^2 = \frac{\alpha_1^4}{2} \qquad 3.49$$

occurs for $x_i \to 0$ and in this case

$$S(\underline{k},\omega)\Big|_{max} = \frac{1}{2} \cdot \frac{\pi E_1^2 E_2^2 k^4 \alpha_1^4}{32 n_e (m_e \omega_1 \omega_2)^2} \left\{ \delta_{\underline{k},\omega} \right\} \cdot \qquad 3.50$$

Note that the above results for both low and high α_1 are approximately equal and that by definition $\alpha_1 = (k\lambda_{De})^{-1}$, hence

$$S(\underline{k},\omega)\Big|_{max} = \frac{2\pi^3 I_1 I_2}{n_e (m_e c \omega_1 \omega_2)^2 \lambda_{De}^4} \left\{ \delta_{\underline{k},\omega} \right\} \qquad 3.51$$

where $I = (c/8\pi)E^2$ = wave intensity.

Thus for a fixed plasma, the induced ion fluctuations are considerably larger if long wavelength radiation is used over short wavelength radiation. However, frequencies greater than ω_{pe} are still required to allow penetration of the plasma.

In addition it should be remembered that eqn. 3.47 for coupling to ion waves applies only if the condition $x_i \lesssim 1$ has been met by choosing the incident mixing waves such that $\Delta\omega \lesssim |\Delta\underline{k}|v_i$.

Of particular interest is that this process can occur in a plasma produced at the focus of a single high power laser. Although two incident waves are not clearly distinguishable in this case, mixing is still possible since there is a range in frequencies defined by the finite laser linewidth and a range in $\underline{k}$ defined by the focal cone of incident radiation. Use of a long wavelength laser would not only induce large amplitude ion waves but would do so over a large fraction of the input focal cone whereby essentially all of the laser power would be available for coupling purposes. Measurements of enhanced Thomson scattering from such induced waves in a TEA CO_2 laser-produced plasma are reported later in this chapter.

3.3 Thomson Scattering From a Low Density Plasma

3.3.1 Setup

The experimental setup used for scattering from a low density plasma is shown in Fig. 3.4. The hollow cathode discharge used was identical to that of Gerry[16]. An arc is struck between a tantalum cathode and copper anode in approximately 10^{-3} Torr of argon and is

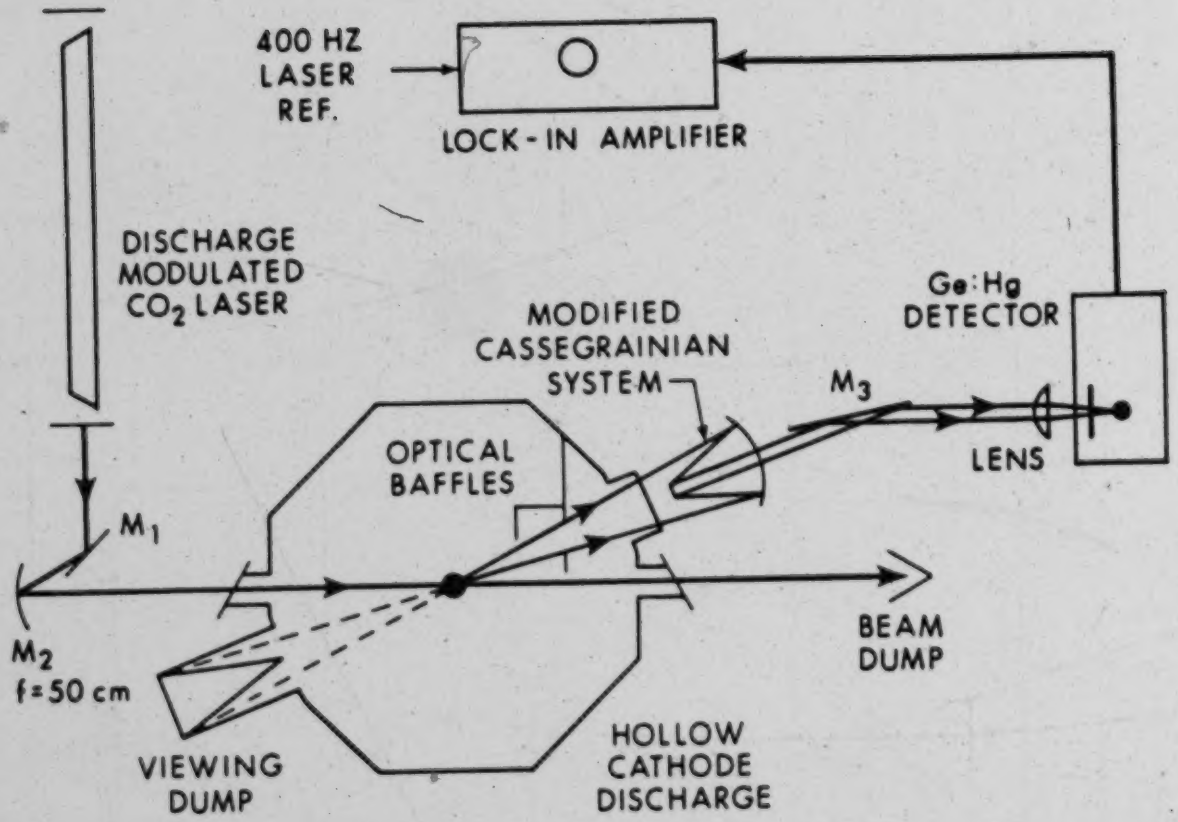

Fig. 3.4 Experimental setup for Thomson scattering from a low density plasma.

confined to a 0.5 cm diameter column by an axial $\underline{B}$ field of $\sim$ 500 gauss. Power requirements of 40A at 40V are supplied from a D.C. welding supply while initiation of the arc is accomplished by applying several kilovolts of R.F. between the electrodes. Typical axial parameters at these operating conditions are $n_e \sim 5 \times 10^{13}$ cm^{-3}, $T_e = 5$ eV and $T_i \sim 0.5$ eV.

A low-pressure discharge-modulated CO_2 laser[17] with output power variable from 50 - 400 watts rms at 400 Hz was focused into the plasma with a 50 cm gold-coated mirror. After passage through the plasma, the beam was dumped into a blackened wedge-shaped absorber.

Use of polarized radiation was doubly advantageous. With Brewster windows on the plasma chamber, large stray light levels arising from window reflections could be minimized. Secondly, this allowed the electric field to be oriented perpendicular to the wavevector of the scattered radiation collected, enabling a maximum Thomson cross-section to be obtained since $\beta = \pi/2$ (see eqn. 3.1). A polarized output from the laser was obtained by employing Brewster windows on the laser discharge tube.

As a reasonable compromise between a distinct electron feature and required spectral resolution, a scattering parameter $\alpha = 2$ was chosen. Thus for typical parameters of this plasma, a forward scattering angle of 22° was used.

Although a large collection solid angle $\Delta\Omega$ is desirable for increasing the scattered power detected, care must be taken to assure that the variation in $\underline{k} = \underline{k}_s - \underline{k}_i$ is small over $\Delta\Omega$ in order to minimize smearing of spectral details. In this experiment a collection solid angle of $\pi \times 10^{-2}$ sr was used for the scattering angle of 22°.

Scattered light was collected over this solid angle by a Cassegrainian mirror system modified to provide a well-collimated output beam. Such good collimation was necessary since a scanning Fabry-Perot interferometer was to be used for spectral analysis. A blackened conical viewing dump was placed opposite the Cassegrainian in order to minimize detected stray light from inside the chamber.

A 6.5 cm focal length NaCl lens was used to focus the output beam from the Cassegrainian onto a mercury-doped germanium detector cooled with liquid helium. This gave an overall magnification of 0.5 in the collection system which for the detector size of 1 x 2 mm^2 enabled scattering to be observed from the total intersection volume of laser and plasma.

A narrowband 10.6μ filter (B.P. = 1600Å) also cooled to 4.2°K and mounted directly in front of the detector gave an improved responsivity of 4×10^7 volts/watt (a factor of 80 over no filter) with no increase in noise level. Even with this improvement in signal-to-noise, expected scattered signal levels were still well below that of broadband detector noise (6 $\mu V/\sqrt{Hz}$). Synchronous detection employing a PAR model HR-8 lock-in amplifier was therefore necessary for improved signal-to-noise. Integration time constants of 10 - 100 sec were used in the measurements. Phase reference for the lock-in was obtained from a laser current monitor.

Finally, a blackbody radiator was placed at the scattering center and the overall collection optical system transmission factor was measured to be 0.14.

3.3.2 Results and Discussion

Preliminary measurements of integrated Thomson scattering were done with no spectral dispersion in the collection optical system.

In this case, the scattered power is described by eqns. 3.2 and 3.19. Separate Langmuir probe measurements yielded $\langle n_e \ell \rangle = 1.5 \times 10^{13}$ cm^{-2} and $T_e = 4.7$ eV. The ion temperature was taken to be 0.5 eV. Thus for a 50W incident laser beam, a total scattered power of 4.9×10^{-13} watts would be expected, or including the optical transmission and detector responsivity, a scattered signal level of 2.7 μV.

Stray light was reduced to a minimum obtainable level of 15 μV for 50W of incident laser power. Irising near the laser was done to limit the beam size and highly divergent modes. Optical baffling preventing the Cassegrainian from directly viewing the entrance and exit apertures of the plasma chamber gave significant improvement by a factor of 30. In addition, completely enclosing the detection system eliminated background sources outside the chamber.

Such large stray light levels are not normally a problem since they can be subtracted from the scattering measurements. In this experiment however, background level variations of 18% occurred on minute time scales. Transverse mode changes in the laser were mainly responsible with 5% variation being caused by output power and phase fluctuations. For long integration times, no improvement was obtained since very slow drifts were still present.

Statistically averaged measurements over ten plasma on-off cycles implied a scattered signal of 1.5 μV. Agreement with the expected

2.7 μV to within a factor of two is quite good under these circumstances.

Signal levels given above correspond to an input laser power of 50W rms. Measurements at powers up to 400W yielded a linear behavior of both stray light and Thomson scattered signals. Effective noise for integration time constants greater than 20 sec was less than 1 μV, thus in this case, no advantage to using powers above 100W was obtained.

Because the background was large and drifting, and the electrical noise level only marginally below that of Thomson scattering, no spectral analysis was attempted since the scattered power per spectral band would be considerably less than the integrated scattering. It is clear that successful spectral analysis would require a stable high power laser and long integration times in order to improve both signal-to-noise and signal-to-background.

3.4 High α, Collision-Dominated Thomson Scattering Measurements

3.4.1 Setup

A schematic of the backscattering experiment from an argon plasma jet is shown in Fig. 3.5. Parameters of this jet are known from the absorption and interferometry measurements of Chapter II. In this experiment the jet was operated at 300A and an argon flow rate of 100 cc/sec.

The CO_2 laser, input optical system and beam dumping were identical to those used in conjunction with the hollow cathode discharge discussed in the previous section. Here the scattering volume was situated 8 mm above the jet anode.

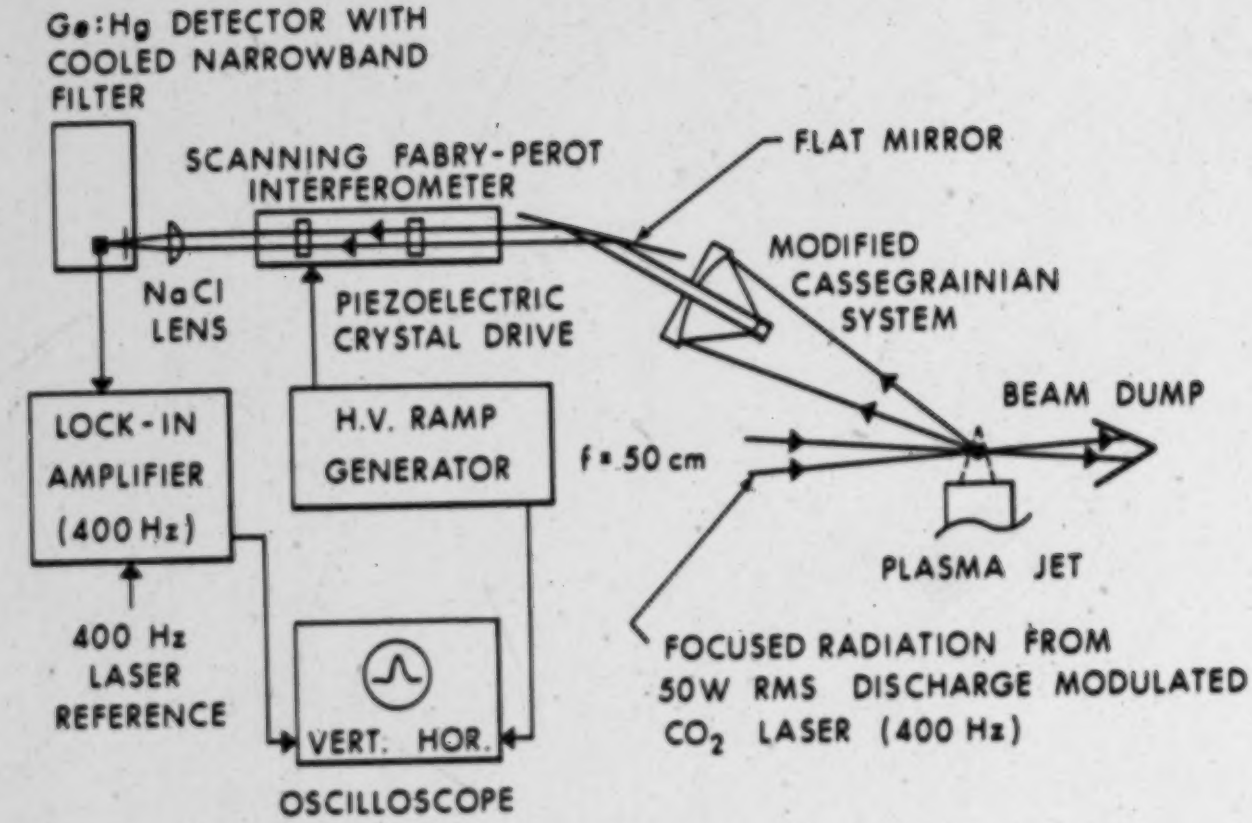

Fig. 3.5 Experimental setup for Thomson scattering from a collision-dominated plasma.

For typical plasma jet electron densities and temperatures, the scattering parameter α for 10.6μ radiation is greater than 36 for any scattering angle θ thus establishing a highly cooperative Thomson scattering regime. In this case the width of the scattered spectrum is inversely proportional to α. Thus to minimize the spectral resolution required, a value of $\alpha = 37$ corresponding to a scattering angle of 160° was chosen.

Thomson scattered light was collected by a modified Cassegrainian system. A He-Ne laser illuminating a small metal ball centered in the scattering volume was used to align the two Cassegrainian mirrors to achieve the best collimated output beam. The theoretical minimum full-angle divergence of 7 mrad for this system was obtained. This assured excitation of only the axial cavity mode in a scanning Fabry-Perot interferometer placed immediately behind the Cassegrainian.

This Fabry-Perot consisted of two germanium substrate mirrors both with dielectric coatings for a reflectance of 94% on one surface and 0% on the other. Its general characteristics and performance are described in Appendix II. A nominal plate spacing of 10 cm was used to obtain a free spectral range of 5.6 Å which was marginally greater than the 4.5 Å FWHM scattered spectrum that would be expected on the basis of a collisionless plasma. Small variations (up to 16μ) in this spacing were effected by a piezoelectric crystal that was mounted behind one of the mirrors and driven by a high-voltage ramp generator (0 - 1.6 KV).

A 6.5 cm focal length NaCl lens focused the output beam from the Fabry-Perot onto a mercury-doped germanium detector through a cooled narrowband filter as described in the previous low density measurements. Synchronous detection was again utilized for signal

averaging and noise reduction.

An oscilloscope provided for visual display of the scattered spectrum. Since Fabry-Perot resonant wavelength shifts are directly proportional to spacing (for constant mode number), a ramp generator monitor was applied to the scope X-axis to obtain a linear wavelength dispersion. Output from the lock-in amplifier was used for amplitude deflection.

Measurement of spectrally integrated scattering was done with the Fabry-Perot interferometer removed from the optical system. In this case a blackbody radiator placed at the scattering center yielded a transmission of 0.18. For these measurements an incident laser power of 50W rms was used. Higher powers were not required since observed signal levels were well above detector noise and stray light levels.

3.4.2 Results and Discussion

Measurements done here were for an average electron density of 1.2×10^{17} cm^{-3} in a viewed scattering volume of $1 \times 2 \times 3$ mm^3. The electron and ion temperatures were taken as 1.2 and 1 eV respectively. For these parameters, $\alpha = 37$ resulting in a distinct central ion feature in the scattered spectrum which would have a FWHM of 4.5Å if collisions were negligible. However collisional effects are important here with the collisional parameter of the ions $p_i \sim 8$. Thus a considerably narrower lineshape with a FWHM of ~ 0.65Å, as described by eqn. 3.37, was expected.

Since collisions only modify the spectral shape, the integrated scattering is still predicted by eqns. 3.2 and 3.19. In this experiment $\langle n_e \ell \rangle = 3.6 \times 10^{16}$ cm^{-2}, which inferred a total scattered power of 2.25×10^{-9} watts for an incident laser power of 50W rms. Including the optical transmission factor and detector responsivity, this corresponds to a scattered signal level of 17 mV. Experimentally, a value of 26 mV was measured with the Fabry-Perot interferometer removed and is in reasonable agreement with the expected result.

Subsequent spectral measurements were done using the Fabry-Perot interferometer. For the etalon spacing of 10 cm, corresponding to a free spectral range of 5.6Å, a finesse of 6 was obtained as shown in Fig. 3.6. Alignment was done using a low pressure CO_2 laser (linewidth $\sim$ 0.1Å) hence Fig. 3.6 represents the instrumental linewidth. This resolution of 1Å, though not as good as desired, nevertheless allowed an unambiguous check for line narrowing and disappearance of the ion peak. Furthermore for a narrow line, observation of the fractional broadening over the instrumental width would set an upper bound on the scattered linewidth.

Background scattering and noise as shown in Fig. 3.7a was well below plasma scattering which is shown in Fig. 3.7b. A scattered linewidth of about 0.5Å was obtained from empirical folding with the instrumental linewidth.

It is clear that pronounced narrowing of the ion feature and the disappearance of the ion acoustic resonances indeed occurs as expected for a highly collisional plasma. These results however are at odds with recent theory by Leonard and Osborn [18] which predicts

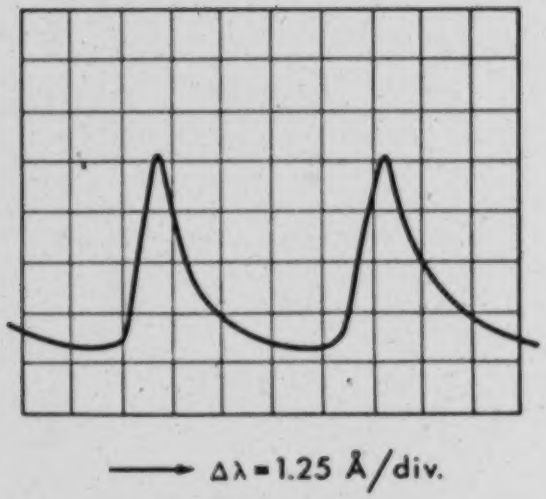

Fig. 3.6 Fabry-Perot resolution characteristics for a plate spacing of 10 cm.

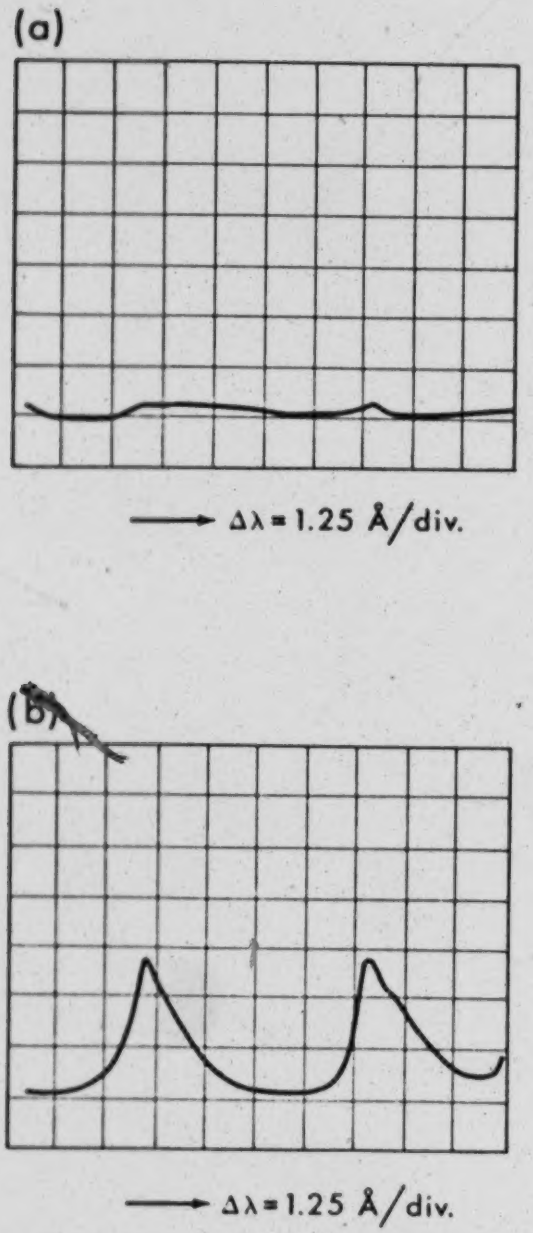

Fig. 3.7 Fabry-Perot interferograms: (a) noise and background scattering (jet off), (b) Thomson scattering. Vertical deflection factors are the same in both cases.

only marginal narrowing and enhanced ion acoustic resonances. This discrepancy may well be due to their assumption of a fully ionized plasma. Other recent calculations[19] imply spectral narrowing and reduced ion resonances in partially ionized plasmas, such as the plasma jet used here, although no specific results have been presented for Thomson scattering of 10.6μ radiation.

Further collision-dominated Thomson scattering experiments are therefore required to test these various theories. Such measurements would require a substantially higher resolution than was attainable here. During this writing, new Fabry-Perot etalons with higher reflectivity have arrived and proved capable of resolving down to the laser linewidth itself (0.1Å).

3.5 High α, Enhanced Thomson Scattering

3.5.1 Setup

Measurements of scattering from non-thermal fluctuations were done using the arrangement of Fig. 3.8. A confocal 10 cm lens and concave mirror, used as a total reflector on a UV initiated Rogowski-type CO_2 laser[20,21], was enclosed in a low pressure (15 Torr) hydrogen cell. Breakdown occurred at the focus when the laser was fired.

Scattering measurements at 10.6μ were performed in a plane perpendicular to the cavity axis using a separate helical pin TEA CO_2 laser focused into the plasma via a 10 cm focal length NaCl lens.

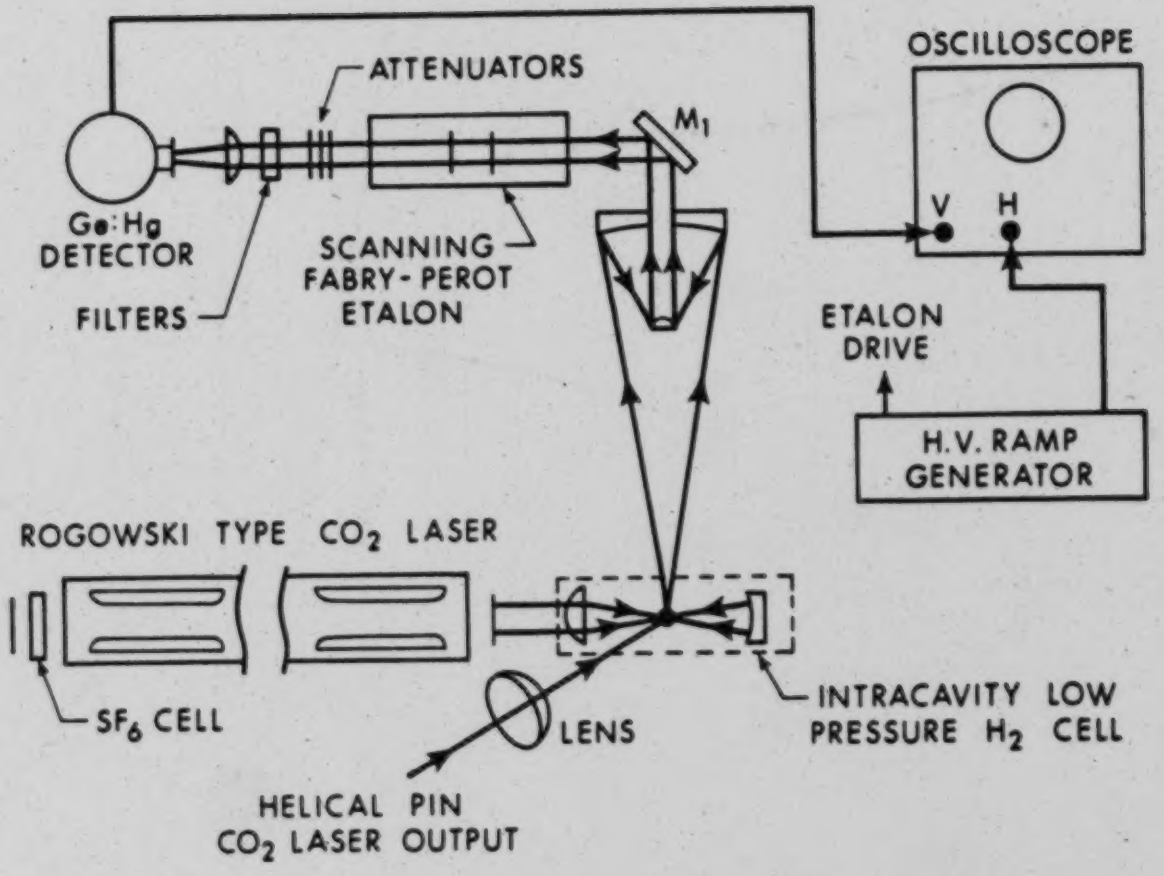

Fig. 3.8 Experimental setup for enhanced Thomson scattering measurements.

Both the probe and plasma-producing lasers were unpolarized.

Thomson scattered radiation at 90° was collected by a modified Cassegrainian system and detected by a mercury-doped germanium detector as previously described. Loading of the detector to 560Ω gave a detection time constant of less than 100 ns. In these measurements the cooled narrowband 10.6μ filter was not used. Even with the resulting lower responsivity, large signals were observed and mylar attenuators in the collection system were necessary in order to maintain a linear detector response. Output from the detector was monitored on an oscilloscope.

To establish that the observed signal was neither refraction nor reflection of the probe beam, a scanning Fabry-Perot interferometer was used to check for a Doppler shift in the detected radiation.

Large amounts of stray light and Thomson scattering from the plasma-producing Rogowski laser which normally also operated at 10.6μ, was eliminated by utilizing an intracavity SF_6 cell to tailor its gain profile. For 100 Torr of SF_6 in the 5 cm long cell, lasing occurred only at 9.6μ. With both > 10μ long wavelength pass and 10.6μ bandpass filters in the collection optical path, rejection of this radiation was > 10^6. Thus scattering of the 10.6μ probe laser could be easily detected by discriminating against the 9.6μ laser producing the plasma. In addition, the 10.6μ filter limited the plasma emission seen by the detector to values less than that of Thomson scattered radiation.

3.5.2 Results and Discussion

Scattering measurements were done for a probe laser power of 1.5 MW and a plasma-producing laser power of 300 MW. Results reported

here were for an initial cell pressure of 15 Torr hydrogen.

Typical parameters in the scattering volume (1 x 1 x 2 mm^3) were $n_e \sim 4 \times 10^{17}$ cm^{-3}, $T_e \sim 10$ eV and $T_i \sim 5$ eV. Thus the scattering parameter $\alpha = 33$ and collisional parameter $p_i \sim 0.5$, whereby a dominant central ion feature with a FWHM = 55Å not substantially modified by collisions would be expected on the basis of thermal fluctuations. In addition, for 1.5 MW of unpolarized incident radiation, interaction length of 2 mm and collection solid angle of $\pi \times 10^{-2}$ sr, a total scattered power of 7.5×10^{-5}W would also be expected.

With the Fabry-Perot etalon removed, a spectrally integrated signal level of 0.22V was measured. For mylar attenuation = 216, overall transmission = 0.1 and reduced detector responsivity (including loading), this corresponded to a scattered power of 85 mW. Thus the observed signal was larger than that predicted on the basis of thermal fluctuations by a factor of about 1100.

On the other hand, such a large signal could be due to reflection or refraction rather than Thomson scattering. During the production of this transient plasma, a radial shock wave with peak density $\sim 10^{18}$ cm^{-3} expands at a velocity of $\sim 5 \times 10^6$ cm/sec[21]. In this case the laser frequency is only a factor of three above the plasma frequency and, along with the density gradient, might have accounted for the observed fractional scattering of 10^{-7}. Such sources, however, would be Doppler shifted by about 15Å.

To check for such a shift, a Fabry-Perot interferometer with free spectral range of 40Å and resolution of 6Å was employed. It was found that the plasma-scattered spectrum was not shifted from that obtained by suspending a small metal ball at the scattering center. Thus reflection/refraction can be ruled out as the source of observed

signal.

In addition, the instrumental width was broadened by only 20%; thus the enhanced Thomson scattered radiation was substantially narrowed over the FWHM of 55Å predicted for a thermal plasma. Therefore the observed scattering is attributable to non-thermal fluctuations.

As discussed in section 3.2.3, induced fluctuations in this experiment can arise from mixing of an infinite number of waves defined by the focal cone and laser linewidth. Thus, according to eqn. 3.46, enhanced scattering would be seen only if the scattering $\underline{k}$ were matched to any $\underline{k}_2-\underline{k}_1$ where $\underline{k}_{1,2}$ lie within the plasma-producing focal cone of radiation. In this experiment such matching was not used, therefore eqn. 3.46 does not directly predict the observed enhancement. However, non-thermal fluctuations diffuse in $\underline{k}$-space, whereby the measured enhancement of 1100 is a lower bound to the level of enhancement that would be found for matched conditions.

That the 9.4μ Rogowski laser efficiently induced fluctuations over a wide spectrum can be seen from the coupling condition $\Delta\omega \lesssim |\Delta\underline{k}|v_i$. For these measurements, the cone of focused radiation had an apex angle of 22° (3.8 cm aperture and 10 cm focal length). Thus the mean angle of 11° would imply strong coupling for $\Delta\omega \lesssim 4\times10^9$ sec^{-1} which is of the order of the laser linewidth ($\Delta\omega_L \sim 10^{10}$ sec^{-1}).

An approximate quantitative expression for the enhancement in spectrally integrated scattering can be obtained from the total coherent longitudinal wave energy density in the plasma, which is given by

$$u = \frac{n_e e^2}{(2\pi)^3}\int \frac{1}{k^2} \lim_{VT\to\infty}\left\{\frac{1}{VT}\frac{|n_e(\underline{k},\omega)|^2}{n_e}\right\} d\underline{k}d\omega$$

$$= \frac{n_e e^2}{(2\pi)^2}\int \frac{S(\underline{k},\omega)}{k^2}\, d\underline{k}d\omega \qquad 3.52$$

where the form factor for Thomson scattering has been substituted for the electron density autocorrelation. Values of $|\underline{k}|$ are limited to $0 \leq |\underline{k}| \leq \lambda_{De}^{-1}$ since shorter wavelength cooperative fluctuations are heavily Landau damped.

In the absence of induced waves thermal fluctuations prevail, whereby using eqn. 3.19 and taking $Z = 1$ and $T_e = T_i$ for simplicity,

$$u_{thermal} \sim \frac{0.6}{\pi}\frac{n_e e^2}{\lambda_{De}} . \qquad 3.53$$

Assuming the non-thermal energy to be the same before and after diffusion in $\underline{k}$ and therefore using eqn. 3.50,

$$u_{nonthermal} \sim \frac{\pi e^2 I_o^2}{2m_e^2 c^2 (\omega_o \lambda_{De})^4 |\Delta\underline{k}|^2} \qquad 3.54$$

where I_o = laser intensity and $\omega_1 \sim \omega_2 \sim \omega_o$.

Thus a relative measure of the enhancement as given by the ratio of total non-thermal to thermal wave energy is

$$\frac{u_{nonthermal}}{u_{thermal}} \sim \frac{\pi^2 I_o^2}{1.2 n_e m_e^2 c^2 \omega_o^4 \lambda_{De}^3 |\Delta\underline{k}|^2} \qquad 3.55$$

Experimentally $I_o \sim 2 \times 10^{17}$ erg/sec-cm^2 at $\lambda = 9.6\mu$, $\lambda_{De} = 3.7 \times 10^{-6}$ cm and a typical $|\Delta \underline{k}| \sim 1250$ cm^{-1} corresponds to the mean focal cone angle of 11°. For these values $u_{nonthermal}/u_{thermal} \sim 9400$. Although only a rough approximation this result does indicate that the enhancement of $\sim$ 1100 found experimentally is not unreasonable.

Subsequent experiments to measure the $\underline{k}$-spectrum of these fluctuations would be useful in the study of laser light absorption by non-linear processes in plasmas of thermonuclear interest. From the results reported here, it is clear that Thomson scattering of 10.6μ radiation would serve this purpose adequately.

CHAPTER IV

PLASMA PERTURBATION BY ABSORPTION OF 10.6μ RADIATION

4.1 Introduction

Inverse bremsstrahlung absorption ($\sim n_e^2 \lambda^2$) of 10.6μ radiation in plasmas is substantially greater than at visible wavelengths, which results in correspondingly larger perturbations of density and temperature. This is of particular importance in cases where a high power pulsed TEA CO_2 laser is required for plasma diagnostics such as Thomson scattering.

When the plasma being investigated is only partially ionized, small amounts of heating can significantly change the electron density ($n_e \sim T_e^8$) which in turn leads to substantially increased absorption.

Two experiments measuring the perturbation of a partially ionized argon plasma jet by a focused TEA CO_2 laser are described. First, the amplitude of the shock wave generated was recorded using a high speed piezoelectric pressure transducer. In the second, enhanced bremsstrahlung radiation was used to monitor plasma heating.

The purpose of these measurements was to determine practical limits of laser power beyond which large perturbations were induced. An approximate quantitative description of the dominant perturbing mechanism is also given.

4.2 Measurement of Shock Energy Released

4.2.1 Setup

The experimental arrangement is shown in Fig. 4.1. Radiation from a helical pin TEA CO_2 laser[1] with nominal output energy of 0.2 joule was varied by using calibrated attenuators constructed of thin mylar sheets (.002", .006"). This attenuated beam was focused into an atmospheric pressure argon plasma jet[2] by a 10cm focal length NaCl lens.

The resulting interaction volume of laser and plasma had a cross-sectional area of $\sim 1mm^2$ and a length of $\sim$ 3mm through the plasma.

A long Langmuir probe was swept through the plasma (Chapter II)in order to monitor the average electron density which was varied over 10^{15} - 10^{17} cm^{-3} by axially translating the jet.

Measurement of plasma perturbation was done using a high speed piezoelectric pressure transducer to record the amplitude of the shock wave generated by absorbed CO_2 laser radiation. This particular piezoprobe (Atlantic Research LD-25) had an adequate time resolution of $\sim$ 1 μsec. It was mounted on a movable stand to permit easy positioning at varying distances d from the focal volume; results given here correspond to d = 2 and 7 cm. A check of the transducer response (2V/atm.) was done using a shock tube to provide a known pressure jump.

Finally a capacitive spark discharge in air was used for calibration of piezosignal vs energy released at a point. Good agreement with theoretical blast wave relations[3] was obtained. Energies in the range 100 - 500 mJ were used.

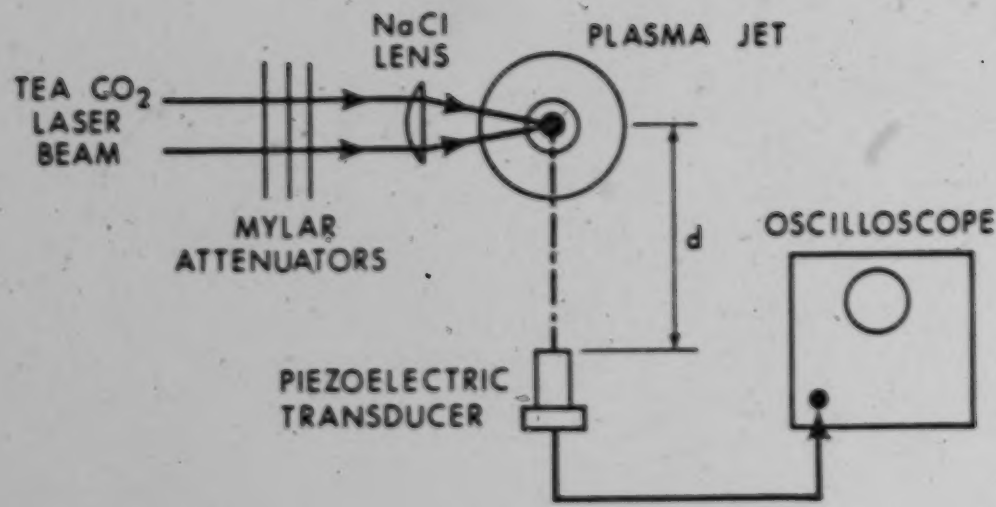

Fig. 4.1 Experimental setup for jet perturbation measurements using a piezoprobe.

4.2.2 Results and Discussion

Two separate sets of measurements were done. In the first the piezoprobe signal was monitored as a function of laser input energy for a constant initial electron density of 3×10^{16} cm^{-3}. Fig. 4.2 shows energy release E_o from the focal region vs incident laser energy E_i. Two additional curves assuming complete transfer of absorbed energy to shock energy are also given. The first corresponds to total absorption of incident laser light while the second assumes only small perturbations whereby the absorbed energy is determined by the initial electron density and temperature.

It is clear that for $E_i \gtrsim 20$mJ plasma disturbances are large. On the other hand, the minimum detectable shock energy of $\sim 10^{-8}$J was much less than the 2×10^{-5}J of electron thermal energy in the focal region and hence can be considered a small perturbation.

Thus a threshold laser energy of $\sim$ 10mJ exists in this case. Due to the highly non-linear behavior, it is unlikely that this limit could be exceeded by more than a factor of 3 for useful diagnostic measurements under similar plasma conditions.

An approximate quantitative description of the heating process can be obtained from the energy density in a partially ionized plasma:

$$u = \frac{3}{2} n_e T_e + \frac{3}{2} n_i T_i + \frac{3}{2} n_n T_n + n_e I \quad \text{eV/cm}^3 \qquad 4.1$$

for $n = \text{cm}^{-3}$, $T = \text{eV}$, I = ionization energy (eV) and e,i,n = electrons, ions, neutrals respectively.

For a simple analysis, expansion of the focal volume will be

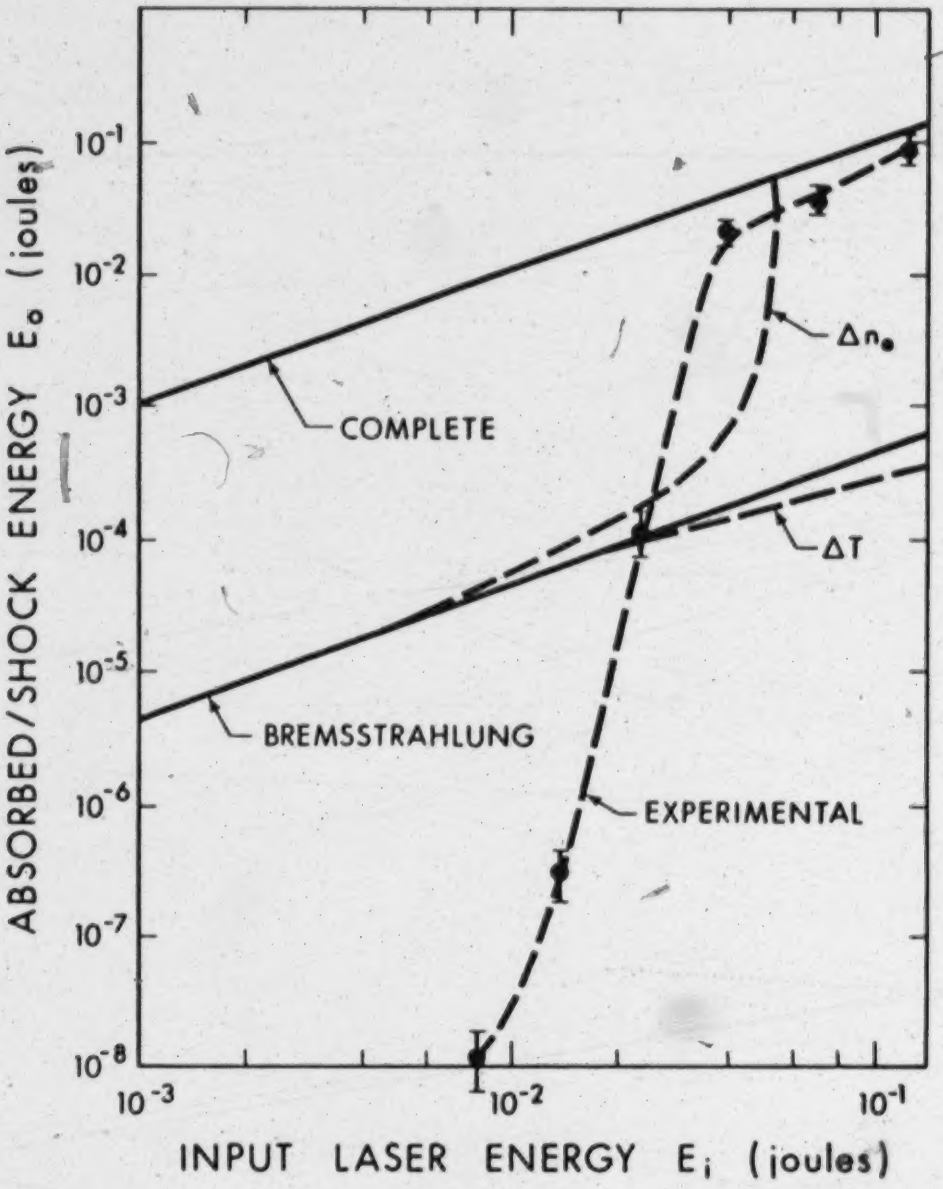

Fig. 4.2 Shock energy released vs incident laser energy for a constant initial electron density of 3×10^{16} cm^{-3}.

neglected along with energy losses through heat conduction and radiation. Thus for this fixed volume, $n_i + n_n = n_o$ = constant. In addition it is reasonable to take $T_i \sim T_n$ since the ion-neutral equipartition time is $\sim$ 20ns for conditions in the jet.

Equating absorbed power (using α of eqn. 2.18) to du/dt,

$$1.8\times10^{-35}\,\frac{P_i(t)}{A}\,\frac{n_e^2}{T_e^{3/2}} = \frac{3}{2}\,n_e\,\frac{dT_e}{dt} + \frac{3}{2}\,n_o\,\frac{dT_i}{dt} + (\frac{3}{2}\,T_e + I)\frac{dn_e}{dt} \qquad 4.2$$

where A = cross-sectional area of the focus, P_i = incident power and the units are eV and cm. The radiation intensity was taken to be constant across the focal area A.

Several limiting cases can be easily calculated. If all of the absorbed energy goes into heating only electrons (no ion-neutral heating or increased ionization), the final electron temperature, upon integration of eqn. 4.2, would be

$$T_{e_2} = \left[1 + \frac{1.88\times10^{-16}\,n_e E_i}{A T_{e_1}^{5/2}}\right]^{2/5} T_{e_1} \qquad 4.3$$

for T_e = eV, n_e = cm^{-3}, E_i = J, A = cm^2. The shock wave energy is then given by

$$E_o = 2.4\times10^{-19}\,n_e T_{e_1} A z \left[\left(1 + \frac{1.88\times10^{-16}\,n_e E_i}{A T_{e_1}^{5/2}}\right)^{2/5} - 1\right] \qquad 4.4$$

where ℓ = interaction length = 0.3cm, $n_e = cm^{-3}$, E = J and T_e = eV. This is an upper limit since all of the absorbed energy is assumed to be converted into shock energy.

If ions and neutrals are heated at the same rate as electrons,

$$T_{e_2} = \left[1 + \frac{1.88\times10^{-16} n_e^2 E_i}{A T_{e_1}^{5/2}(n_e+n_o)}\right]^{2/5} T_{e_1} \qquad 4.5$$

$$E_o = 2.4\times10^{-19}(n_e+n_o)T_{e_1} A\ell\left[\left(1 + \frac{1.88\times10^{-16} n_e^2 E_i}{A T_{e_1}^{5/2}(n_e+n_o)}\right)^{2/5} - 1\right] \qquad 4.6$$

These two cases correspond to zero and infinite electron-ion equipartition times τ_{ei}. For typical jet densities and temperatures, τ_{ei} = 40-100 ns[4] which is much smaller than the laser pulse length of 3 μs. Thus eqns. 4.5 and 4.6 would be expected to give the best results if only the temperature increased.

On the other hand, if all of the absorbed energy goes into increased ionization ($\frac{dT}{dt} \approx 0$), the final electron density is given by

$$n_{e_2} = \frac{n_{e_1}}{1 - \frac{1.12\times10^{-16} n_{e_1} E_i}{A T_e^{3/2}(\frac{3}{2}T_e + I)}} \qquad 4.7$$

for E_i = J, A = cm^2, T = eV, I = eV, n = cm^{-3} which gives a shock energy

$$E_o = \frac{1.8\times10^{-35}\,\dfrac{n_{e_1}^2 E_i \ell}{T_e^{3/2}}}{1 - \dfrac{1.12\times10^{-16} n_{e_1} E_i}{A T_e^{3/2}(\frac{3}{2}T_e + I)}} \quad . \quad . \quad 4.8$$

Unlike the previous ΔT cases, a catastrophic process occurs for

$$E_i \geq \frac{A T_e^{3/2}(\frac{3}{2}T_e + I)}{1.12\times10^{-16} n_{e_1}} \quad . \quad 4.9$$

Equations 4.6 and 4.8 are plotted in Fig. 4.2 for $n_e = 3\times10^{16}$ cm^{-3}, $T_e = 1eV$, $A = 10^{-2}$ cm^2, $\ell = 3mm$ and $I = 15.7$ eV (argon). Clearly the Δn_e limit is much more dominant than the ΔT limit. It is evident that the rapid onset of large perturbations forcast by eqn. 4.8 is in reasonable agreement with the experimental threshold of about $\frac{1}{3}$ this quantity.

That the energy output at low laser inputs is much less than that corresponding to complete conversion of bremsstrahlung to shock energy merits some qualitative discussion. Since most of the absorbed energy is taken up in further ionization, pressure wave generation will be governed by recombination where, from Chapter II, recombination times range from 10 μs at $n_e = 10^{18}$ cm^{-3} to 1 ms at $n_e = 10^{16}$ cm^{-3}.

Absolute calibration of the piezoprobe used to obtain the shock energies applies only to a fast release of energy. Experimentally, an air spark ($n_e \geq 10^{18}$ cm^{-3}) with fast recombination was used while the theoretical relations of Brode[3] assume an instantaneous energy deposit at a point. Obviously for longer-lived energy releases, lower amplitude pressure jumps will be measured by the piezoprobe.

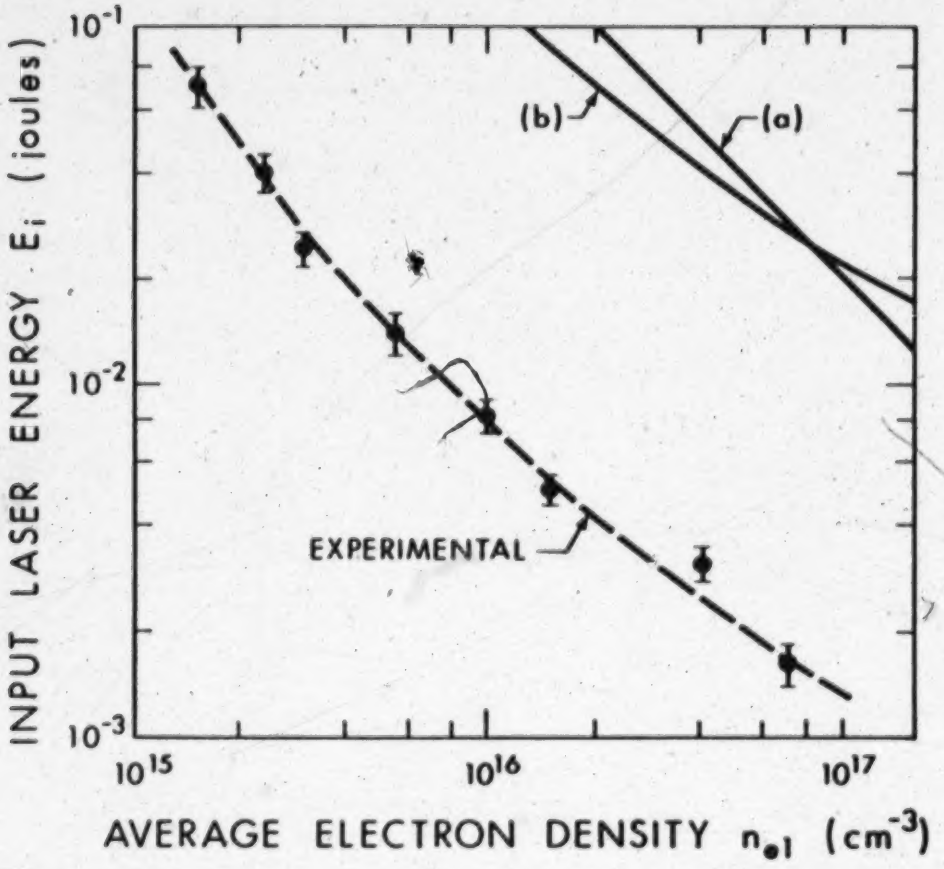

Fig. 4.3 Incident laser energy vs average electron density for a constant shock energy of 10^{-8}J.

Thus at low level laser inputs, where the transiently enhanced electron density is still small, measured shock energies are expected to be less than the actual values. However, this should not substantially alter the large-disturbance threshold because of the highly non-linear behavior of Fig. 4.2.

In the second set of measurements, input laser energies required to produce a fixed low-level perturbation were monitored as a function of initial electron density in the jet. A constant shock energy of 10^{-8}J corresponding to the minimum detectable piezosignal was used. The electron density was varied by focusing the TEA laser at different heights above the jet anode.

Results of these measurements are shown in Fig. 4.3. Also plotted are two curves of the breakdown energy defined by eqn. 4.9. A constant electron temperature of 1.2 eV was used in (a) while in (b) temperature corrections derived from Saha equilibrium of the inital conditions have been included.

Thus over a wide range of electron densities, it can be seen that a relatively low-level perturbation is assured by taking input laser energies below about 0.1 of that predicted by the breakdown energy.

4.3 Measurement of Enhanced Emission

4.3.1 Setup

A schematic of the experiment is shown in Fig. 4.4. Output radiation from a helical pin TEA CO_2 laser was varied by using mylar

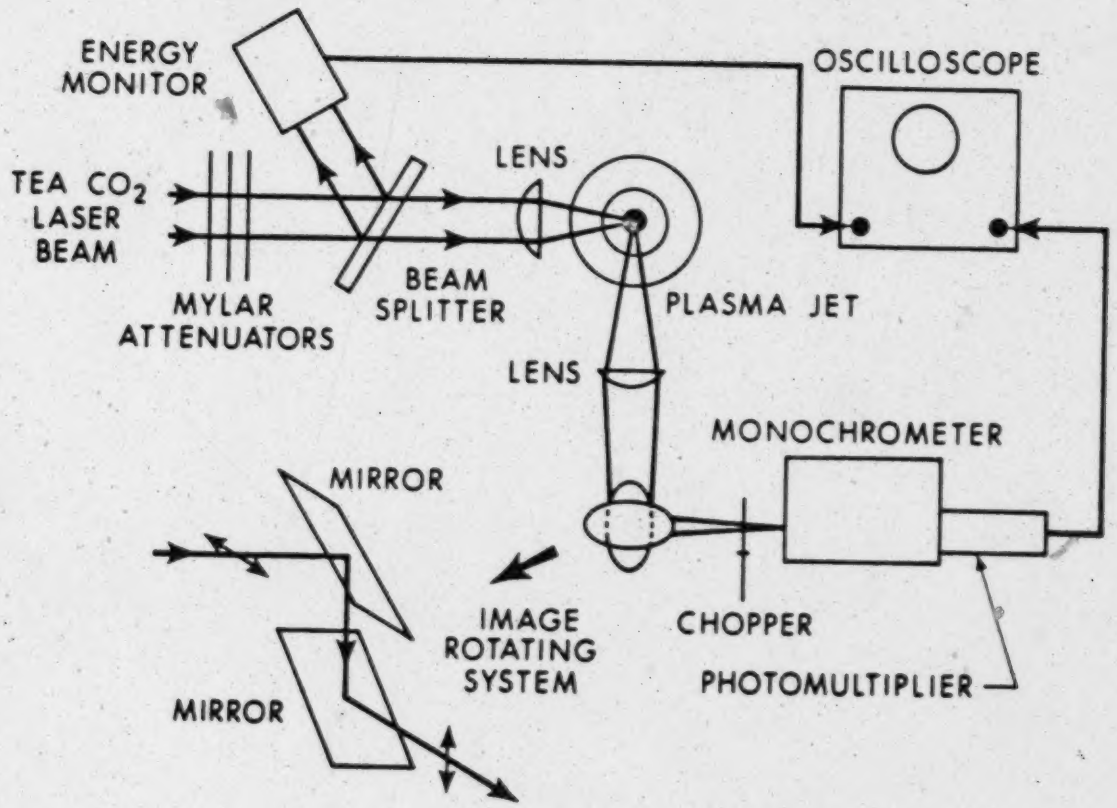

Fig. 4.4 Experimental setup for enhanced plasma emission measurements.

attenuators. A portion of the attenuated light was obtained from an uncoated NaCl beam splitter (two-surface reflectivity = 8%) and monitored using a Gen-Tec pyroelectric energy detector. The transmitted beam was focused into an argon plasma jet as done in the previous shock measurements with resulting interaction volume of $\sim 1mm^2 x 3mm$.

Plasma emission at visible wavelengths was collected from this volume and imaged at the input of a 0.25m Jarrel-Ash monochromator by a lens. A system of two flat mirrors provided image rotation whereby the 3mm length of perturbed plasma could be imaged parallel to the entrance slit.

Slit sizes of 1000μ were used in the measurements to obtain relatively large signal levels and a spectral integration of continuum radiation over approximately 25Å. With these large slits, improved spatial resolution was achieved by positioning the collecting lens and monochromator to give a two-fold magnification of the interaction volume.

A photomultiplier at the monochromator output was used for light detection. Loading to 51KΩ was found to be a reasonable compromise between a maximum in signal level and a minimum in response time. In this case the detection time constant was 30 μsec.

Both plasma emission and input laser energy were simultaneously recorded on an oscilloscope. Quiesent emission was monitored by inserting a chopper wheel into the collection optical system.

4.3.2 Results and Discussion

Measurements of transiently enhanced emission, centered at $\lambda = 6909Å$, as a function of input laser energy were done at constant

initial electron densities of 3×10^{16} and 8×10^{16} cm^{-3}.

These results are plotted in Fig. 4.5 b,d where enhancements have been normalized to the non-perturbed emission. Random fluctuations of about 6% in the quiesent emission precluded measurement of lower level perturbations. The values actually measured have been multiplied by a calculated correction factor of 1.5 since the reference levels included emission from outside of the interaction region (see Fig. 4.6).

It can be seen that the large disturbance threshold for $n_e = 3\times10^{16}$ cm^{-3} (curve b) and marked non-linear behavior are in good agreement with the previous shock results. For low input laser energies, a larger relative perturbation for $n_e = 8\times10^{16}$ cm^{-3} was found as expected.

The Δn_e model (eqn. 4.7) can be used to approximately calculate enhanced emission from the interaction volume V shown in Fig. 4.6. A constant electron temperature will be taken, since spatially T_e varies by only $\sim$ 30% in V and temporally $\Delta T = 0$ (Δn_e limit).

In this case, plasma emission per unit volume integrated over both a fixed wavelength interval $\Delta\lambda$ and solid angle is

$$\varepsilon \sim \text{constant} \times n_e^2 \qquad 4.10$$

since essentially all of the light results from free-free electron transitions ($\Delta\lambda = 25\mathring{A}$). The enhancement γ in detected power is thus

$$\gamma \sim \frac{\int n_{e_2}^2\, dV - \int n_{e_1}^2\, dV}{\int n_{e_1}^2\, dV} \quad . \qquad 4.11$$

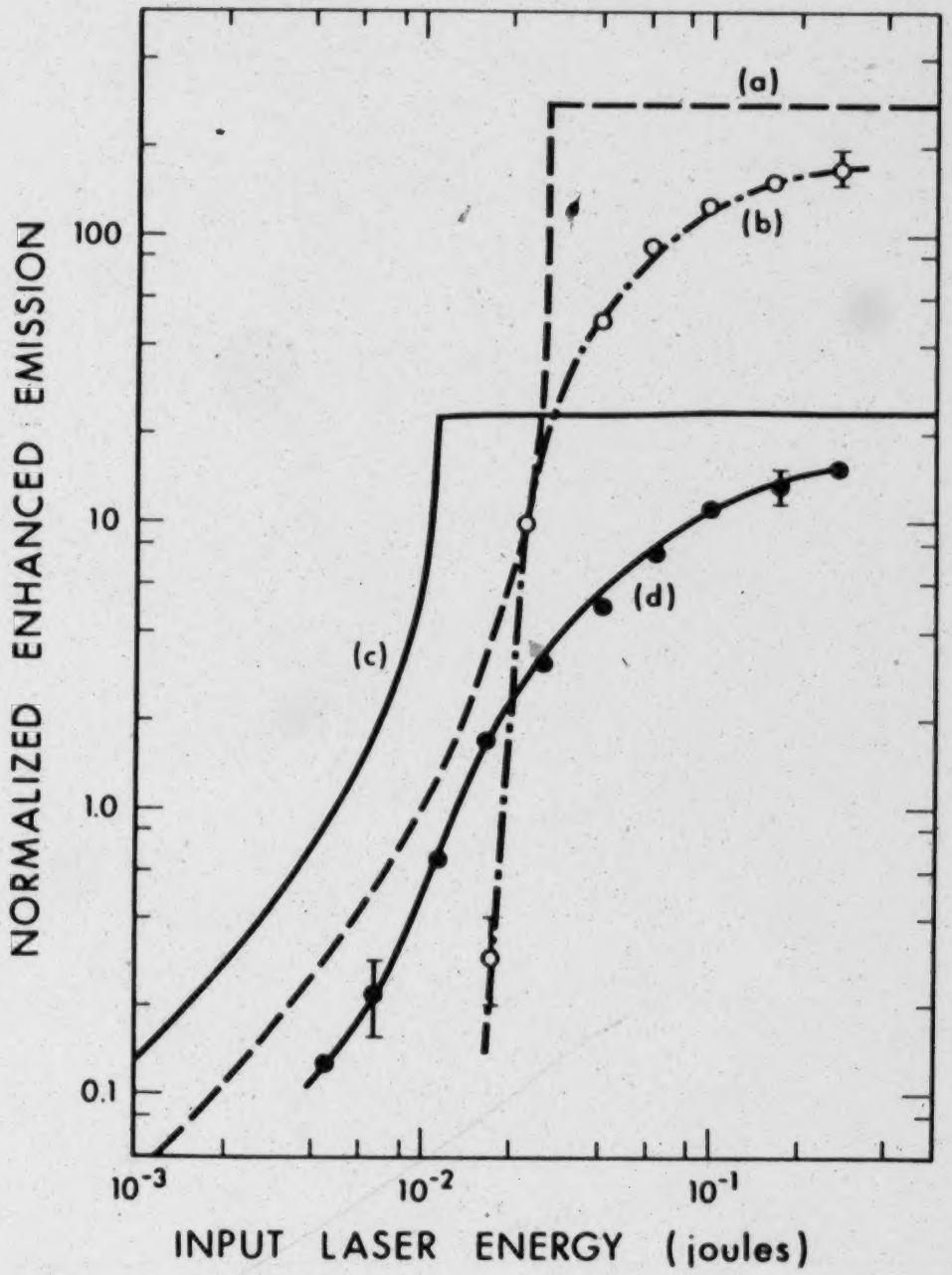

Fig. 4.5 Enhanced plasma emission vs input laser energy. Measured curves (b) for $n_e = 3 \times 10^{16}$ cm^{-3} and (d) for $n_e = 8 \times 10^{16}$ cm^{-3} correspond to theoretical curves (a) and (c) respectively.

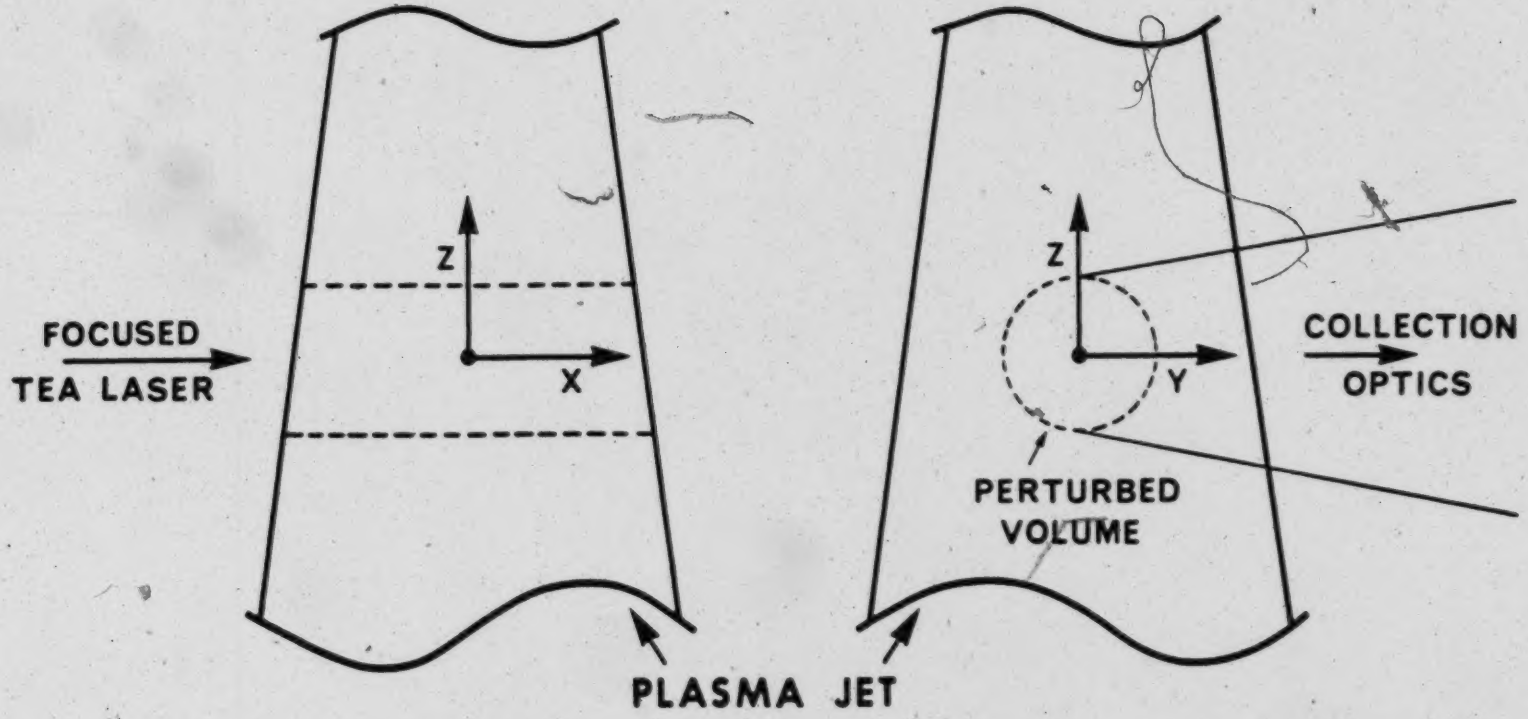

Fig. 4.6 Interaction volume of TEA laser and plasma jet.

Taking n_e to be constant in y,z and initially linear in x, eqn. 4.7 for the final density, eqn. 4.11 can be readily integrated to give

$$\gamma \approx \frac{3}{4x^3}\left(\frac{2x(1-x)}{1-2x} + \ln(1-2x)\right) - 1 \qquad 4.12$$

where $$x = \frac{1.12\times10^{-16} E_i \langle n_{e_1} \rangle}{A T_e^{3/2}\left(\frac{3}{2}T_e + I\right)}$$

and E_i = J, A = cm^2, T = eV, I = eV, $\langle n_{e_1} \rangle$ = cm^{-3} = average initial electron density in V.

Physically however, γ cannot exceed a maximum value corresponding to complete ionization of all available neutrals in V. If n_t = total number of particles in equilibrium at temperature T and atmospheric pressure prior to the laser pulse,

$$\gamma_{max} \approx \frac{3n_t}{2\langle n_{e_1} \rangle}\left(\frac{n_t}{2\langle n_{e_1} \rangle} - 1\right) . \qquad 4.13$$

Eqns. 4.12 and 4.13 are plotted in Fig. 4.5 a,c for initial densities of 3×10^{16} cm^{-3} and 8×10^{16} cm^{-3}.

Agreement with experiment is reasonable considering the numerous approximations used. It should be remembered that the Δn_e model is only a limiting case where all of the absorbed energy is taken up by further ionization of neutrals.

In practice, however, some of the absorbed energy increases the plasma temperature. Expansion of the laser-heated region resulting in decreased densities is also important in these measurements in view of the somewhat long photo-detection time constant of 30 μs. Thus the

Δn_e limit is expected to over-estimate measured enhancements, as is indeed borne out by Fig. 4.5.

Nevertheless, approximate maximum levels of TEA CO_2 laser energy usable for diagnostic purposes can be determined. As can be seen from both the shock and emission measurements, low level perturbation is assured for laser energies less than one-tenth of that required for breakdown (eqn. 4.9).

These results are, of course, still only applicable to atmospheric pressure partially ionized plasmas. For other cases such as more fully ionized plasmas, it may well be that the Δn_e limit will not apply.

CHAPTER V

SUMMARY AND CONCLUSION

Interferometry, absorption and Thomson scattering of CO_2 laser radiation have been established as useful plasma diagnostic techniques.

Inverse bremsstrahlung absorption in moderately dense plasmas has been found to give excellent results both qualitatively and quantitatively. Even though absorption depends on both electron density and temperature, either of these parameters can be determined if the other is known. Furthermore, in partially ionized plasmas where T_e is approximately constant over a wide range of n_e, absorption alone can be used to measure spatial variations in electron density.

The first experiment accurately measured the absorption coefficient using an electromagnetic shock tube with predictable electron density and temperature and a CO_2 laser. Subsequent spatial measurements of transmission through an argon plasma jet with known temperature have been Abel unfolded to give electron density profiles that are in agreement with those measured by other methods. Absorption can thus yield spatially resolved n_e in partially ionized plasmas where the variations in T_e are small ($n_e \sim T_e^8$).

On the other hand, if neither n_e or T_e is initially known, n_e can first be determined interferometrically which in turn enables calculation of T_e from the absorption. The major advantage of CO_2 laser radiation for these techniques is that the measurable fringe shifts and attenuation are appreciably larger than at shorter

wavelengths. Both interference and absorption were easily observed for spatially integrated densities $\langle n_e \ell \rangle \sim 5 \times 10^{16}$ cm^{-2}.

A 10.6μ Mach-Zehnder interferometer set up around an argon plasma jet has been used to quantitatively verify the theory of convection limited ion current to a Langmuir probe in a flowing high density plasma. Thus confidence can now also be placed in electron densities measured by Langmuir probes in highly collisional plasmas.

A new technique using simultaneous absorption and interferometry is particularly useful for transient plasmas. Such measurements on a laser-produced plasma have yielded the temporal behavior of both n_e and T_e. This setup has proved to be most useful for determining electron-ion recombination coefficients as functions of electron density and temperature.

Thomson scattering from low density plasmas was marginally successful at best. An experiment designed around a hollow cathode discharge could only provide measurement of the integrated scattering. Insufficient signal-to-noise prohibited spectral resolution of the scattered radiation. In addition, a large varying stray light level due to poor laser characteristics was unable to be subtracted from the Thomson scattering for improved signal-to-noise.

Nevertheless such measurements should be possible with an improved experimental setup. It is clear that a very stable, high power laser is required for scattering from low density plasmas. Use of a TEA CO_2 laser is therefore quite attractive. Although a cooled narrowband filter in front of the detector is essential, signal-to-noise could be further enhanced by cooling the collection optical system as well.

On the other hand, Thomson scattering of CO_2 laser light from high density plasmas was successful. A high α, collision-dominated spectrum has been observed for the first time using an argon plasma jet. The central ion feature was found to be substantially narrowed over that predicted by collisionless scattering theory. The exact linewidth could not be accurately determined since it was less than the attainable resolution; nevertheless an approximate narrowing inferred experimentally agreed with that predicted for a collisional parameter $p = (k\lambda_{mfp})^{-1}$. More detailed spectral information would require a Fabry-Perot interferometer with a much higher finesse than that used here. A higher reflectivity etalon could be used for this purpose.

Enhanced Thomson scattering of CO_2 laser radiation from non-thermal fluctuations in a laser-produced plasma has been done. A separate 10.6μ TEA laser was used for 90° scattering in a plane perpendicular to the direction of the 9.6μ TEA laser beam producing the plasma. In this setup the scattering wavevector $\underline{k}$ was not matched to any plasma modes directly pumped by non-linear self-mixing of the 9.6μ radiation. Thus the measured enhancement of $\sim$ 1000 over thermal fluctuations represents a lower bound to the level of turbulence in this plasma.

Further measurements at various $\underline{k}$ could be done by changing both the scattering plane and angle. This would establish the wavelength dependence of these fluctuations and therefore be quite helpful for a more complete understanding of non-linear coupling of high frequency radiation to plasmas.

Finally, the maximum pulsed CO_2 laser energies that can be utilized for diagnostic purposes in high density partially-ionized plasmas have been measured by focusing a variable power TEA CO_2 laser into an atmospheric pressure plasma jet. In this case the threshold for large plasma perturbations could be calculated by equating energy absorbed via inverse bremsstrahlung to an increase in ionization energy. Experimentally measured perturbations were a very non-linear function of input laser energy clearly defining a distinct threshold which cannot be appreciably exceeded. For CO_2 laser radiation, these thresholds are lower than at visible wavelengths by a factor of about 200.

REFERENCES

CHAPTER II

1. J. Dawson and C. Oberman, Phys. Fluids 5, 517 (1962).
2. I.P. Shkarofsky, T.W. Johnston and M.P. Bachynski, "The Particle Kinetics of Plasmas", (Addison-Wesley, 1966).
3. G. Bekefi, "Radiation Processes in Plasmas", (Wiley and Sons, New York, 1966).
4. P.R. Smy, Rev. Sci. Instr. 36, 1334 (1965).
5. C.K.N. Patel, P.K. Tien and J.H. McFee, Appl. Phys. Lett. 7, 290 (1965).
6. S. Mikoshiba, Ph.D. Thesis (Univ. of Alberta, 1971).
7. R.N. Morris, M.Sc. Thesis (Univ. of British Columbia, 1968).
8. H.R. Griem, "Plasma Spectroscopy", (McGraw Hill, New York, 1964).
9. B. Ahlborn, Z. Naturforsch. 20a, 466 (1965).
10. F. Keilmann, Rev. Sci. Instr. 41, 278 (1970); Ph.D. Thesis (Garching, 1971).
11. R.M. Clements and P.R. Smy, J. Appl. Phys. 41, 3745 (1970).
12. R. Fortin, M. Gravel and R. Tremblay, Can. J. Phys. 49, 1783 (1971).
13. E.V. George, G. Bekefi, R.J. Hawryluk and B. Ya'akobi, MIT Quart. Prog. Rep. 100, 105 (1971).

CHAPTER III

1. J.A. Fejer, Can. J. Phys. 38, 1114 (1960).
2. M.N. Rosenbluth and N. Rostoker, Phys. Fluids 5, 776 (1962).
3. E.E. Salpeter, Phys. Rev. 120, 1528 (1960).
4. M. Daehler and F. Ribe, Phys. Lett. 24A, 745 (1967); Phys. Rev. 161, 117 (1967).
5. J.W.M. Paul, L.S. Holmes, R.A. Hardcastle and C.C. Daughney, Inst. of Physics and Physical Society Conf. Plasma Diagnostics, Culham (1968).
6. B.L. Stansfield, R. Nodwell and J. Meyer, Phys. Rev. Lett. 26, 1219 (1971).
7. D.E. Evans and J. Katzenstein, Rep. Prog. Phys. 32, 207 (1969).
8. Y. Izawa, M. Yokoyama and C. Yamanaka, Japan. J. Appl. Phys. 8, 965 (1969).
9. C.M. Surko, R.E. Slusher, D.R. Moler and M. Porkolab, Phys. Rev. Lett. 29, 81 (1972).
10. M. Kornherr, G. Decker, M. Keilhacker, F. Lindenberger and H. Röhr, Phys. Lett. 39A, 95 (1972).
11. M. Grewal, Phys. Rev. 134, A86 (1964).
12. J.P. Dougherty and D.T. Farley Jr., J. Geophys. Res. 68, 5473 (1963).
13. T. Hagfors and R.A. Brockelman, Phys. Fluids 14, 1143 (1971).
14. J. Meyer and B.L. Stansfield, Can. J. Phys. 49, 2187 (1971).
15. N.M. Kroll, A. Ron and N. Rostoker, Phys. Rev. Lett. 13, 83 (1964).

16. E.T. Gerry, Ph.D. Thesis (MIT, 1965).

17. C.K.N. Patel, P.K. Tien and J.H. McFee, Appl. Phys. Lett. 7, 290 (1965).

18. E.M. Leonard and R.K. Osborn, Phys. Rev. A8, 2021 (1973).

19. E.J. Linnebur and J.J. Duderstadt, Plasma Physics 15, 647 (1973).

20. M.C. Richardson, A.J. Alcock, K. Leopold and P. Burtyn, Proc. IEEE Quantum Electron. Conf., Montreal (May 1972).

21. N.H. Burnett, R.D. Kerr and A.A. Offenberger, Optics Comm. 6, 372 (1972).

CHAPTER IV

1. R. Fortin, M. Gravel and R. Tremblay, Can. J. Phys. 49,1783 (1971).

2. R.N. Morris, M.Sc. Thesis (Univ. of British Columbia, 1968).

3. H.L. Brode, J. Appl. Phys. 26, 766 (1965).

4. L. Spitzer, "Physics of Fully Ionized Gases", (Interscience, New York, 1956).

APPENDIX I

The propagation of two high frequency ($\omega >> \omega_{pe}$) electromagnetic waves through an unmagnetized isotropic Maxwellian plasma is considered. Assuming collisions to be negligible, the electron ($f_e(\underline{r},\underline{v},t)$) and ion ($f_i(\underline{r},\underline{v},t)$) distribution functions satisfy Vlasov equations

$$\frac{\partial f_e}{\partial t} + \underline{v}\cdot\frac{\partial f_e}{\partial \underline{r}} - \frac{e}{m_e}\left(\underline{E} + \underline{E}_{int} + \frac{\underline{v}}{c}\times\underline{B}\right)\cdot\frac{\partial f_e}{\partial \underline{v}} = 0 \qquad \text{AI.1}$$

$$\frac{\partial f_i}{\partial t} + \underline{v}\cdot\frac{\partial f_i}{\partial \underline{r}} + \frac{Ze}{m_i}\left(\underline{E} + \underline{E}_{int} + \frac{\underline{v}}{c}\times\underline{B}\right)\cdot\frac{\partial f_i}{\partial \underline{v}} = 0 \qquad \text{AI.2}$$

where $\underline{E},\underline{B}$ are the external wave fields and $\underline{E}_{int}$ is the interparticle electric field.

Assuming sufficiently intense external waves, first order perturbations f_{el} and f_{il} of f_e and f_i from the zeroth order Maxwellians can be obtained by taking $\underline{E}_{int} = 0$. Defining the spatial and temporal Fourier transform as

$$f(\underline{k},\underline{v},\omega) = \int f(\underline{r},\underline{v},t)e^{i(\omega t-\underline{k}\cdot\underline{r})}d\underline{r}dt \qquad \text{AI.3}$$

these first order perturbations are given by

$$f_{el}(\underline{k},\underline{v},\omega) = \frac{e}{m_e}\,\frac{\underline{E}(\underline{k},\omega)\cdot\dfrac{\partial f_{em}}{\partial \underline{v}}}{i(\underline{k}\cdot\underline{v}-\omega)} \qquad \text{AI.4}$$

$$f_{i1}(\underline{k},\underline{v},\omega) = -\frac{Ze}{m_i}\frac{\underline{E}(\underline{k},\omega)\cdot\frac{\partial f_{im}}{\partial \underline{v}}}{i(\underline{k}\cdot\underline{v}-\omega)} \qquad \text{AI.5}$$

where $\underline{E}$ = sum of wave electric fields and the subscript m denotes the Maxwellian distributions as defined by eqns. 3.6. The electric field $\underline{E}$ is composed of transverse EM waves with $\omega >> \omega_{pe}$ and the plasma under consideration is non-relativistic, whereby the denominators of the above equations can be approximated by $-\omega$ since $\underline{k}\cdot\underline{v} << \omega$. Thus the first order perturbations integrated over velocity space are essentially equal to zero.

The second order perturbations are obtained for $\underline{E}_{int} \neq 0$, in which case the Fourier transformed Vlasov equations to second order are

$$i(\underline{k}\cdot\underline{v}-\omega)f_{\alpha 2}(\underline{k},\underline{v},\omega) + \frac{q_\alpha}{m_\alpha}\left(-i\underline{k}\phi(\underline{k},\omega)\right)\cdot\frac{\partial f_{\alpha m}}{\partial \underline{v}}$$

$$+\frac{1}{(2\pi)^4}\left(\frac{q_\alpha}{m_\alpha}\right)\iint\left[\underline{E}(\underline{k}',\omega') + \frac{\underline{v}}{c}\times\underline{B}(\underline{k}',\omega')\right]\cdot$$

$$\frac{\partial f_{\alpha 1}(\underline{k}-\underline{k}',\underline{v},\omega-\omega')}{\partial \underline{v}}\,d\underline{k}'d\omega' = 0 \qquad \text{AI.6}$$

where α = electrons or ions and $\underline{E}_{int} = -\nabla\phi$ defines the potential ϕ.

The interparticle electric field satisfies Poisson's equation

$$\nabla\cdot\underline{E}_{int} = 4\pi\rho = 4\pi e\, n_{eo}\left[\int f_i d\underline{v} - \int f_e d\underline{v}\right]$$

$$= 4\pi e\, n_{eo}\left[\int f_{i2} d\underline{v} - \int f_{e2} d\underline{v}\right] \qquad \text{AI.7}$$

where $\int f_{\alpha 1} d\underline{v} = 0$ and n_{eo} = average electron density. Thus

$$\phi(\underline{k},\omega) = \frac{4\pi e\, n_{eo}}{k^2}\left[\int f_{i2}(\underline{k},\omega) - \int f_{e2}(\underline{k},\omega)\right] \qquad \text{AI.8}$$

Substituting this ϕ into the Vlasov equations and integrating over velocity space gives the second order perturbation in electron density

$$f_{e2}(\underline{k},\omega) = \left(\frac{1-G_i}{1-G_e-G_i}\right)\frac{e}{m_e}\,\frac{1}{(2\pi)^4}\int \frac{\left[\underline{E}^+ + \frac{\underline{v}}{c}\times\underline{B}\right]}{i(\underline{k}\cdot\underline{v}-\omega)}\cdot\frac{\partial f_{e1}^+}{\partial \underline{v}}\,d\underline{k}'d\omega'd\underline{v}$$

$$+\left(\frac{G_e}{1-G_e-G_i}\right)\frac{Ze}{m_i}\,\frac{1}{(2\pi)^4}\int \frac{\left[\underline{E}^+ + \frac{\underline{v}}{c}\times\underline{B}\right]}{i(\underline{k}\cdot\underline{v}-\omega)}\cdot\frac{\partial f_{i1}^+}{\partial \underline{v}}\,d\underline{k}'d\omega'd\underline{v} \qquad \text{AI.9}$$

Where $\underline{E} = \underline{E}(\underline{k}',\omega')$, $\underline{B} = \underline{B}(\underline{k}',\omega')$, $f_{a1}^+ = f_{a1}(\underline{k}-\underline{k}',\underline{v},\omega-\omega')$ and the functions G_e and G_i are defined by eqns. 3.5. Since the integrals in both terms are similar, details of only the first involving f_{e1} will be given. This integral will be denoted by $R_e(\underline{k},\omega)$ and the second by $R_i(\underline{k},\omega)$.

Noting that the plasma is isotropic and using the previous non-relativistic approximation

$$f_{e1}^+(\underline{k},\underline{v},\omega) = \frac{e}{im_e}\cdot\frac{2b\underline{v}\cdot\underline{E}^+ f_{em}(\underline{v})}{\omega-\omega'} \qquad \text{AI.10}$$

where $b = \frac{1}{v_e^2} = \frac{m_e}{2K_B T_e}$.

Taking components of $\underline{v}$ parallel and perpendicular to $\underline{E}^+$, it can be shown that

$$\frac{\partial f_{e1}^{+}}{\partial \underline{v}} = \frac{2be}{im_e} \cdot \frac{f_{em}(\underline{v})\left[\underline{E}^{+}-2b(\underline{E}^{+}\cdot\underline{v})\underline{v}\right]}{\omega-\omega'} \qquad \text{AI.11}$$

whereby

$$R_e(\underline{k},\omega) = \frac{2be}{m_e}\int \frac{f_{em}(\underline{v})\underline{E}\cdot\left\{\underline{E}^{+}-2b(\underline{E}^{+}\cdot\underline{v})\underline{v}\right\}}{(\omega'-\omega)(\underline{k}\cdot\underline{v}-\omega)}\, d\underline{k}'d\omega'd\underline{v}$$

$$+ \frac{2be}{m_e c}\int \frac{f_{em}(\underline{v})\left\{\underline{v}\times\underline{B}\right\}\cdot\left\{\underline{E}^{+}-2b(\underline{E}^{+}\cdot\underline{v})\underline{v}\right\}}{(\omega'-\omega)(\underline{k}\cdot\underline{v}-\omega)}\, d\underline{k}'d\omega'd\underline{v}$$

$$= \frac{2be}{m_e} I_1 + \frac{2be}{m_e c} I_2 \qquad \text{AI.12}$$

Attention is now given to evaluating I_1, performing the velocity integration first. Taking vector components parallel and perpendicular to $\underline{k}$ and redefining the distribution function in terms of these components:

$$f_{em}(\underline{v}) = F_e(v_{11})F_e(v_{\perp 1})F_e(v_{\perp 2}) \qquad \text{AI.13}$$

where $$F_e(v) = \sqrt{\frac{b}{\pi}}\, e^{-bv^2} \qquad \text{AI.14}$$

it can be easily shown that

$$I_1 = \int \frac{d\underline{k}'d\omega'}{\omega-\omega'}\int \frac{dv_{11}\,\frac{\partial F_e(v_{11})}{\partial v_{11}}}{kv_{11}-\omega}\,(1-2bv_{11}^2)E_{11}E_{11}^{+}$$

$$= -\frac{1}{2b}\int \frac{d\underline{k}'d\omega'}{\omega-\omega'}\, E_{11}E_{11}^{+}\int \frac{\frac{\partial^2 F_e(v_{11})}{\partial v_{11}^2}}{kv_{11}-\omega}\, dv_{11} \qquad \text{AI.15}$$

Integrating by parts

$$I_1 = -\frac{1}{2b}\int \frac{d\underline{k}'d\omega'}{\omega-\omega'}\,(kE_{11}E_{11}^{+})\int \frac{\frac{\partial F_e(v_{11})}{\partial v_{11}}}{(kv_{11}-\omega)^2}\,dv_{11} \,. \qquad \text{AI.16}$$

Noting that the defined function $G_e(\underline{k},\omega)$ is

$$G_e(\underline{k},\omega) = \frac{\omega_{pe}^2}{k^2}\int \frac{\underline{k}\cdot\frac{\partial f_e(\underline{v})}{\partial \underline{v}}}{\underline{k}\cdot\underline{v}-\omega}\,d\underline{v}$$

$$= \frac{\omega_{pe}^2}{k}\int \frac{\frac{\partial F_e(v_{11})}{\partial v_{11}}}{kv_{11}-\omega}\,dv_{11} \,, \qquad \text{AI.17}$$

$$I_1 = -\frac{k^2}{2b\omega_{pe}^2}\,\frac{\partial G_e}{\partial \omega}\int \frac{E_{11}E_{11}^{+}d\underline{k}'d\omega'}{\omega'-\omega}$$

$$= -\frac{1}{2b\omega_{pe}^2}\,\frac{\partial G_e}{\partial \omega}\int \frac{(\underline{k}.\underline{E})(\underline{k}.\underline{E}^{+})}{\omega'-\omega}\,d\underline{k}'d\omega' \,. \qquad \text{AI.18}$$

For two plane monochromatic waves

$$\underline{E}_{1,2}(\underline{r},t) = \underline{E}^{\circ}_{1,2}\cos(\underline{k}_{1,2}\cdot\underline{r} - \omega_{1,2}t) \qquad \text{AI.19}$$

$$\underline{B}_{1,2}(\underline{r},t) = \underline{B}^{\circ}_{1,2}\cos(\underline{k}_{1,2}\cdot\underline{r} - \omega_{1,2}t) \,, \qquad \text{AI.20}$$

$$\underline{E}(\underline{k},\omega) = \frac{(2\pi)^4}{2}\left\{\underline{E}^{\circ}_1\left[\delta(\underline{k}-\underline{k}_1)\delta(\omega-\omega_1) + \delta(\underline{k}+\underline{k}_1)\delta(\omega+\omega_1)\right]\right.$$

$$\left. + \underline{E}^{\circ}_2\left[\delta(\underline{k}-\underline{k}_2)\delta(\omega-\omega_2) + \delta(\underline{k}+\underline{k}_2)\delta(\omega+\omega_2)\right]\right\} \,. \qquad \text{AI.21}$$

Defining a convention for conciseness

$$\underline{E}(x) = \frac{(2\pi)^4}{2}\left\{\underline{E}_1^\circ\left[\delta(x-x_1)+\delta(x+x_1)\right] + \underline{E}_2^\circ\left[\delta(x-x_2)+\delta(x+x_2)\right]\right\} \qquad \text{AI.22}$$

and

$$\underline{B}(x) = \frac{(2\pi)^4}{2}\left\{\underline{B}_1^\circ\left[\delta(x-x_1)+\delta(x+x_1)\right] + \underline{B}_2^\circ\left[\delta(x-x_2)+\delta(x+x_2)\right]\right\}. \qquad \text{AI.23}$$

Substituting $\underline{E}(x')$ and $\underline{E}^+(x-x')$ into equation AI.18, integrating over $x' = \underline{k}',\omega'$ and retaining only low frequency terms ($\omega << \omega_{1,2}$):

$$I_1 = -\frac{1}{2b\omega_{pe}^2}\frac{\partial G_e}{\partial \omega}\frac{(2\pi)^8}{4}(\underline{k}\cdot\underline{E}_1^\circ)(\underline{k}\cdot\underline{E}_2^\circ)$$

$$\left[\delta(x-x_2+x_1)\left\{\frac{1}{\omega_2-\omega}+\frac{1}{-\omega_1-\omega}\right\} + \delta(x+x_2-x_1)\left\{\frac{1}{\omega_1-\omega}+\frac{1}{-\omega_2-\omega}\right\}\right]$$

$$= +\frac{(2\pi)^8}{8b\omega_{pe}^2}\frac{\partial G_e}{\partial \omega}(\underline{k}\cdot\underline{E}_1^\circ)(\underline{k}\cdot\underline{E}_2^\circ)\frac{\omega}{\omega_1\omega_2}\left[\delta(x-x_2+x_1)+\delta(x+x_2-x_1)\right]$$

$$= +\frac{(2\pi)^8}{8b\omega_{pe}^2}\frac{\partial G_e}{\partial \omega}(\underline{k}_1\cdot\underline{E}_2^\circ)(\underline{k}_2\cdot\underline{E}_1^\circ)\frac{\omega}{\omega_1\omega_2}\left[\delta(x-x_2+x_1)+\delta(x+x_2-x_1)\right]. \qquad \text{AI.24}$$

Attention is now turned to evaluation of I_2. Noting that

$$(\underline{v}\times\underline{B})\cdot\left[\underline{E}^+ - 2b(\underline{E}^+\cdot\underline{v})\underline{v}\right] = -\underline{v}\cdot(\underline{E}^+\times\underline{B}) \quad ,$$

$$I_2 = -\int \frac{d\underline{k}'d\omega'}{\omega'-\omega} (\underline{E}^+ x \underline{B}) \cdot \int \frac{\underline{v} f_{em}(\underline{v})}{\underline{k}\cdot\underline{v}-\omega} d\underline{v} \ . \qquad \text{AI.25}$$

Again taking velocity components parallel and perpendicular to $\underline{k}$ and performing the integral over velocity,

$$I_2 = -\int \frac{d\underline{k}'d\omega'}{\omega'-\omega} (\underline{E}^+ x \underline{B}) \cdot \underline{k} \left(\frac{1}{-2b\omega_{pe}^2} \right) G_e(\underline{k},\omega)$$

$$= \frac{G_e(\underline{k},\omega)}{2b\omega_{pe}^2} \int \frac{\underline{k}\cdot(\underline{E}^+ x \underline{B})}{\omega'-\omega} dx' \qquad \text{AI.26}$$

for the previously defined $x' = \underline{k}', \omega'$. Substituting eqns. AI.22 and AI.23 for $\underline{E}^+(x-x')$ and $\underline{B}(x')$, integrating over $\underline{k}', \omega'$ and retaining only terms for $\omega << \omega_{1,2}$,

$$I_2 = \frac{(2\pi)^8 G_e \underline{k}}{8b\omega_{pe}^2} \cdot \left\{ \delta(x+x_2-x_1) \left[\frac{\underline{E}_2^\circ x \underline{B}_1^\circ}{\omega_2} - \frac{\underline{E}_1^\circ x \underline{B}_2^\circ}{\omega_1} \right] \right.$$

$$\left. + \delta(x-x_2+x_1) \left[\frac{\underline{E}_1^\circ x \underline{B}_2^\circ}{\omega_1} - \frac{\underline{E}_2^\circ x \underline{B}_1^\circ}{\omega_2} \right] \right\} \cdot \qquad \text{AI.27}$$

But $\underline{B}_{1,2}^\circ = c(\underline{k}_{1,2} x \underline{E}_{1,2}^\circ)/\omega_{1,2}$, therefore

$$I_2 = \frac{(2\pi)^8 c G_e}{8b\omega_{pe}^2 \omega_1 \omega_2} \left\{ \delta(x+x_2-x_1) \left[\underline{k}\cdot(\underline{k}_1-\underline{k}_2)(\underline{E}_1^\circ \cdot \underline{E}_2^\circ) \right.\right.$$

$$+ (\underline{k}\cdot\underline{E}_2^\circ)(\underline{k}_2\cdot\underline{E}_1^\circ) - (\underline{k}_1\cdot\underline{E}_2^\circ)(\underline{k}\cdot\underline{E}_1^\circ) \Big]$$

$$+ \delta(x-x_2+x_1) \Big[\underline{k}\cdot(\underline{k}_2-\underline{k}_1)(\underline{E}_1^\circ \cdot \underline{E}_2^\circ) + (\underline{k}\cdot\underline{E}_1^\circ)(\underline{k}_1\cdot\underline{E}_2^\circ)$$

$$\left.\left. - (\underline{k}\cdot\underline{E}_2^\circ)(\underline{k}_2\cdot\underline{E}_1^\circ) \Big] \right\} \cdot \qquad \text{AI.28}$$

Noting that in terms $\delta(x+x_2-x_1)$ that $\underline{k} = \underline{k}_1-\underline{k}_2$ and in terms $\delta(x-x_2+x_1)$ that $\underline{k} = \underline{k}_2-\underline{k}_1$,

$$I_2 = \frac{(2\pi)^8 c G_e}{8b\omega_{pe}^2\omega_1\omega_2}\left\{|\underline{k}|^2(\underline{E}_1^\circ\cdot\underline{E}_2^\circ) + 2(\underline{k}_1\cdot\underline{E}_2^\circ)(\underline{k}_2\cdot\underline{E}_1^\circ)\right\}\cdot$$

$$\left\{\delta(x-x_2+x_1) + \delta(x+x_2-x_1)\right\} \cdot \qquad \text{AI.29}$$

Substitution of eqns. AI.24 and AI.29 for I_1 and I_2 into eqn. AI.12 yields

$$R_e(\underline{k},\omega) = \frac{(2\pi)^8 e}{4m_e\omega_{pe}^2\omega_1\omega_2}\left\{G_e\left[|\underline{k}|^2(\underline{E}_1^\circ\cdot\underline{E}_2^\circ) + 2(\underline{k}_1\cdot\underline{E}_2^\circ)(\underline{k}_2\cdot\underline{E}_1^\circ)\right]\right.$$

$$\left. + \omega\frac{\partial G_e}{\partial\omega}(\underline{k}_1\cdot\underline{E}_2^\circ)(\underline{k}_2\cdot\underline{E}_1^\circ)\right\}\left\{\delta(x-x_2+x_1)+\delta(x+x_2-x_1)\right\}$$

AI.30

or substituting $\omega_{pe}^2 = 4\pi e^2 n_{eo}/m_e$ and rearranging

$$R_e(\underline{k},\omega) = \frac{(2\pi)^8}{16\pi e n_{eo}\omega_1\omega_2}\left\{G_e|\underline{k}|^2(\underline{E}_1^\circ\cdot\underline{E}_2^\circ)\right.$$

$$\left. + \frac{1}{\omega}\frac{\partial(\omega^2 G_e)}{\partial\omega}(\underline{k}_1\cdot\underline{E}_2^\circ)(\underline{k}_2\cdot\underline{E}_1^\circ)\right\}\cdot$$

$$\left\{\delta(x-x_2+x_1) + \delta(x+x_2-x_1)\right\} \cdot \qquad \text{AI.31}$$

$R_i(\underline{k},\omega)$ can be obtained from this result by putting

$$e \rightarrow -Ze$$

$$n_{eo} \rightarrow n_{io} = n_{eo}/Z$$

$$G_e \rightarrow G_i \ .$$

Substituting these expressions for R_e and R_i into eqn. AI.9, the second order electron density perturbation becomes,

$$f_{e2}(\underline{k},\omega) = \frac{\pi^3}{m_e n_{eo} \omega_1 \omega_2} \left\{ \delta(\underline{k}-\Delta\underline{k})\delta(\omega-\Delta\omega)+\delta(\underline{k}+\Delta\underline{k})\delta(\omega+\Delta\omega) \right\}$$

$$\left(\frac{1-G_i}{1-G_e-G_i} \right) \left\{ |\underline{k}|^2 (\underline{E}_1 \cdot \underline{E}_2) G_e + \frac{1}{\omega} \frac{\partial(\omega^2 G_e)}{\partial\omega} (\underline{k}_1 \cdot \underline{E}_2)(\underline{k}_2 \cdot \underline{E}_1) \right\}$$

$$- \left(Z\frac{m_e}{m_i} \right) \left(\frac{G_e}{1-G_e-G_i} \right) \left\{ |\underline{k}|^2 (\underline{E}_1 \cdot \underline{E}_2) G_i + \frac{1}{\omega} \frac{\partial(\omega^2 G_i)}{\partial\omega} \right.$$

$$\left. \cdot (\underline{k}_1 \cdot \underline{E}_2)(\underline{k}_2 \cdot \underline{E}_1) \right\} \qquad \text{AI.32}$$

where $\underline{E}_{1,2}$ is now taken to represent the field amplitudes and $\Delta\underline{k} \equiv \underline{k}_2 - \underline{k}_1$, $\Delta\omega \equiv \omega_2 - \omega_1$.

Regrouping terms and noting that $Zm_e << m_i$,

$$f_{e2}(\underline{k},\omega) = \frac{\pi^3}{m_e n_{eo} \omega_1 \omega_2} \left\{ \delta(\underline{k}-\Delta\underline{k})\delta(\omega-\Delta\omega) + \delta(\underline{k}+\Delta\underline{k})\delta(\omega+\Delta\omega) \right\}$$

$$\left[\begin{array}{l} \left(\frac{1-G_i}{1-G_e-G_i} \right) \left\{ |\underline{k}|^2 (\underline{E}_1 \cdot \underline{E}_2) + 2(\underline{k}_1 \cdot \underline{E}_2)(\underline{k}_2 \cdot \underline{E}_1) \right\} G_e \\ + \left(\frac{1-G_i}{1-G_e-G_i} \right) (\underline{k}_1 \cdot \underline{E}_2)(\underline{k}_2 \cdot \underline{E}_1)\omega \frac{\partial G_e}{\partial\omega} \\ - \left(Z\frac{m_e}{m_i} \right) \left(\frac{G_e}{1-G_e-G_i} \right) (\underline{k}_1 \cdot \underline{E}_2)(\underline{k}_2 \cdot \underline{E}_1)\omega \frac{\partial G_i}{\partial\omega} \end{array} \right] \qquad \text{AI.33}$$

or using the function W and dimensionless parameter x (see eqns. 3.9 - 3.12),

$$f_{e2}(\underline{k},\omega) = -\frac{\pi^3 \alpha_1^2}{m_e n_{eo}\,\omega_1\omega_2}\left(\frac{1}{1+\alpha_1^2 W(x_e)+\alpha_1^2\left(Z\frac{T_e}{T_i}\right)W(x_i)}\right)\left\{\delta_{\underline{k},\omega}\right\}$$

$$\left[\begin{array}{l}\left\{|\underline{k}|^2(\underline{E}_1\cdot\underline{E}_2)+2(\underline{k}_1\cdot\underline{E}_2)(\underline{k}_2\cdot\underline{E}_1)\right\}\left[1+\alpha_1^2\left(Z\frac{T_e}{T_i}\right)W(x_i)\right] \\ \cdot W(x_e)+(\underline{k}_1\cdot\underline{E}_2)(\underline{k}_2\cdot\underline{E}_1)\left\{\left[1+\alpha_1^2\left(Z\frac{T_e}{T_i}\right)W(x_i)\right]\right. \\ \left.\cdot x_e\ \frac{\partial W(x_e)}{\partial x_e}-\alpha_1^2\left(Z\frac{m_e}{m_i}\right)W(x_e)x_i\ \frac{\partial W(x_i)}{\partial x_i}\right\}\end{array}\right]$$

AI.34

where $\alpha_1 \equiv (k\lambda_{De})^{-1}$ and $\delta_{\underline{k},\omega} = \delta(\underline{k}-\Delta\underline{k})\delta(\omega-\Delta\omega)+\delta(\underline{k}+\Delta\underline{k})\delta(\omega+\Delta\omega)$.

Consider the magnitude of the factor

$$\left[1+\alpha_1^2\left(Z\frac{T_e}{T_i}\right)W(x_i)\right]x_e\ \frac{\partial W(x_e)}{\partial x_e}-\alpha_1^2\left(Z\frac{m_e}{m_i}\right)W(x_e)x_i\ \frac{\partial W(x_i)}{\partial x_i}$$

for $T_e \gtrsim T_i$. In this case $x_e \ll x_i$, whereby for $x_i \lesssim 1$, the functions $W(x_e) \sim 1$, $\left|\frac{\partial W(x_e)}{\partial x_e}\right| \sim 1$, $|W(x_i)| \sim 1$ and $\left|\frac{\partial W(x_i)}{\partial x_i}\right| \sim 1$. Thus the first term has a magnitude of order

$$\left[1+\alpha_1^2\left(Z\frac{T_e}{T_i}\right)\right]x_e$$

while the second term has magnitude of order

$$\alpha_1^2\left(Z\frac{m_e}{m_i}\right)x_i\ .$$

Noting specifically that $x_i = \sqrt{\frac{m_i T_e}{m_e T_i}} x_e$, it is clear that the contribution from the second term is negligible. For large x_i, $\frac{\partial W(x_i)}{\partial x_i} \sim \frac{1}{x_i^3}$ whereby the second term is again negligible.

Thus to good approximation for $T_e \geq T_i$

$$f_{e2}(\underline{k},\omega) = -\frac{\pi^3 \alpha_1^2}{n_{eo} m_e \omega_1 \omega_2} \left\{ \delta(\underline{k}-\Delta\underline{k})\delta(\omega-\Delta\omega) + \delta(\underline{k}+\Delta\underline{k})\delta(\omega+\Delta\omega) \right\}$$

$$\cdot \left[\frac{1 + \alpha_1^2 Z\left(\frac{T_e}{T_i}\right) W(x_i)}{1 + \alpha_1^2 W(x_e) + \alpha_1^2 Z\left(\frac{T_e}{T_i}\right) W(x_i)} \right]$$

$$\cdot \left\{ W(x_e) \left\{ |\underline{k}|^2 (\underline{E}_1 \cdot \underline{E}_2) + 2(\underline{k}_1 \cdot \underline{E}_2)(\underline{k}_2 \cdot \underline{E}_1) \right\} \right.$$

$$\left. + x_e \frac{\partial W(x_e)}{\partial x_e} (\underline{k}_1 \cdot \underline{E}_2)(\underline{k}_2 \cdot \underline{E}_1) \right] . \qquad \text{AI.35}$$

This approximation essentially disregards direct excitation of ion fluctuations by the incident waves leaving only excitation through electrostatic coupling with electrons.

APPENDIX II

Fabry-Perot interferometers have been extensively used for high resolution of spectra at wavelengths in the visible. On the other hand, only recently have improved optical coatings and detectors for the infrared enabled such measurements at long wavelengths. This appendix discusses the characteristics of a Fabry-Perot interferometer designed for and used at $\lambda = 10.6\mu$.

The classical theory of Fabry-Perotscan be found in almost any book on physical optics. In summary, the relations of experimental interest are:

Resonance condition:

$$m\lambda = 2d\cos\theta$$

Free Spectral Range:

$$\lambda_s = \frac{\lambda_o^2}{2d}$$

Instrumental Width:

$$\lambda_w = \frac{1-R}{\sqrt{R}} \frac{\lambda_o^2}{2\pi d}$$

Finesse:

$$F = \frac{\lambda_s}{\lambda_w} = \pi \frac{\sqrt{R}}{1-R}$$

Resolving Power:

$$R.P. = \pi m \frac{\sqrt{R}}{1-R}$$

Acceptance Angle:

$$\theta_{acc} = \frac{2}{\sqrt{R.P.}}$$

Angular Orders:

$$\theta_{ord} = 2 \sin^{-1}\left(\frac{n\lambda_o}{4d}\right)^{1/2}$$

Visibility:

$$V = \left(\frac{1+R}{1-R}\right)^2$$

where λ_o = mean wavelength,

m = axial (longitudinal) mode number,

d = plate spacing,

θ = angle of incident beam relative to the cavity axis,

R = geometrical mean reflectivity of mirrors,

n = angular mode number.

These relations apply for $m \gg 1$ (i.e. $d \gg \lambda$) which is generally used experimentally.

The scanning mode of operation was used for the Thomson scattering measurements of Chapter III. In this case, only the axial

cavity mode is excited ($\theta = 0$, $n = 0$) by a well-collimated incident beam. Wavelength scanning is done by changing the cavity length by small known amounts ($\Delta\lambda = \left(\frac{2}{m}\right)\Delta d$). Note that wavelength shifts are directly proportional to variations in plate spacing. For $\Delta\lambda = \lambda_s$, $\Delta d = \lambda_o/2$ which also equals the inter-order separation ($\Delta m = 1$). Thus wavelength calibration is automatic provided the plate spacing can be varied by at least one wavelength.

The first step in designing a Fabry-Perot is to choose a free-spectral range (dynamic range) slightly greater than the total width of the incident radiation to eliminate overlapping of orders. Since λ_s is always only a function of d and λ_o, the plate spacing required is therefore determined. This result can then be used to calculate the mirror reflectivity necessary to obtain the desired resolution.

Etalons used for measurements reported in this thesis were originally purchased for Thomson scattering measurements from the low density hollow cathode discharge. It was hoped to be able to resolve both low α Doppler broadened ($\Delta\lambda \sim 900\text{Å}$) and the cooperative $\alpha = 2$ ($\Delta\lambda \sim 200\text{Å}$) spectra. Extremely high resolution was undesirable since the transmitted power levels would not be detectable. Therefore a $\lambda_s = 1000\text{Å}$ and a $\lambda_w = 20\text{Å}$ were chosen, which required a reflectivity of 94% to achieve the finesse of 50. Such a reflectivity was obtained by a multi-layer dielectric coating on a germanium substrate. Reflectivities of up to 99% can presently be easily achieved using this technique.

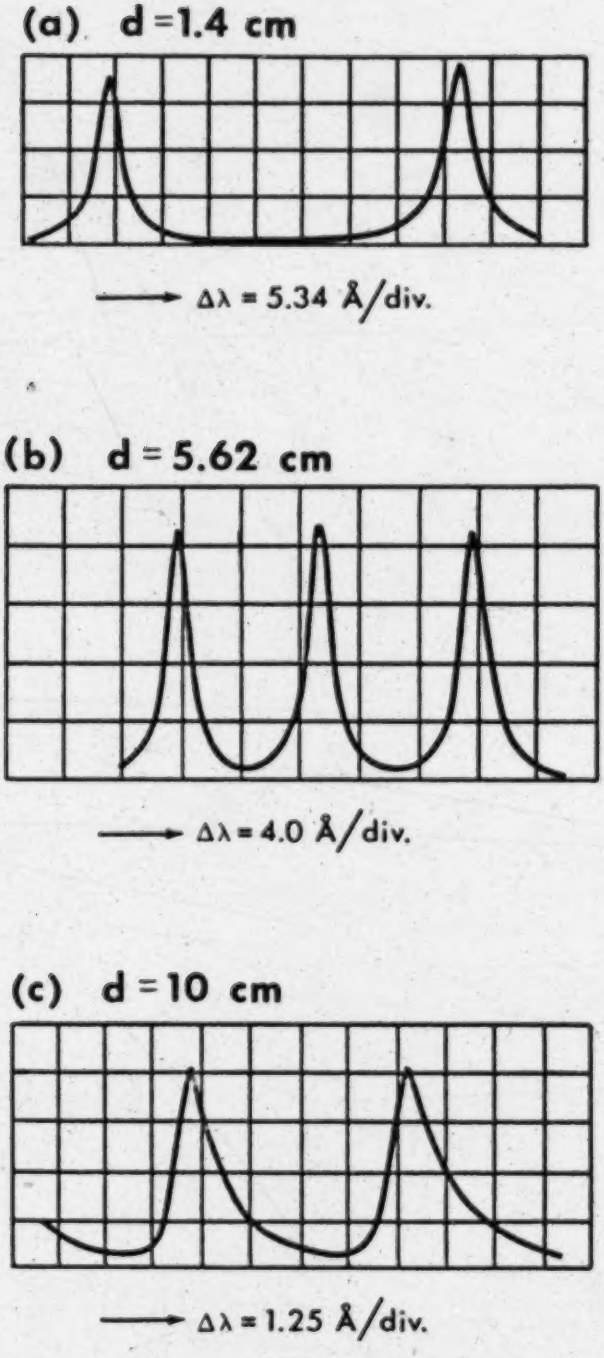

Fig. A2.1 Fabry-Perot resolution characteristics as a function of plate spacing.

With these etalons (R = 94%), a measured finesse of 45 and peak transmission of 90% were found for a plate spacing of 560μ (λ_s = 1000Å). For larger spacings both of these parameters were substantially less. Fig. A2.1 shows the resolution achieved with (a) d = 1.4 cm, λ_s = 40Å, (b) d = 5.62 cm, λ_s = 10Å and (c) d = 10 cm, λ_s = 5.6Å. Note that the amplitude scale is in arbitrary units and different in each case. The setup described in Chapter III was used to obtain these scans.

For d = 10 cm, the maximum finesse was 6 and peak transmission ~ 4% whereas F = 50 would be expected on the basis of mirror reflectivity. In practice, however, the actual finesse includes mirror tilt, mirror surface figure, diffraction and an inadequately collimated incident beam. These additional factors decrease F for increased plate spacings and become dominant for large d, whereby the finesse of 6 achieved with the optical system of Chapter III is not unreasonable.